Vibration-induced settlement of a slip-joint connection for offshore wind turbines

Segeren, Maxim

DOI
10.4233/uuid:caf8ff62-7b9b-4dc1-b3b9-2087819d2ae1

Publication date
2018

Document Version
Final published version

Citation (APA)
Segeren, M. (2018). *Vibration-induced settlement of a slip-joint connection for offshore wind turbines*. [Dissertation (TU Delft), Delft University of Technology]. https://doi.org/10.4233/uuid:caf8ff62-7b9b-4dc1-b3b9-2087819d2ae1

VIBRATION-INDUCED SETTLEMENT OF A SLIP-JOINT CONNECTION FOR OFFSHORE WIND TURBINES

Proefschrift

ter verkrijging van de graad van doctor
aan de Technische Universiteit Delft,
op gezag van de Rector Magnificus prof. dr. ir. T. H. J. J. van der Hagen,
voorzitter van het College voor Promoties,
in het openbaar te verdedigen op 23 februari 2018 om 10:00 uur

door

Maxim Luka Adriaan SEGEREN

Master of Science in Offshore Engineering
geboren te Dordrecht, Nederland.

Dit proefschrift is goedgekeurd door de

promotor: Prof. dr. A.V. Metrikine en
copromotor: dr. ir. H. Hendrikse

Samenstelling promotiecommissie:

Rector Magnificus	voorzitter
Prof. dr. A.V. Metrikine,	Technische Universiteit Delft, promotor
dr. ir. H. Hendrikse,	Technische Universiteit Delft, copromotor

Onafhankelijke leden:

Prof. dr. ir. J. Rots,	Technische Universiteit Delft
Prof. dr. ir. W. Lacarbonara,	Sapienza University of Rome
Prof. dr. J. Tuhkuri,	Aalto University, Finland
Prof. dr. ir. A. Suiker,	Technische Universiteit Eindhoven
dr. ing. M. Seidel,	Siemens Gamesa Renewable Energy
Prof. dr. ir. M.L. Kaminski,	Technische Universiteit Delft, reservelid

This thesis was financed by the research programme Far and Large Offshore Wind (FLOW). This was a joint research programme of thirteen Dutch companies and knowledge institutions who worked together on innovation to reduce the cost of offshore wind energy.

Printed by: Gildeprint

Cover picture: Courtesy of DOT b.v., edited by Julien Segeren

ISBN 978-94-6186-891-6

An electronic version of this dissertation is available at
`http://repository.tudelft.nl/`.

SUMMARY

The majority of existing offshore wind turbines typically consist of a monopile foundation, a transition piece with a vertically positioned grouted connection, a turbine tower, and a turbine. Of the 2,653 offshore turbines that were installed by the end of 2015, 80 percent are supported by a monopile.

Despite the current overwhelming dominance of the monopile, its future application is rather uncertain. Offshore wind turbines have continuously increased in size and have moved to deeper waters; these developments require larger and heavier support structures. It is unlikely that floating structures will be preferred to bottom-founded structures, up to a water depth of 80 m. The question thus becomes whether jackets or monopiles will be used under such conditions? The monopile seems to be losing in this competition, as, to meet the requirements a monopile would have to be extremely large; thus, it may no longer fall within industry limits, both in terms of manufacturing demands and the lifting capacity of dedicated installation vessels. One may wonder whether a single monopile would be necessary, or if a set of intelligently connected smaller length monopiles could suffice. The key to the success of such a concept could be the so-called slip-joint connection.

A slip-joint consists of two conical sections made of steel. This connection does not require any grout and, besides being a connection option for the transition piece and monopile, allows monopiles to be comprised of a number of lighter sections of very large diameters. By employing a slip-joint, the applicability of the monopile could be extended to deeper waters and to turbines that have very large rotors and power capacities.
Although the slip-joint connection has been successfully used for onshore wind turbines in the past, it has not yet been used offshore. One of the challenges in using the slip-joint is ensuring a proper fit of the cones despite the imperfections that result from manufacturing tolerances, deformations by pile driving, and the potential damage that may occur during the handling of the cones.

In this thesis, it is proposed that a slight difference in the cone angles be used to address the aforementioned imperfections. A steeper cone angle for the transition piece when compared to that of the monopile is proposed. These slightly different cone angles require the upper cone to deform elastically in order to slide down the lower cone during installation. To facilitate the installation process, it is proposed that vibrations be employed in order to cause the upper cone to slide down under its own weight. In order to use this new method of connecting joints, it will be necessary to investigate the manner in which vibrations influence the relative motions of the two cones that need to achieve stable contact.

The objective of this thesis is to investigate the potential of the use of vibrations in the installation and dismounting of a slip-joint with slightly different cone angles. The research is conducted by means of numerical modelling and experiments.

In order to carry out a preliminary investigation into the dynamics of the slip-joint, a lumped mass model of the vibration-induced settlement of a slip-joint is developed and analysed. The predictions of the model indicate that the slip distance caused by the weight of the upper cone of a slip-joint alone is insufficient to obtain the desired contact overlap, even for small cone angles. It is demonstrated that the desired contact overlap can be achieved by means of the application of a vibratory load. Furthermore, the model indicates that specific combinations of the amplitudes and forcing frequencies of the load are effective in achieving the desired overlap between the cones. These results support the idea that the controlled installation of a slip-joint is possible with the use of a vibratory load.

In order to demonstrate the effectiveness of vibration-induced settlement in the installation and dismount of a slip-joint for offshore wind turbines, an experimental setup is designed and constructed. The setup is designed in such a manner that the envisaged full-scale installation sequence can be mimicked using scaled specimens. Vibrations are introduced during the experiments using either a set of eccentric motors or an electrodynamic shaker. Using this setup, the following topics are investigated:

1. The effect of vibration-induced movement on scaled slip-joint specimens is investigated using two types of vibratory devices.
2. An experimental modal analysis is conducted in order to identify which frequencies are effective in inducing settlement and to identify the corresponding effective operational deflection shapes of the scaled slip-joint.
3. The dimensions and geometry of a set of scaled cones are measured to determine the status of the cones that are used in the experiments.

The tests demonstrate that the frequency of the vibration applied, is key to the successful installation or dismounting of a slip-joint. Only applied vibration of specific resonance frequencies are found to be effective and allow relative movement to occur. It is observed that an application of a larger force amplitude in combination with a frequency that differs from those specific resonance frequencies that were found to be effective does not automatically result in additional settlement. The settlement that occurs during the application of vibration stabilizes to certain equilibrium levels. This observed behaviour will likely make this procedure attractive for future implementation in offshore conditions when control of the settlement level is desired.
With the use of an electrodynamic shaker, settlement levels similar to those achieved through the use of an eccentric motor are obtained, while the applied force amplitudes are 250 times smaller than those imposed by the eccentric motor. This demonstrates the dominant influence of frequency on the settlement behaviour of the joint.

In order to investigate the behaviour of the cones at the frequencies that were found to be effective in terms of settlement, an experimental modal analysis is conducted on the

installed scaled slip-joint. The results of this experiment confirm that, predominately, those vibrations that are effective at inducing settlement are at the natural frequencies of the combined system. The modal shape around 120 Hz, which is the most effective for installation and dismounting purposes, is characterized by the circumferential mode m=2 and longitudinal mode n=1 of a conical shell.

Based on the measured dimensions of the specimens, an impression of the manufacturing tolerances, the initial contact and the development of the contact are obtained. The results indicate that the specimens have larger local deformations and ovality than aimed for. Analysis of the contact indicates that it develops at two distinct areas and then expands in circumferential direction with increasing settlement levels.

A finite element model is set up, with the aim of reproducing the observations of the experiments qualitatively. The model reproduces settlement behaviour that can be identified as stick-slip. Moreover, the model is capable of capturing the key behaviour of the slip-joint under the influence of vibration. Only vibrations at frequencies corresponding to certain natural frequencies effectively induce relative movements between the cones for small amplitudes of the dynamic force. The finite element model predictions capture this frequency dependence of the vibration induced settlement for both installation and dismounting simulations. The specific mode that corresponds to the circumferential mode m=2 and the longitudinal mode n=1, identified as most effective in the experiments, was also found to be so in the model. A closer look at the settlement process and its dependence on the time signature and symmetry of the load reconfirmed that the settlement is a stick-slip process that occurs at the resonance frequencies of the combined system.
A parametric study is conducted in order to investigate the uncertainties associated with the finite element model. This study indicates that the experimental settlement level achieved as a result of the simulated self-weight can be approximated by utilizing a low friction coefficient in the simulations. The settlement level that occurred as a result of the application of the vibrations that were found to be effective during the experiments was not matched by the finite element model. This difference can be related to the discrepancy between the perfect contact along the circumference of the finite element model and the imperfect contact of the scaled specimens. By choosing even lower friction coefficients the reproduction of the experiments settlement levels is expected to become more accurate.

It is concluded that, under the action of a vibratory source, settlement events between the cones of the slip-joint can be achieved. With the use of experiments and numerical modelling, it is demonstrated that excitation at frequencies equal or close to natural frequencies of the slip-joint is key to the successful installation or dismounting of a slip-joint. The settlement behaviour induced by vibrations is observed to be a stick-slip process that finally stabilizes at a level of equilibrium; this stabilization is observed in the predictions of the numerical models and in the experiments. Overall, the author hopes that this thesis will pave the way to the successful application of the innovative slip-joint connection in the next generation of offshore wind turbines.

CONTENTS

1

INTRODUCTION

1.1. THE FUTURE OF OFFSHORE WIND TURBINES: WITH OR WITHOUT A MONOPILE?

Offshore power generation via wind is a relatively young and rapidly growing industry. The first large-scale offshore wind farm, called Horn Rev, was built off of the coast of Denmark in 2002. From 2002 onward, the yearly installed capacity of offshore wind power in Europe has grown from 170 MW in 2002 to 3,019 MW in 2015 (Ho et al., 2016). The number and size of installed offshore wind farms will likely grow over the coming years in order to achieve the EU's goal that, by 2030, 27 percent of the energy consumed within the region will be produced by renewable energy sources. The majority of the existing offshore wind turbines (OWT) are based on the design used at Horn Rev. The basic building blocks of such an OWT are a monopile foundation (MP), a transition piece (TP) with a vertically positioned grouted connection, a turbine tower, and a turbine. An illustration of such an OWT is provided in Figure 1.1.

Of the 2,653 offshore turbines that were installed by the end of 2015, 80 percent are supported by the same foundation type: the monopile (Ho et al., 2016). Compared to the alternatives, such as gravity-based structures and jackets, the monopile features a relatively simple design and manufacturing process. Furthermore, the experience of the offshore industry with piles and pile driving plays an important role in the preference for the use of monopiles in shallow to medium water depths.
However, despite the current dominance of the monopile, its future application is uncertain. Thus far, the monopile has been applied at offshore wind farms in relatively shallow waters ($\leq$ 35m) for turbines that generate up to 5 MW. Turbine sizes and corresponding weights have continued to increase since the first offshore wind farm was installed. In 2015, the average installed capacity of offshore wind turbines was 4.2MW (Ho et al., 2016). Sieros et al. (2012) investigated the upscaling of turbines and demonstrated that 20 MW turbines are technically feasible. However, such upscaling comes at the cost of an unfavourable increase in the mass of the rotor nacelle assembly (RNA). This upscaling

1

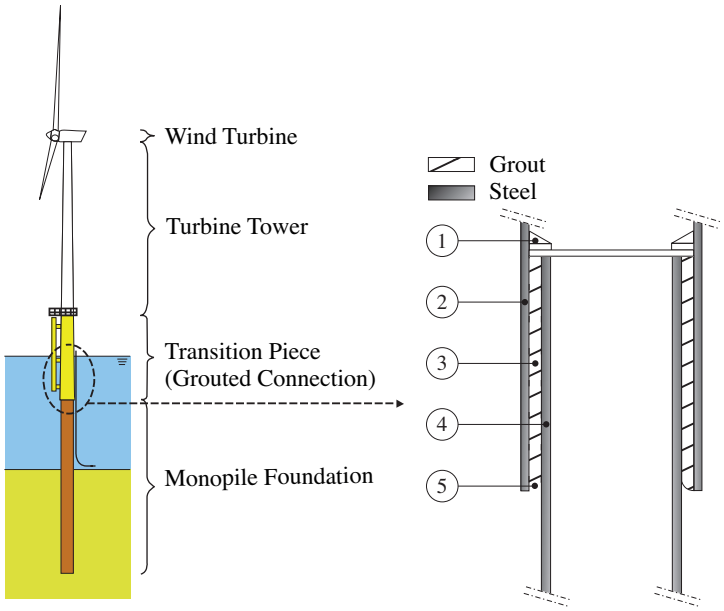

Figure 1.1: An offshore wind turbine with details of a grouted connection: 1) Temporary supports for the grouting process; 2) Transition piece; 3) Grout annulus; 4) Monopile; 5) Grout seal.

effect is illustrated in Figure 1.2(a), in which the exponential growth in RNA mass with respect to the rotor diameter sizes of the existing turbine designs is depicted. In addition to the increasing size and mass of wind turbines, offshore wind farms have been placed further offshore and in deeper waters (Ho et al., 2016). These two developments require monopiles that are longer and have larger diameters; therefore, they are significantly heavier than those that were used before. The weight and diameters of the piles are slowly reaching the industry's limits in terms of manufacturing and the lifting capacities of dedicated wind installation vessels.
Figure 1.2(b) depicts the water depth records of the monopile over time. The water depth record shown in this Figure represents the monopile foundation of the Veja Mata offshore wind farm, which was installed at a depth of 41 m in 2017 (4c offshore, 2016). The trend line indicates that, in the future, it can be expected that the monopile will be used in even deeper waters.

The question as to the limits of the applicability of the monopile foundation is still being debated. Schaumann and Böker (2005), and de Vries and Krolis (2007) have demonstrated that support structures with larger diameters and thus greater mass are required for the application of a monopile in greater water depths. Neither group of authors, however, identifies a limit for the applicability of the monopile. Seidel (2010) states that monopiles may be used for turbines larger than 5 MW and up to a water depth of 40 m. Segeren and Diepeveen (2015) investigated the influence of the RNA mass of a 5MW turbine on the design of monopiles at water depth of 30 m and 50 m; they noted

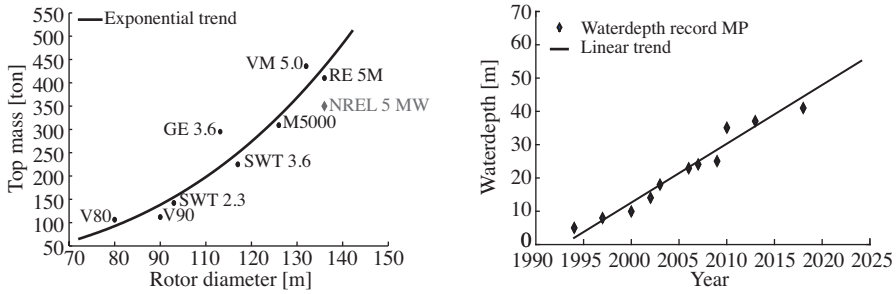

(a) Top mass versus rotor diameters (Diepeveen, 2013).

(b) Water depth record of applied monopiles.

Figure 1.2: Illustration of the trends in both top mass (RNA) and water depth record of applied monopiles.

that the limit of monopile applicability is determined either by the lift capacity of wind installation vessels or the manufacturing limits with regard to the diameters of the piles. They concluded that using monopiles with heavier turbines in deeper waters will either lead to a need for a greater number of installation vessels with crane capacities of above 1000 tons, or to monopiles with diameters greater than 6.5 m that consist of multiple lighter sections to reduce the crane capacity demands. One can imagine that piles of 100 m in length and 8 m in diameter will be difficult to move, lift, drive, and thus to install.

Beyond the aforementioned challenges the future of the monopile became even more uncertain when it was discovered that the grouted connections, an example of which is depicted in detail in Figure 1.1, were failing at the majority of the installed monopiles (NoordzeeWind, 2010; de Vries, 2010). Failure of the grout causes the transition piece to settle progressively; if this settling is not resolved, multiple problems will likely arise. New stress hotspots in joints, which were not accounted for in their design and which will lead to a decrease in the service lives of foundations, may be formed. Furthermore, settlement will decrease the height of access platforms moving them into the wave splash zone. As a consequence, a platform could be hit, and possibly damaged, by waves during storm conditions. Finally, settlement will decrease turbine height, resulting in a turbine producing lower power outputs.

The discovery of the grout problem triggered research into the cause of, and possible solutions to, this problem (DNV, 2011a; Lotsberg et al., 2012). These investigations, which included several joint industry projects, resulted in a revision of the Det Norske Veritas offshore standards for the design of wind turbine structures in 2011 (DNV, 2011b). The revision recommends that axial loads should be transferred through the connection between the foundation and the turbine tower in an alternative way than the grouted connection. One of the proposed solutions is that the pile should have a small angle relative to the vertical in order to prevent slippage.

1

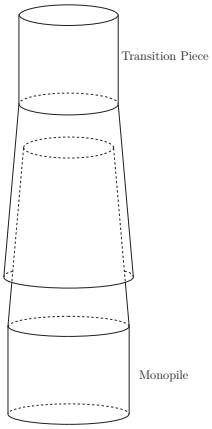

(a) The slip-joint concept, an alternative for the grouted connection.

(b) The Windmaster turbine at Scheveningen.

(c) The Aeroman turbine at Herrendeich - Nordstrand, Germany (wind-turbine-models.com, 2014).

Figure 1.3: The slip-joint concept and two existing onshore turbines with a slip-joint connection.

A promising solution that incorporates this small angle relative to the vertical is the slip-joint. The slip-joint consists of two conical sections made of steel, of which one is the conical bottom of the transition piece and the other is the conical top of the monopile. The dimensions of the slip-joint are chosen such that the cones fit closely into each other (see Figure 1.3(a)). Using this approach, there is a steel-to-steel connection, and the use of grout can be avoided altogether. By avoiding the usage of grout, the current issues associated with grout capacity can be overcome. This saves on grout material and creates a reduction in the diameter of-, and the steel required for the transition piece. Another potential benefit is the reduction in installation time by the elimination of the grouting process and the need to wait for the grout to set before the foundation can be loaded.

The use of the slip-joint will allow monopiles of more than 1000 tons to be constructed of a number of lighter sections of very large diameters. Using this approach, the applicability of the monopile can be extended to deeper waters and for turbines that have very large rotors and power capacities. Another benefit of the use of lighter sections is that the bulk of the existing lift vessels dedicated to offshore wind can be used for the installation of monopiles. The use of the slip-joint therefore solves the grout issues and provides the industry with a means of continuing to apply their preferred support structure: the monopile.

1.2. IS THE SLIP-JOINT A SOLUTION?

Although the slip-joint connection has been used successfully in the past for onshore wind turbines, it has not yet been used offshore. If the slip-joint could be successfully

applied offshore, a competitive and promising alternative to the grouted connection will be put forward. Load transfer through the joint is an essential part of a slip-joint's function. To permit this transfer, appropriate contact between the cones is necessary; the upper cone needs to be installed onto the lower cone. One approach to installation is dropping the upper cone onto the lower cone. This approach has been used during onshore installation of the slip-joint. This method is considered to be undesirable in offshore applications as a result of the risk of damaging the connection or even the adjacent parts of the pile and the uncontrollable nature of the method. The challenge thus lies in allowing the upper cone to move/slide in a controlled manner.

A high-potential and novel solution that is proposed in this thesis is causing the upper cone to move in a controlled manner by means of the application of a vibratory load at the top of the upper cone; this load will cause a slippage at the upper cone. It can be expected that the use of vibrations of frequencies that are close to a relevant natural frequency will lead to desirable settlement. Such a method would not only be effective when installing a slip-joint, as it could also be used for remedial manoeuvres and dismounting purposes. This new method of connecting joints requires further investigation, as it is necessary to determine how vibrations lead to the relative motions of the two parts that need to be connected.

Beyond the installation method, the imperfections of the cones and their surfaces influence the contact that is achieved between them. Imperfections of the cones can result from manufacturing tolerances, deformations caused by pile driving and as a consequence of the manner in which the cones are handled. Such imperfections can lead to undesirably limited contact areas between cones; reduced contact areas lead to higher stresses in a joint which will affect its lifetime.

In this thesis, it is proposed that a slight difference in cone angles be used to reduce the effect of the aforementioned imperfections. A steeper cone angle is used for the TP relative to that which is used for the MP; these slightly different cone angles require the upper cone to deform elastically in order to slide down. Using this approach, it becomes possible to form contact at points on the surface that feature imperfections and deformations. As a result, the area of contact will be increased as compared to cones with equal cone angles, which will have a positive effect on the load transfer through the joint. To achieve this positive effect, however, a controllable installation method is required.

1.3. THESIS AIM AND RESEARCH STRATEGY

The objective of this thesis is to investigate the potential of the use of vibrations for the installation and dismounting of a slip-joint with slightly different cone angles. To this end, the current status of research into slip-joints is first investigated. The history of the slip-joint and the similar types of connections that are used in other fields provide knowledge concerning the basic working principle of the joint and the envisaged challenges and advantages of its offshore use.

To capture the basic behaviour of a conical cylinder that is subjected to vibrations, a simplified semi-analytical model is proposed. The results of the model provide insight into the basic aspects of the sliding behaviour of the cone and the possible influence of the frequency and amplitude of vibrations on settlement.

Subsequently, the objective is considered from an experimental perspective with the aim of assessing the effectiveness of a vibration-assisted installation. Additionally, these experiments are executed in order to investigate the validity of the simplified model and to prove the validity of the concept of the use of vibration-induced settlement for installation and dismounting purposes. By means of a detailed experimental modal analysis of the specimens used in the experiments, insight into the structural modes that can be excited to effectively initiate sliding is obtained. Detailed measurements of the dimensions of the joint capture the quality of the manufactured cones that are used in the experiments. Based on the measured geometry, it is possible to make a prediction of the development of contact throughout the installation process.

As a final step, a finite element model, with the aim of reproducing the results of the experiments, is developed. This model captures the behaviour of the cones under the influence of vibrations in greater detail, when compared to the lumped mass model.

1.4. OUTLINE OF THIS THESIS

Figure 1.4 presents a diagram of the thesis layout. For each chapter a short description of the objectives and the chosen approach is given.

Chapter 2 reviews the current status of knowledge regarding the slip-joint. The slip-joint principle, its history, and its applications in other industries are discussed. Subsequently, a more detailed overview of the advantages and challenges associated with its offshore use is provided.

Chapter 3 presents a semi-analytical model of the sliding behaviour of conical steel cylinders under harmonic loads. This chapter first describes the dynamics of a conical cylinder in a simplified manner. A new method intended to describe the complex interaction that occurs between the two conical sections that are in contact and stick and slide is introduced. The model developed provides insight into the influence of the frequency and amplitude of a vibratory force on settlement behaviour in a qualitative manner. The influence of the dimensions of the individual cones and design assumptions regarding the sliding behaviour is investigated by means of a parametric study.

Chapter 4 presents the experiments performed in order to provide insight into the actual behaviour of a slip-joint with different cone angles that is subjected to vibrations. The experiments also provide proof of the concept of vibration-induced settlement. First, scaling and its effect on the design of the experimental setup are discussed. Second, the test case and the resulting experimental set up are presented. Subsequently, the observations of the installation and dismount tests are presented. The experimental data

provides the opportunity to investigate the changes that occur in the dynamics of the structure as settlement increases. By means of an experimental modal analysis, further insight is gained into which vibrational modes are effective for settlement purposes. Additionally, the exact dimensions of the test pieces are measured in order to identify their manufacturing tolerances and imperfections. Based on the measurements, predictions are made concerning where the two cones will first 'touch' and how the contact surface may develop as a function of settlement.

Chapter 5 focuses on a finite element model that describes the settlement of a slip-joint under the influence of vibration in greater detail when compared to the model discussed in Chapter 2. First, the model is presented, and the choices made in terms of modelling are explained and motivated. Second, the experiments conducted in Chapter 4 are simulated using the finite element model. It is demonstrated that the behaviour of the cones observed during experiments can be qualitatively reproduced using the model. A parameter study that demonstrates the sensitivity of the model to uncertainties concerning element size, friction, and damping is presented. It is shown that this model can approximate the settlements obtained in the experiments using a low friction coefficient.

Finally, in Chapter 6 the main conclusions are summarized.

Thesis Objective

Investigate the potential of the use of vibrations for the installation and dismounting of a slip-joint with slightly different cone angles.

Sub objective	Approach	Chapter
Determine the current status in slip-joint research.	Investigate the history of the use of a slip-joint and similar joint types in various industries. Investigate the challenges and opportunities of the slip joint.	2 Background slip-joint
Investigate the sliding mechanism of a slip-joint subjected to vibrations.	Based on simplified models of contact and friction, the mechanism of sliding is modelled.	3 Lumped mass model
Experimentally identify the mechanism of settlement of a slip-joint under the influence of vibrations. Prove and investigate the efficiency of vibration-induced settlement.	Settlement experiments with two types of shakers. Experimental modal analysis of the individual and combined system. Measurements of the dimensions of one set of cones.	4 Experimental investigation
Investigate the possibility to model the observed behaviour in the experiments with finite element software. Reproduce the result of the experiments.	Set up a finite element model of the joint. Investigate the model's uncertainties and reproduce the experimental results.	5 Finite element model

Figure 1.4: Overview of the objectives and approach per chapter.

2

THE SLIP-JOINT: CONNECTING (OFFSHORE) FOUNDATIONS AND WIND TURBINES

2.1. INTRODUCTION

The slip-joint presents a new and inspiring approach to connecting a foundation pile to a turbine tower. While this type of connection did not originate from the offshore industry, it has a promising future when applied to wind turbines. The principle of using friction in a connection is applied in various industries and this principle can be considered to be proven technology.

This chapter has two goals: The first is to provide an overview of the history of the slip-joint and the use of similar principles in other industries; this is presented in Section 2.2. The second goal is to provide a more detailed overview of the opportunities and challenges associated with the offshore application of the joint; these opportunities and challenges are discussed in Section 2.3. Ensuring a proper fit of the cones despite manufacturing tolerances and the deformations that may result from pile driving is discussed. In Section 2.4, background information is provided concerning why the use of small differences between the cone angles could present an innovative solution. In addition, the options with regard to installing such a joint using current offshore industrial capabilities are discussed in this section.

2.2. AN OVERVIEW OF THE CURRENT KNOWLEDGE ON THE SLIP-JOINT CONNECTION

2.2.1. THE SLIP-JOINT IN THE ONSHORE WIND INDUSTRY

The principle of the slip-joint connection is fairly simple: It resembles two cups that are fitted together. The bottom section of a slip-joint is connected to the monopile and the upper section to the transition piece, as illustrated in Figure 2.1. For stability and load

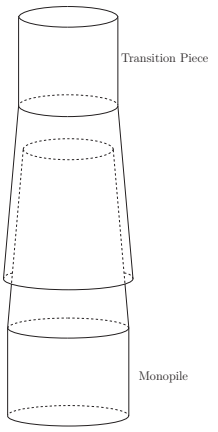

Figure 2.1: The slip-joint.

transfer, the connection relies on friction between the steel-to-steel contact surfaces. The frictional forces between the contact surfaces result from the weight of the structure and the overturning moments resulting from an operational wind turbine. The normal forces have the same origins and are further enhanced by the hoop stress. An important difference when compared to the grouted connection, is that the axial load capacity of a slip-joint depends on the cone angle; in contrast to the vertically grouted connections, the axial load capacity of a slip-joint only marginally depends on surface irregularities. In Figure 2.2 the static load transfer in terms of the forces acting on the monopile part of the slip-joint is illustrated.

The use of the slip-joint connection for wind turbines was first introduced by Windmaster in its onshore turbines in the 1990s. In their turbines, the slip-joint connects two sections of the tower. It was quite innovative to not use a bolted connection, as this approach was, and still is, used by other onshore turbine manufacturers in their towers. In 1998, Windmaster was taken over by Lagerwey which resulted in the end of the use of the slip-joint. One of the last functional Windmaster turbines was the *'Duinvogel'*; situated at Scheveningen, the Netherlands, it was installed in 1995 and was operated by Eneco. In April 2014, having reached the end of its operational lifetime, this turbine was dismantled (see Figure 2.3(c)). The dismounted tower which contains the slip-joint of *'Duinvogel'*is currently stored at one of the yards of Van Oord Contractors awaiting further investigation.

Van der Tempel and Schipholt (2003) explored the possibility of using the slip-joint for offshore wind turbines in 2003. Using basic calculations, they showed that the use of a slip-joint could reduce the installation time and the overall costs associated to such turbines when compared to the use of bolted connections and grouted connections. They also explored the interior of the tower of the *'Duinvogel'* after eight years of operation and found that the joint had settled an acceptable 5 cm (see Figure 2.3(a)). While the slip-joint already showed potential benefits back in 2003 it did not lead to

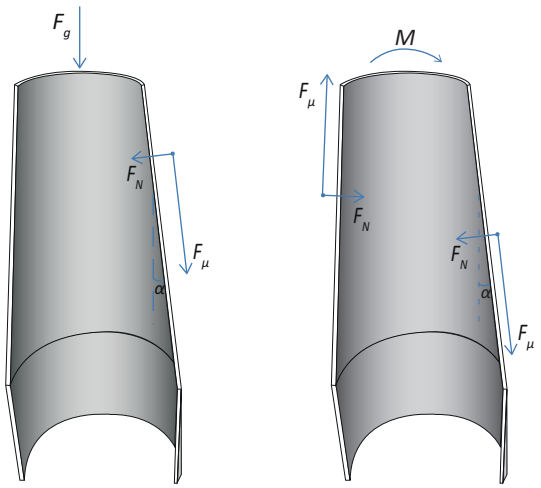

Figure 2.2: Transfer of the axial load F_g and overturning moment M shown in terms of the forces acting on the monopile part of the slip joint; F_μ is the friction force and F_N is the normal force.

the development of any prototypes for offshore use. At Delft University of Technology the research into the slip-joint was resumed in 2011 when the problem associated with the use of a grouted connection became publicly known. In order to check the status of the *'Duinvogel'*, Eneco Services took a new photo of the same slip-joint location as that featured in Van der Tempel's photo at the request of Delft University of Technology in 2011. Figure 2.3(b) depicts the interior of the slip-joint after 16 years of operation. When the two settlement levels were compared it was concluded that no settlement had occured after 2003.

In the wind industry a connection similar to the slipjoint has been used in the past by MAN for their onshore turbines. The MAN Aeromann turbines were manufactured by MAN Maschinenfabrik Augsburg-Nürnberg in Germany. Their small-sized onshore turbines, which have power production capacities up to 40 kW were supported by towers of an octagonal shape and included a slip-joint, or as they referred to it in German: a *'Schachtelstoss'*. Figure 1.3(c) shows a photograph of the 20 kW Aeroman at Herrendeich in Germany, in which the octagonal slip-joint is depicted. This type of connection worked well and it was originally intended that a weld be added at the end of the overlap to ensure the stick positions. This was, however, not done as the operators of the turbine felt that was unnecessary. Similarly to the slip-joints used in the Windmaster turbines the *'Schachtelstoss'* settled slightly during the period of time in which the turbine was operational (Segeren and Hintz, 2015).

2.2.2. APPLICATIONS OF THE SLIP-JOINT IN OTHER INDUSTRIES

Beyond the use of the slip-joint in the wind industry, similar types of connections are found in other industries. The *'Schachtelstoss'* for example was also used in German electricity masts and light poles prior to its use in turbines. A German guideline dating

(a) In 2003.

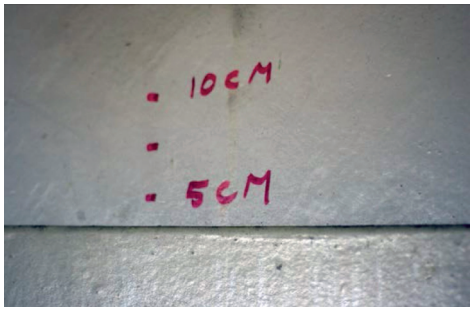

(b) In 2011.

(c) Dismantling of the tower.

Figure 2.3: (a,b) Inside the turbine tower at the location of the slip-joint of the 'Duinvogel' turbine, Scheveningen (van der Tempel and Schipholt, 2003), (c) Photograph of the 'Duinvogel' turbine tower being dismantled.

from 1931 recommends that this connection type be used to join sections of an electricity mast (Stockinger, 1931). Even today, Valmont, a manufacturer of light poles, uses the *'Schachtelstoss'* to connect the two sections of some of their light poles (Valmont, 2015).

Similar connection types are found in drilling and machining. For the purpose of drilling rock, this joint is called a conical friction joint. In the past, drill bits were in some cases connected to drill rods by means of conical friction joints. Nordlund and Lundberg (1986), among others, studied the effect of impact-induced loads on the stability of such joints.
An example of a similar joint that is used in machining is the cone-clamping element (see Figure 2.4(a)). This element connects a hub and a shaft for the purpose of transferring torque.

Another example is the machine taper that is used to secure tools for cutting or other machining activities. This type of joint functions in a manner similar to that of the slip-joint; however, in this case the two sections (the male and female part) are not thin-walled but are more solid. Figure 2.4(b) depicts the Jacob taper holder, which is one of the taper holders that are frequently used for the securing of drill press chucks. The friction-based joint principle is thus used in various industries, and it can be considered a proven solution for (temporarily) connecting two separate conical parts.

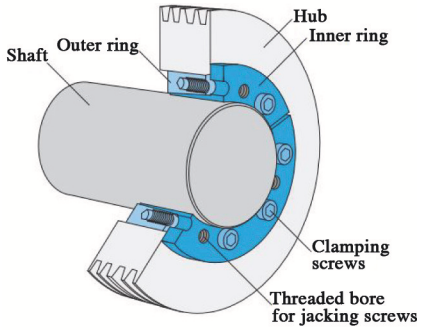

(a) Cone clamping element (Ringspann, 2011)

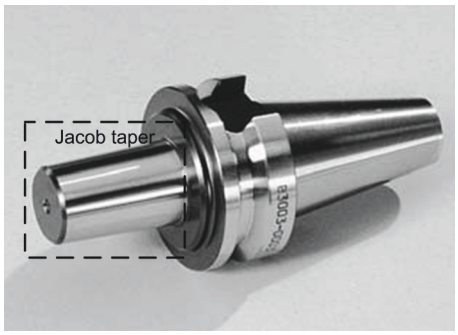

(b) Jacob taper holder (Nikken, 2015)

Figure 2.4: Examples of connection types in machining with similar working principle as the slip-joint.

2.3. THE SLIP-JOINT IN OFFSHORE CONDITIONS

In Windmaster's onshore turbines, slip-joints connect sections of the turbine towers and are therefore located relatively close to the turbines. Offshore, the joint is envisaged to connect foundations with turbine towers and to enable foundations to be comprised out of multiple sections. As such, it represents an alternative to the grouted connection. When compared to both the onshore application of the slip-joint and the traditional grouted connection, the offshore environment presents a number of opportunities and challenges, which arise in the design, installation, and operational phase of a joint. These opportunities and challenges are discussed with reference to the traditional grouted connection in the following subsections.

2.3.1. OPPORTUNITIES

1. Reduction of steel and grout: The use of the slip-joint removes the need for grout and reduces the amount of primary steel required as a result of the reduced diameter of the transition piece;

2. The possibility of dividing the monopile foundation into two or more sections: This possibility provides opportunities for the industry that focuses on manufacturing, transporting, and installing monopiles. By dividing a monopile into lighter sections, its diameters can increase beyond current manufacturing and handling limits, and stay within the lifting capacity of the majority of the existing wind installation vessels (Segeren and Diepeveen, 2015). This allows monopiles to be used in deeper waters and accommodate heavier/larger turbines;

3. Faster installation of the transition piece: A potential reduction in installation time can be realized by avoiding the grouting process. This process takes, on average, approximately 8 hours. Furthermore, the grout needs to harden for approximately 28 days before a turbine tower can be installed. With the use of the slip joint the grouting process and its hardening time is omitted; and

4. Prevention of progressive settlement: Given the conical shape of the joint, the extent of possible settlement is limited. In the case of the traditional vertical straight cylinders, the settlement that may have occurred had to be stopped by the introduction of an additional support that allowed the axial load to be transferred through the joint.

5. Decommissioning of the joint: The slip joint has the potential opportunity to be decommissioned after its lifetime using a reverse installation procedure. As compared to the grouted connection, which has to be cut offshore, this ability of the slip joint may reduce the required time, equipment and the related cost of its removal.

2.3.2. CHALLENGES

During the lifetime of a slip-joint the following factors need special attention:

1. Pile driving on the lower cone of the slip-joint: Pile driving on the conical section of a friction-based connection such as the slip-joint has not been done previously.

The deformation that may occur to the top part of the conical section that is subjected to hammering has not yet been investigated, and it is therefore uncertain whether these deformations will be acceptable. The heavy blows, involved in such pile driving may cause plastic deformation of the top of the cone to such a degree that the angle of the cone may become non-uniform along the height. Any resulting deformation will affect the contact between the surfaces and thereby load transfer through the joint;

2. Installing the upper cone of the slip-joint onto the lower cone of the foundation pile in a controlled manner: After the foundation pile is driven into the ground, the upper cone of the connection needs to be placed on top of the lower part. To ensure a proper fit, the one should slide into the other. Onshore, this has previously been done by dropping the upper cone from a certain height (van der Tempel and Schipholt, 2003); offshore, however, this method does not seem desirable, as the risk of damaging one of the cones is present. Driving the upper cone by striking the top with a hammer also poses the same undesirable risk. It may also be more difficult to position the upper section of the slip-joint offshore when compared to onshore. This is mainly due to the difference in manoeuvrability that occurs as a result of an offshore location and how accessible such locations are for lifting cranes;

3. Assumptions regarding effective contact areas when analysing the ultimate and fatigue-limit load cases: Depending on the load direction and magnitude the degree of contact between the surfaces of the cones can change in operation. Other factors that influence contact between the cones are the local deformations that may occur as a result of the manufacturing tolerances involved in the creation of the cones and the possible deformations that may be caused by the pile driving the top of one of the cones. For load calculations, an assumption regarding the contact area that will determine the stresses in maximum and fatigue loading that are expected during the lifetime of a joint needs to be made;

4. Correction of a potentially misaligned foundation pile: Most monopiles have a small inclination with respect to the vertical after the pile is driven into the soil. This misalignment normally is corrected with the use of a grouted connection. With a slip-joint, however, this inclined foundation pile imposes two challenges: one is the installation of the upper cone on the inclined lower cone, while the other is correcting for the inclination;

5. Corrosion in the gaps between the cones: The offshore environment in which slip-joints could be used results in a high risk of corrosion. Contact within a slip-joint will not be uniform due to surface imperfections, the presence of welds, and deformations caused by loads and pile driving. Furthermore, the presence of water and air in the gaps may cause corrosion. Corrosion of the joint will reduce the wall thickness locally. At these corroded locations, the structural strength will naturally also be reduced; and

6. Access to the turbine: The slip-joint is an alternative to the grouted connection in a transition piece. Currently, this transition piece provides access to the turbine by

means of an attached boat landing. A similar access point must be attached prior to or after the installation of a slip-joint.

Proper load transfer is crucial for the functioning of a slip-joint. Load transfer is dependent on the contact achieved between the two surfaces. This contact is affected by manufacturing tolerances, the deformations that may result from pile driving, and the installation of the joint. In order to address the imperfections in the geometry that may be caused by manufacturing and pile driving, the use of a slip joint that features cones with unequal cone angles is proposed.

2.4. THE USE OF CONES WITH UNEQUAL CONE ANGLES IN AN OFFSHORE SLIP-JOINT

If the lower cone angle of the transition is slightly larger as a result of imperfections and/or pile driving, the bottom of the overlap may lose contact; this is illustrated in Figure 2.5. In such case, the area of load transfer will become smaller. Furthermore, the areas located at the bottom and where no contact is present could quasi-periodically collide with each other as a result of the vibration of the turbine.

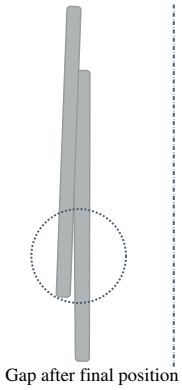

Figure 2.5: Final position of a slip-joint where the cone of the MP part is steeper than the TP part.

It would therefore be beneficial to manufacture the two cones of a slip-joint with a slight difference in cone angles (see Figure 2.6(a)). When using this approach the upper cone needs to deform elastically in order to slide down (see Figure 2.6(b)); thus, it would become possible to make contact at locations along the surface that may feature imperfections. Furthermore, the effect of the deformations that may have occurred as a result of the installation process will also be reduced due to a relatively high elastic stress. This will increase the area of contact, thus having a positive effect on the load transfer through the joint.

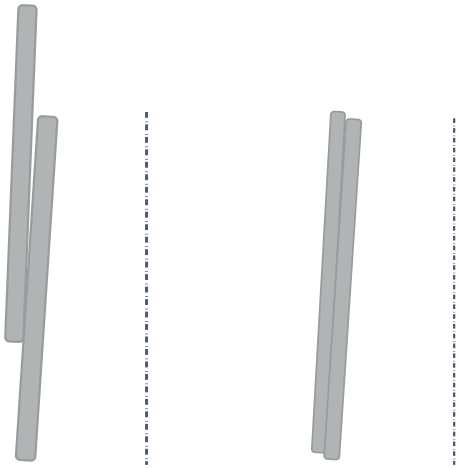

(a) Upon initial contact.

(b) After full installation.

Figure 2.6: The contact of a slip-joint with a steeper cone angle of the TP compared to the MP part.

2.4.1. THE OFFSHORE INSTALLATION OF A SLIP-JOINT

After a foundation pile is driven into the soil the upper part of the slip-joint will be placed over its lower part, which is positioned at the top of monopile. There are multiple options for connecting the joint: It can be connected using the weight of the upper cone, by dropping the upper cone from a certain height, by hammering, or by settling the upper cone axially using a vibratory device.

Connecting a joint using the self-weight of the upper cone can be done by means of the controlled lowering of the upper part onto the lower part of the slip-joint. This would be risky, however, because the joint will most likely not slide down sufficiently far to reach a fully stable position. Therefore, it may move laterally or rotate when the pile is subjected to wave loading. Furthermore, when the turbine sections and the turbine are placed on top of the upper part, there is a risk that the joint will settle further. This would cause a sudden slip during the installation process. This is undesirable for any lifting crane, not to mention the individuals working on the turbine at that moment. To prevent this sudden slip, a somewhat different installation method may be desirable.

Dropping the joint from a height was the method used onshore for the slip-joints in the Windmaster turbines. Offshore, however, this method would be undesirable, as there is an associated risk of damaging the joint in the process; in addition, the offshore environment presents more challenges for installation in comparison to onshore conditions.

Installation by hammering uses a hydraulic hammer to issue blows that are intended to achieve additional settlement to the top of the TP. Although it has been successfully used in the past for driving piles into the seabed, such hammering is undesirable given the risk of damaging or deforming a joint during the process.

Another possible approach involves the use of a vibratory device, such as the CAPE CV

230 (CAPE Holland, 2015), to create a vibration-induced movement of the slip-joint in the axial direction. Such vibratory devices use vibrations to drive (mono)piles into the soil and could be adopted for offshore use. This method is deemed to be preferred over the other alternatives, as it will allow for a controlled settlement of a slip-joint to the fully stable position. A vibratory device could also potentially be used to adjust and to dismount a slip-joint when required.

2.5. CONCLUDING REMARKS

Although it has been applied onshore, the slip-joint has to date not been used offshore. The essential factor for a successful joint is a proper fit. To make contact at points along a surface that features imperfections, a slip-joint with slightly unequal cone angles is proposed to be used. To ensure a proper fit it is desirable to adjust the position of the cones and maximize the contact area between them in a controllable manner. A potential solution is to make the upper cone move in a controlled manner by introducing vibration at its top. The installation of a slip-joint using vibrations has the potential to ensure a proper fit of the cones and, additionally, to provide a corrective measure for errors during installation. Furthermore, vibrations can be used to assist during the decommissioning phase of a cone. This new method for connecting sections of piles with slip-joints has not yet been developed and requires research. In the next chapter, vibration-assisted installation is pre-studied by means of a semi-analytical model. The results from the conducted experiments aimed to investigate the use of vibrations during installation and dismount are presented in Chapter 4.

3

A LUMPED-ELEMENT MODEL OF THE VIBRATION-INDUCED SETTLEMENT OF A SLIP-JOINT CONNECTION

3.1. INTRODUCTION

The objective of this chapter is to pre-study several installation procedures of a slip-joint as a basis for the development of the experiments presented in the next chapter. A simplified lumped-element model of a slip-joint connection is developed in order to qualitatively investigate the behaviour under the following installation conditions: self-weight only, dropping of the upper cone and vibration-assisted installation.

The model composition, assumptions, and simplifications are introduced in Section 3.2, while the governing equations are presented in Section 3.3. In Section 3.4, a parametric study of the model predictions is conducted with reference to the dimensions and loading details of a selected offshore wind project.

3.2. MODEL DESCRIPTION

3.2.1. ASSUMPTIONS

The first assumption made is that the installation process of a slip-joint preserves the axial symmetry. Given this assumption, it is acceptable to represent the two conical cylinders as two lumped elements as shown in Figure 3.1(a). The effective stiffness of the entire upper cone, at its point of contact with the lower cone, is represented by a linear translational spring and a linear rotational spring with stiffnesses K_{r} and K_{rot}, respectively (the derivation of these stiffnesses is elaborated upon in Section 3.2.2).

Parts of this chapter have been published in 'Investigation of a slip joint connection between the monopile and the tower of an offshore wind turbine', IET Renewable Power Generation, Special Issue: European Wind Energy Association 2013, doi: 10.1049/iet-rpg.2013.0163, (Segeren et al., 2014)

3

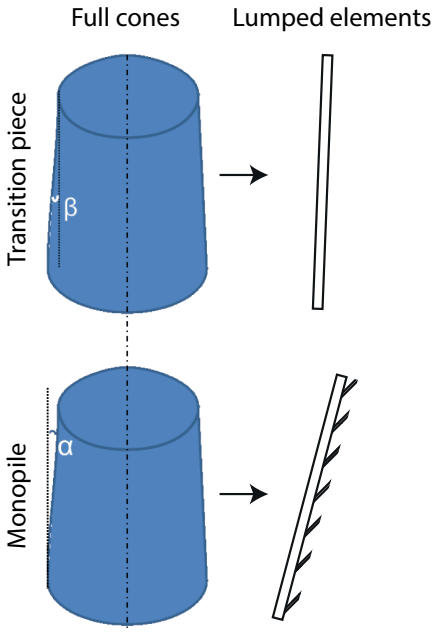

(a) Transformation.

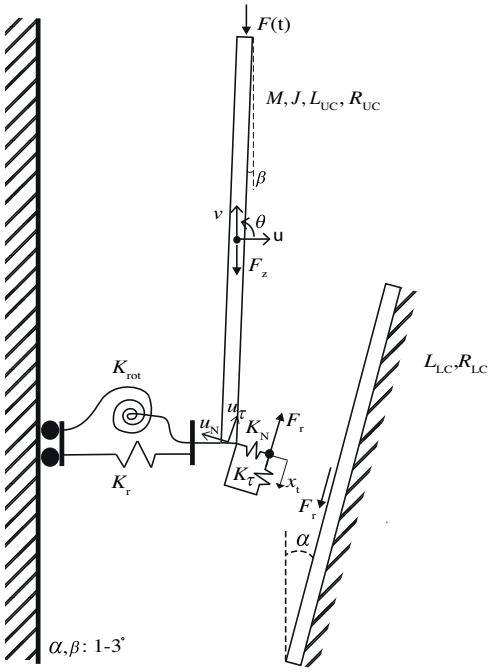

(b) The lumped element model with cone angles α and β, radius of the bottom of the upper cone R_{UC}, radius of the bottom of the lower cone R_{LC}, length of the upper cone L_{UC}, length of the lower cone L_{LC}, excitation force $F(t)$, gravity force F_{z}, displacement in tangential direction u_{τ}, displacement in normal direction u_{N}, mass of the upper cone M, mass moment of interia of the upper cone J, stick position along the surface of the lower cone x_{τ}, and the translational degrees of freedom of the upper cone v, u, and rotational degree of freedom θ.

Figure 3.1: (a) Transformation from full cones to lumped elements and (b) the adopted lumped model.

The flexibility of the lower cone is accounted for analogously; Effective contact stiffnesses in the normal and tangential directions are represented by two linear springs denoted as K_N and K_τ respectively (a detailed discussion of these stiffnesses is provided in Section 3.2.2 to 3.2.4).

The values of the effective stiffnesses are calculated numerically at their initial positions and are then kept constant throughout the simulation. Note, however, that in reality the effective contact stiffnesses change with the increase of the local cone diameter that occurs with the increase in slip distance: by not taking this variation into account, the effective contact stiffnesses are slightly different (as an example, in Section 3.4 a settlement of 40 cm is desired; this would affect the stiffnesses in normal and tangential direction with 0.5 percent and 6 percent, respectively). The resulting settlements presented in Section 3.4 are therefore to be taken as indicative.

In Figure 3.1(b), the adopted lumped model of the slip-joint is shown. Contact between the two bodies is assumed to be point-like. This is permissible, as the flexibility of the cones is taken into account by means of springs at the contact point. The last assumption of this model is that the two rigid bodies are initially in contact: Any velocity or acceleration of the upper cone at the start of the analysis is taken into account as an initial condition. Note that any misalignment between the cones cannot be taken into account in this model.

3.2.2. THE EFFECTIVE STIFFNESSES OF THE CONES

All spring stiffnesses are derived based on the theory of conical shells (Soedel, 2004). The flexibility matrix is obtained at the point of initial contact. For the upper cone, this contact point is, and remains, the lower edge of the conical shell. For the lower cone, this point depends on where it initially touches the upper cone. The translational and rotational effective stiffnesses of the upper cone are obtained by means of inverting the flexibility matrix. Section 3.2.3 provides the force balance equations and boundary conditions used to (numerically) calculate these effective stiffnesses as a function of the geometrical and material properties of the cone.

The translational stiffness of the upper cone, K_r, represents the resistance of the conical shell in the radial direction under the action of a unit force applied at the lower boundary in the direction normal to the surface of the cone. The rotational stiffness, K_{rot}, represents the resistance of the upper cone under the action of a unit moment applied at the lower boundary. The stiffnesses are obtained assuming the upper end of the upper cone to be clamped and the lower end to be free. The stiffnesses depend on the cone angle of the upper cone β, the radius of the bottom of the upper cone R_{UC}, the wall thickness h, the modulus of elasticity E, the Poisson ratio ν, and the length of the upper cone L_{UC} (see Section 3.2.3).

The contact stiffnesses K_N and K_τ represent the resistance of the lower cone to a line load applied along the circumference in the normal and tangential directions, respectively. The contact stiffnesses are obtained for a cone with a free upper and clamped lower

end. These stiffnesses depend on the geometrical and material properties of the lower cone. As mentioned previously, these stiffnesses are assumed to be constant and are not updated during the calculations.

3.2.3. THE FORCE BALANCE AND BOUNDARY CONDITIONS TO OBTAIN EFFECTIVE STIFFNESSES USING SHELL THEORY

In this section, a more extensive explanation as to the derivation of the effective stiffnesses is given. First, it is shown, using shell theory (Soedel, 2004), which force-balance equations and boundary conditions are used to calculate the effective stiffnesses of the upper cone. Subsequently, the effective contact stiffnesses for the lower cone are explained.

In Appendix A, Equations (A.1) to (A.3) define the static equilibrium for the tangential direction U_x, circumferential direction U_θ and normal direction U_3 of a conical shell in accordance with Soedel's work (2004). In Figure 3.2, the coordinate system of the conical shell is defined.

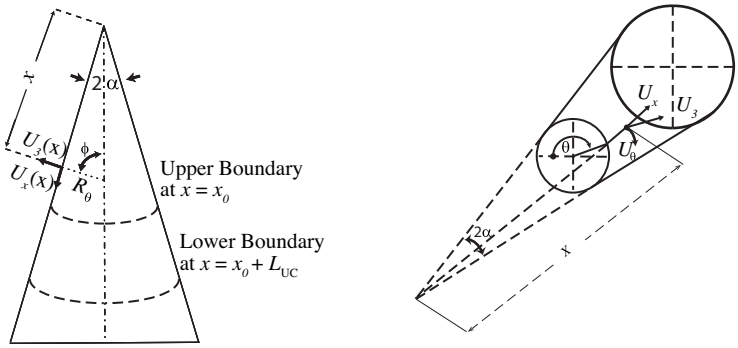

Figure 3.2: Coordinate definitions for a conical shell with cone angle α, the displacement in tangential direction U_x, in circumferential direction U_θ and in normal direction U_3.

To obtain the effective stiffnesses the following steps are taken:

1. Due to the assumed axial symmetry the circumferential force balance is automatically satisfied. Therefore, all derivatives with respect to the angle θ are set to zero;
2. Insert in (A.1) to (A.3) the relation between the stress and moment resultants and the strain that is given by (A.6) to (A.11); and following that
3. Insert in (A.1) to (A.3) the relation between the strain and displacement that is given by (A.14) to (A.21).

This results in the coupled ordinary differential equations (3.1) and (3.2) which give the force balance in the tangential and normal directions, respectively, as follows:

$$\frac{Eh\sin(\alpha)}{(1-\nu^2)} \cdot \left(-\frac{U_3'\nu}{\tan(\alpha)} - U_x''x - U_x' + \frac{U_3}{x\tan(\alpha)} + \frac{U_x}{x} \right) = 0 \tag{3.1}$$

$$-\frac{Eh\sin(\alpha)}{\tan(\alpha)(1-\nu^2)}f_1+\frac{Eh^3\sin(\alpha)}{12(1-\nu^2)}\left[f_2+f_3-f_4\right]=0 \tag{3.2}$$

where the distributed external loads q_x, q_θ, and q_3 are taken as zero and where f_1 to f_4 are defined by equations (3.3) to (3.6) in which $\frac{\delta}{\delta x}$ is denoted as $'$:

$$f_1=\frac{U_x}{x}+\frac{U_3}{x\tan(\alpha)}+\nu U_x^{'} \tag{3.3}$$

$$f_2=2\left(-U_3^{'''}+\nu\left(-\frac{U_3^{''}}{x}+\frac{U_3^{'}}{x^2}\right)\right) \tag{3.4}$$

$$f_3=x\left(-U_3^{''''}+2\nu\left(-\frac{U_3^{'''}}{2x}+\frac{U_3^{''}(x)}{x^2}-\frac{U_3^{'}(x)}{x^3}\right)\right) \tag{3.5}$$

$$f_4=-\frac{U_3^{''}}{x}+\frac{U_3^{'}}{x^2}-\nu U_3^{'''} \tag{3.6}$$

As the model is assumed to be linear, the force-displacement relation at the contact point (circumference) can be written in the following matrix form: $\left(\vec{\mathbf{x}}=\mathbf{F}\vec{\mathbf{f}}\right)$. Where $\vec{\mathbf{x}}$ is the displacement vector, $\vec{\mathbf{f}}$ is the force vector and $\mathbf{F}$ is the flexibility matrix. The latter is defined as follows:

$$\mathbf{F}=\begin{pmatrix}a_{1,1} & a_{1,2} & a_{1,3}\\ a_{2,1} & a_{2,2} & a_{2,3}\\ a_{3,1} & a_{3,2} & a_{3,3}\end{pmatrix} \tag{3.7}$$

The procedure used to obtain the terms of the flexibility matrix is as follows: The magnitude of term $a_{1,1}$ equals the tangential displacement (U_x) of the lower boundary under the action of a unit force, uniformly distributed along the circumference boundary that acts in the direction of x-axis (see in Figure 3.2). To obtain this term, equations (3.1) and (3.2) are solved using six boundary conditions given by equations (3.8) to (3.13). The upper cone is assumed to be fixed at its upper end, which is located at x=x_0=$\frac{R_{\mathrm{UC_T}}}{\tan(\alpha)}$ (see Figure 3.2), with $R_{\mathrm{UC_T}}$ being the radius of the upper end of the upper cone and α the cone angle of the upper cone. At the lower boundary (x=x_0+L_{UC}), with L_{UC} being the length of the upper cone, three line loads are defined (see Figure 3.3). The corresponding boundary conditions are given as follows:

Tangential displacement	$U_x(x_0)=0$	(3.8)
Normal displacement	$U_3(x_0)=0$	(3.9)
Rotation around x	$U_3'(x_0)=0$	(3.10)
Axial force	$N_{xx}(x=x_0+L_{\mathrm{UC}})=1$ N/m	(3.11)
Shear force	$Q_{x3}(x=x_0+L_{\mathrm{UC}})=0$ N/m	(3.12)
Moment over the edge	$M_{xx}(x=x_0+L_{\mathrm{UC}})=0$ Nm/m	(3.13)

The expressions for the distributed axial force N_{xx} in the direction of x, the distributed shear force Q_{x3} in the direction normal to the shell surface and the distributed moment M_{xx}, are given as follows:

$$N_{xx} = \frac{Eh}{(1-\nu^2)}\left(U_x' + \nu\left(\frac{U_x}{x} + \frac{U_3}{x\tan(\alpha)}\right)\right) \tag{3.14}$$

$$Q_{x3} = \frac{Eh^3}{12(1-\nu^2)}\left(U_3''' + \frac{U_3''}{x} - \frac{U_3'}{x^2}\right) \tag{3.15}$$

$$M_{xx} = \frac{Eh^3}{12(1-\nu^2)}\left(U_3'' + \nu\frac{U_3'}{x}\right) \tag{3.16}$$

Solving the system of equations {(3.1), (3.2), (3.8)-(3.13)} results in a tangential displacement (U_x, term $a_{1,1}$), a displacement in the normal direction (U_3, term $a_{2,1}$), and a rotation (U_3', term $a_{3,1}$). As a result of the conical shape, the equations are coordinate dependent; therefore, they are solved numerically using the numeric computing environment Maple. The other terms of the matrix **F** are obtained analogously using loading conditions N_{xx}=0 Q_{x3}=1 M_{xx}=0 and N_{xx}=0 Q_{x3}=0 M_{xx}=1.
Using the parameters from Table 3.1, as an example, the following numerical values are obtained:

$$\mathbf{F} = \begin{pmatrix} 1.5\cdot10^{-9} & 1.0\cdot10^{-10} & -1.4\cdot10^{-12} \\ 1.0\cdot10^{-10} & 4.3\cdot10^{-9} & 1.3\cdot10^{-7} \\ -1.4\cdot10^{-12} & 1.3\cdot10^{-7} & 7.8\cdot10^{-7} \end{pmatrix} \tag{3.17}$$

The stiffness matrix **K** is calculated by means of inverting the flexibility matrix. Inverting matrix (3.17) results in matrix shown in equation (3.18), where the effective stiffnesses K_{r} and K_{rot} are represented by the values of positions $a_{2,2}$ and $a_{3,3}$ of matrix (3.18). In the model the off-diagonal terms are neglected, being at least a factor six smaller as compared to the diagonal terms, in the calculation as their effect on the qualitative behaviour is considered to be negligible.

$$\mathbf{K} = \begin{pmatrix} 6.6\cdot10^{8} & 3.2\cdot10^{7} & -5.3\cdot10^{6} \\ 3.2\cdot10^{7} & 4.6\cdot10^{8} & -7.6\cdot10^{7} \\ -5.3\cdot10^{6} & -7.6\cdot10^{7} & 2.5\cdot10^{7} \end{pmatrix} \tag{3.18}$$

Table 3.1: Design parameters of the slip-joint case study.

	Lower cone	Upper cone	Unit
Cone angle	α=1.05	β=1.0	°
Top outer diameter	5.84	5.947	m
Bottom outer diameter	6.00	6.104	m
Wall thickness	60	60	mm
Total mass		151	Tons
E	210	210	GPa
ν	0.33	0.33	-
K_τ	2.02×10^9		N/m^2
K_N	9.00×10^8		N/m^2
K_r		4.67×10^8	N/m^2
K_{rot}		2.56×10^7	N/rad

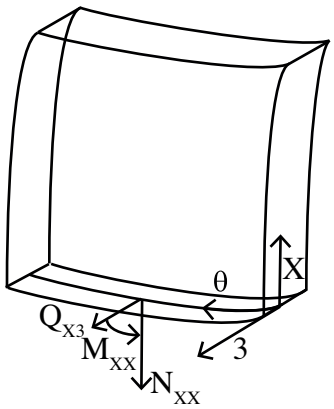

Figure 3.3: The boundary forces. The axial force N_{xx} in the direction of x, the shear force Q_{x3} in the direction normal to the shell surface, and the moment M_{xx}.

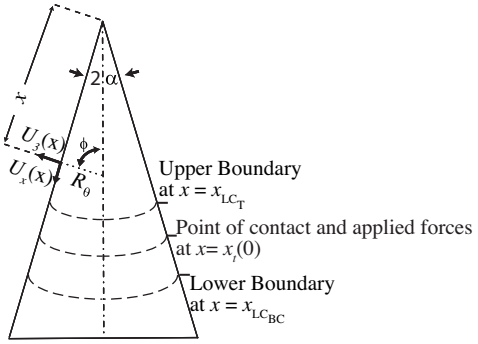

Figure 3.4: The position of the boundaries and the point of contact for which the stiffnesses for the lower cone are obtained.

3.2.4. THE EFFECTIVE CONTACT STIFFNESS OF THE LOWER CONE

The contact stiffnesses are obtained at the circumference of initial contact in a manner analogous to that used to obtain the stiffnesses K_r and K_{rot}, as described in the previous section. The upper end of the lower cone is assumed to be free and is located at $x = x_{LC_T} = \frac{R_{LC_T}}{\tan(\alpha)}$ (see Figure 3.4), with R_{LC_T} being the radius of the top of the lower cone, and α the cone angle of the lower cone. The lower end of the lower cone is assumed to be fixed and is located at x=$x_{LC_{BC}}$=$x_{LC_t} + 2L_{LC}$, with L_{LC} being the length of the lower cone. The location of the fixed boundary is chosen such that this boundary condition does not influence the local stiffness. External forces are applied at the circumference of contact to calculate the (local) stiffness at the contact points. The initial circumference of contact is located at the position where the inner diameter of the upper cone and the outer diameter of the lower cone match: ($x = x_t(0) = \frac{R_{UC_b} - t_w}{\tan(\alpha)}$), with R_{UC_b} being the radius of the bottom of the upper cone. The boundary conditions of the lower cone are given as follows:

Tangential displacement	$U_x(x_{LC_{BC}}) = 0$	(3.19)
Normal displacement	$U_3(x_{LC_{BC}}) = 0$	(3.20)
Rotation around x	$U_3'(x_{LC_{BC}}) = 0$	(3.21)
Axial force	$N_{xx}(x_t(0)) = 1\text{N/m}$	(3.22)
Shear force	$Q_{x3}(x_t(0)) = 0\text{N/m}$	(3.23)
Moment over the edge	$M_{xx}(x_t(0)) = 0\text{Nm/m}$	(3.24)

Solving the system of equations {(3.1), (3.2), (3.19)-(3.24)} results in a tangential displacement (U_x, term $a_{1,1}$), a displacement in the normal direction (U_3, term $a_{2,1}$), and a rotation (U_3', term $a_{3,1}$). The other terms of the matrix $\mathbf{F}_l$ are obtained analogously using loading conditions N_{xx}=0 Q_{x3}=1 M_{xx}=0 and N_{xx}=0 Q_{x3}=0 M_{xx}=1.

Using the parameters from Table 3.1, as an example, the following numerical values are obtained:

$$\mathbf{F}_l = \begin{pmatrix} 4.9\cdot10^{-10} & 3.2\cdot10^{-11} & 1.1\cdot10^{-10} \\ 3.2\cdot10^{-11} & 4.6\cdot10^{-8} & 1.9\cdot10^{-12} \\ 1.1\cdot10^{-10} & 1.9\cdot10^{-12} & 1.4\cdot10^{-8} \end{pmatrix} \tag{3.25}$$

By means of inverting the flexibility matrix (3.25), the stiffness matrix (3.26) is obtained.

$$\mathbf{K}_l = \begin{pmatrix} 2.0\cdot10^{9} & -6.0\cdot10^{7} & -1.7\cdot10^{7} \\ -6.0\cdot10^{7} & 9.0\cdot10^{8} & 3.7\cdot10^{5} \\ -1.7\cdot10^{7} & 3.7\cdot10^{5} & 7.1\cdot10^{7} \end{pmatrix} \tag{3.26}$$

The effective stiffnesses, K_τ and K_N, are represented by the values of positions $a_{1,1}$ and $a_{2,2}$ of matrix (3.26). The off-diagonal terms are neglected in the equations of motion presented in the next Section as the magnitude is an order smaller than the diagonal terms

3.3. STICK-SLIP EQUATIONS OF MOTION

The upper cone can respond to the gravitational and harmonic load in one of two ways: It can either stick to the lower cone at a given position, represented by x_τ in each stick-slip cycle, or it can start slipping/moving if the force in the tangential direction is greater than the maximum static friction force. Drawing on the similar systems presented and discussed by Den Hartog (1930), Popp (1998), and Hong and Liu (2000), a stick-slip system with a Coulomb friction force is introduced. In the following, the equations of motion (EOM) are derived for the lumped model of Figure 3.1(b), with friction force F_r. The Coulomb friction force is calculated as follows:

$$F_r = \begin{cases} \mu_d N & \text{if} \quad \dot{u}_\tau > 0 \\ \in [-\mu_s N, \mu_s N] & \text{if} \quad \dot{u}_\tau = 0 \\ -\mu_d N & \text{if} \quad \dot{u}_\tau < 0 \end{cases} \tag{3.27}$$

where μ_d, μ_s and N are the dynamic and static friction coefficients and the normal force, respectively. The friction coefficients μ_d and μ_s are the assigned values of 0.3 and 0.5, respectively. The friction force causes the motion of the slip-joint to be non-smooth and dependent on the tangential velocity.

For slip and stick, different EOM are set up using the displacement or so-called direct stiffness method (Cook et al., 2002). The system is linearised for small angles, meaning that $\sin(\theta) \approx \theta$, $\cos(\theta) \approx 1$. The multiplication of θ with a displacement is therefore $\ll 1$ and becomes negligible. The non-linear coupled EOM in the stick condition for the system shown in Figure 3.1(b) are presented in Equations (3.28) to (3.30) for the three degrees of freedom of the upper cone (u, v, θ).

$$\begin{aligned} M\ddot{u}(t) = &- K_r u(t) - K_r \left(\frac{L_{UC}}{2}\right) \sin(\theta(t)) - K_N u_N(t) \cos(\alpha) \\ &- K_\tau (u_\tau(t) - x_\tau(t)) \sin(\alpha) \end{aligned} \tag{3.28}$$

$$M\ddot{v}(t) = K_N u_N(t) \sin(\alpha) - K_\tau (u_\tau(t) - x_\tau(t)) \cos(\alpha) - F_z - F(t) \tag{3.29}$$

$$J\ddot{\theta}(t) = -K_r u(t)\left(\frac{L_{UC}}{2}\right)\cos(\theta(t)) - K_r\left(\frac{L_{UC}}{2}\right)\cos(\theta(t))\left(\frac{L_{UC}}{2}\right)\sin(\theta(t)) - K_{rot}\theta(t) - K_N u_N(t)(\cos(\alpha)\left(\frac{L_{UC}}{2}\right)\cos(\theta(t)) - \sin(\alpha)\left(\frac{L_{UC}}{2}\right)\sin(\theta(t))) - K_\tau(u_\tau(t) - x_\tau(t))(\sin(\alpha)\left(\frac{L_{UC}}{2}\right)\cos(\theta(t)) + \cos(\alpha)\left(\frac{L_{UC}}{2}\right)\sin(\theta(t))) \quad (3.30)$$

The normal and tangential displacements of the upper cone, $u_N(t)$ and $u_\tau(t)$ are given by Equations (3.31) and (3.32) and can be obtained using the trigonometric relations, assuming small θ:

$$u_N(t) = u(t)\cos(\alpha) - v(t)\sin(\alpha) + \theta(t)\frac{L_{UC}}{2}\cos(\alpha) \quad (3.31)$$

$$u_\tau(t) = u(t)\sin(\alpha) + v(t)\cos(\alpha) + \theta(t)\frac{L_{UC}}{2}\sin(\alpha) \quad (3.32)$$

The linearised stiffness matrix K and force vector F are presented in equations 3.33 and 3.34.

$$K = \begin{bmatrix} K_r + K_N\cos^2(\alpha) + K_\tau\sin^2(\alpha) & (-K_N + K_\tau)\cos(\alpha)\sin(\alpha) & K_r\frac{L}{2} + K_N\frac{L}{2}\cos^2(\alpha) + K_\tau\frac{L}{2}\sin^2(\alpha) \\ (-K_N + K_\tau)\cos(\alpha)\sin(\alpha) & K_N\sin^2(\alpha) + K_\tau\cos^2(\alpha) & (-K_N + K_\tau)\frac{L}{2}\cos(\alpha)\sin(\alpha) \\ K_r\frac{L}{2} + K_N\frac{L}{2}\cos^2(\alpha) + K_\tau\frac{L}{2}\sin^2(\alpha) & (-K_N + K_\tau)\frac{L}{2}\cos(\alpha)\sin(\alpha) & K_{rot} + K_r(\frac{L}{2})^2 + K_N(\frac{L}{2})^2\cos^2(\alpha) + K_\tau(\frac{L}{2})^2\sin^2(\alpha) \end{bmatrix} \quad (3.33)$$

$$F = \begin{bmatrix} -K_\tau x_\tau(t)\sin(\alpha) \\ -F_z - F(t) - K_\tau x_\tau(t)\cos(\alpha) \\ -K_\tau x_\tau(t)\frac{L}{2}\sin(\alpha) \end{bmatrix} \quad (3.34)$$

The EOM of slip are equal to the EOM of stick, with the exception that the tangential spring force $K_\tau(u_\tau - x_\tau)$ is replaced by the friction force F_r of Equation (3.27). To determine if slip or stick occurs, the EOM of the stick situation are first solved and the following condition is then checked:

$$\begin{array}{lllll} \text{Stick}: & \dot{u_\tau}(t) = 0 & \text{and} & F_\tau(t) \leq \mu_s N \\ \text{Slip}: & \dot{u_\tau}(t) \neq 0 & \text{or} & F_\tau(t) \geq \mu_s N \end{array} \quad (3.35)$$

where $F_\tau(t) = K_\tau(u_\tau - x_\tau)$.

The initial value problem is solved numerically using Runge-Kutta formulas of order five and six to obtain the displacements per time step.

3.4. MODEL PREDICTIONS FOR THE SETTLEMENT OF A SLIP-JOINT UNDER SELF-WEIGHT AND IN THE CASE OF DROPPING

3.4.1. INTRODUCTION OF THE CASE STUDY

The installation of a slip-joint onshore is performed by means of dropping the upper cone from a height of 10 cm (van der Tempel and Schipholt, 2003). The dropping of a cone offshore will introduce additional challenges, as the dynamic offshore environment reduces the controllability of the installation. This section compares the results of an installation under self-weight with one that involves dropping (with the latter being less desirable offshore). The degree of settlement achieved under self-weight is obtained for a slip-joint with geometrical properties based on the monopile design of the reference project OC3 (Jonkman and Musial, 2010) (the dimensions are given in Figure 3.5). A constant wall thickness of 60 mm is used.

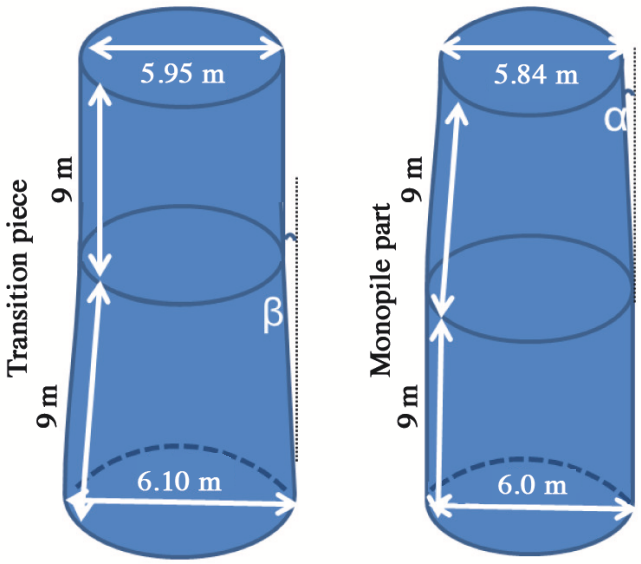

Figure 3.5: Slip-joint dimensions based on the OC3 project.

The cone angles of the upper and lower parts of the slip-joint, the mass of the upper part (the cone plus the straight section), the contact stiffnesses of the lower cone, and the radial and rotational stiffnesses of the upper cone are presented in Table 3.1. The desired overlap length, L_{overlap}, is defined as for grouted connections, i.e. 1.5 D_{MP}, where D_{MP} is the diameter of the monopile. The distance that the upper cone must slip to attain full contact, designated L_{slip}, is dependent on the difference between the cone angles and the length of the desired overlap, as shown in Figure 3.6. From this figure, it can be seen that, for a given set of initial cone angles, full contact can be ensured by an appropriate choice in terms of diameter of the upper cone. This desired slip length is an

estimation and does not take into account the effect of the bending of the cones. The desired slip distance and radius of the upper cone R_{UC} are calculated using Equation (3.36) and (3.37).

$$L_{slip} = L_{overlap}\left(1 - \frac{\sin(\beta)}{\sin(\alpha)}\right) \tag{3.36}$$

$$R_{UC} = R_{MP} - L_{slip}\sin(\alpha) \tag{3.37}$$

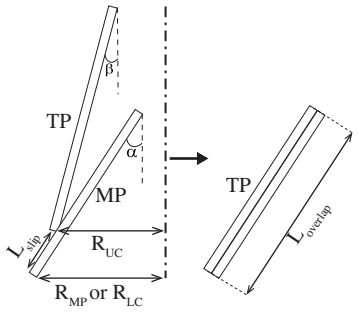

Figure 3.6: Slip distance clarification: on the left the initial situation and on the right the installed situation with the desired overlap obtained.

3.4.2. RESULTS FOR INSTALLATIONS WITH AND WITHOUT AN INITIAL VELOCITY

The tangential displacement u_τ of the upper cone is plotted in Figure 3.7 for a situation in which the upper cone has no velocity or acceleration at the time of first contact. It can be seen that, under the weight only, a small and unsatisfactory slip distance is obtained. The installation method of dropping the upper cone from a height of 10 cm is considered for the case presented in Table 3.1, which can be mimicked by providing the upper cone with an initial velocity of approximately 1.4 m/s at the time of first contact. The slip development including this initial velocity is presented in Figure 3.7 as well. The figure indicates that this 10 cm drop does not result in the desired slip length (settlement of 0.43 m) for the geometry considered: while the settlement obtained due to the initial velocity is two thirds of the desired overlap, it is considered unsatisfactory.

SENSITIVITY OF THE SETTLEMENT TO CONE ANGLES AND FRICTION COEFFICIENT

To investigate the sensitivity of the degree of the settlement to the cone angles and friction coefficient, the five cases listed in Table 3.2 are considered. Case 1 is the same as that described in table 3.1, while cases two and three consider situations in which the two cones are almost vertical, in combination with different dynamic friction coefficients. Cases four and five, consider situations that feature different angles (α and β) with all other parameters being equal to those of case 1. No initial velocity is taken into account for these five cases (installation by self-weight only).

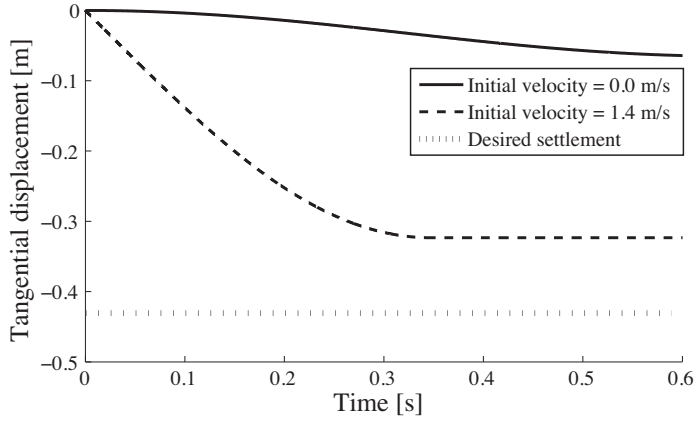

Figure 3.7: Tangential displacement under self-weight with and without initial velocity 1.4 m/s.

Table 3.2: Cases for the sensitivity study.

Case	α / β [°]	R_{UC} [m]	L_{slip} [m]	μ_d [-]
1	1.05 / 1	2.99	0.43	0.3
2	1.05 / 1	2.99	0.43	0.4
3	1.05 / 1	2.99	0.43	0.2
4	2.5 / 1.5	2.68	3.6	0.3
5	2.5 / 2.4	2.96	0.36	0.3

In Figure 3.8 the tangential displacement u_τ of cases 1 to 3 are presented. The figure shows that, for lower friction coefficients, the displacement increases. In Figure 3.9, the tangential displacements for cases 1, 4, and 5 are presented. When comparing the slip distance of case 1 with that of case 4, it can be seen that an increase of the angle α, i.e., a reduced steepness of the lower cone, decreases the slip distance achieved under self-weight. Increasing angle β to be closer to α, i.e. case 5, although implying changes in the stiffnesses of all springs, does not have a significant effect on the slip distance. Comparing case 1 with case 5 it can be concluded that the increase of both cone angles will increase the resistance to slipping. On the basis of these results, it can be concluded that the tangential displacement caused by only the self-weight of the slip-joint is insufficient to obtain the desired contact overlap, even for small angles, small angle differences, and low friction coefficients. For an offshore slip-joint, installation under self-weight is therefore considered to be undesirable and inefficient. Dropping the slip-joint from a height of 10 cm leads to significant tangential displacement, but, as explained previously, is less desirable for the associated risks. As an alternative to these two methods, the vibration-assisted installation of a slip-joint is investigated in the next subsection.

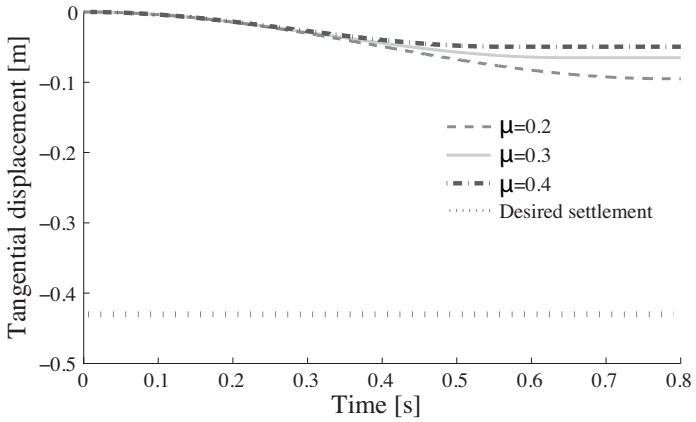

Figure 3.8: Tangential displacement under self-weight for cases 1 to 3 presented in Table 3.2.

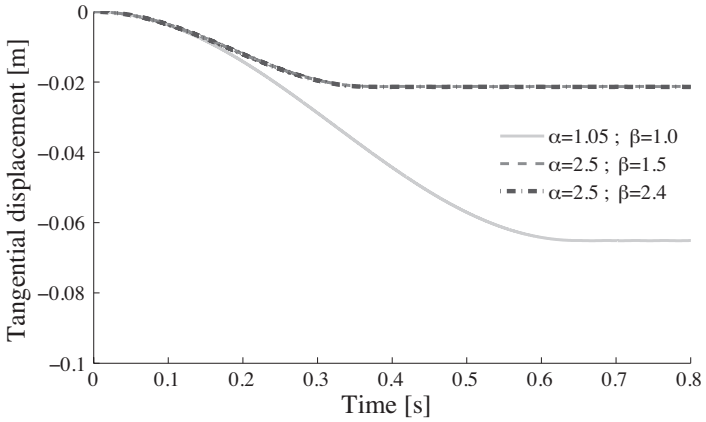

Figure 3.9: Tangential displacement under self-weight for cases 1, 4, and 5 presented in Table 3.2. The desired settlement is not shown here tin order to visualize the effect of the parameter change.

3.5. MODEL RESULTS SIMULATING THE INSTALLATION OF THE SLIP-JOINT ASSISTED BY VIBRATIONS

The installation of a slip-joint under the action of harmonic loads is investigated for case 1 of Table 3.2. A harmonic loading $F(t)$ (Figure 3.1(b)) is applied at the top of the upper cone in the vertical direction. The vertical application of the harmonic force is similar to the vibratory driving used in the offshore industry for pile installation. The frequencies and amplitudes that are used in this analysis are based on the specification of one of the largest vibratory devices used in the industry as of 2013, resulting in a frequency spectrum of 0-20 Hz and force amplitudes of 0 - 500 kN (CAPE Holland, 2015).

In Figure 3.10, the tangential displacement achieved under harmonic loading with an amplitude of 300 kN is plotted over time and for various forcing frequencies: Low frequencies show a rough stick-slip behaviour, while higher frequencies smoothen the stick-slip behaviour. The figure also indicates that, after a certain time, a stable stick position is reached for all of the frequencies used.

In Figure 3.11, the final stick position achieved after after 90 seconds of harmonic loading is plotted as a function of the forcing frequency and amplitude. It can be concluded that the desired tangential displacement can be achieved with harmonic loading using various combinations of amplitudes and forcing frequencies. This indicates that the controlled installation of a slip-joint is possible by means of the application of vibration during the installation of the upper cone.

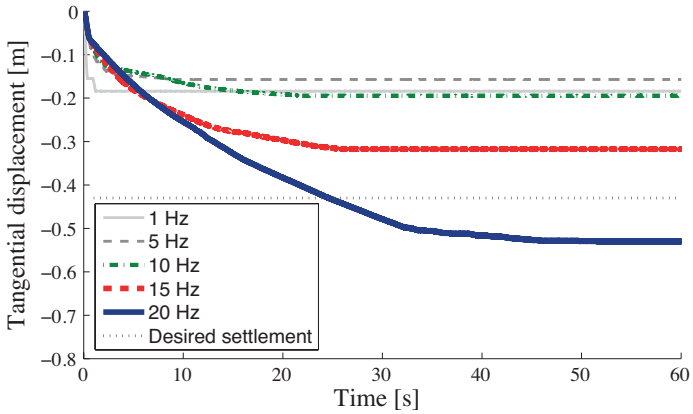

Figure 3.10: Tangential displacement under harmonic loading with an amplitude of 300kN and various frequencies of oscillation.

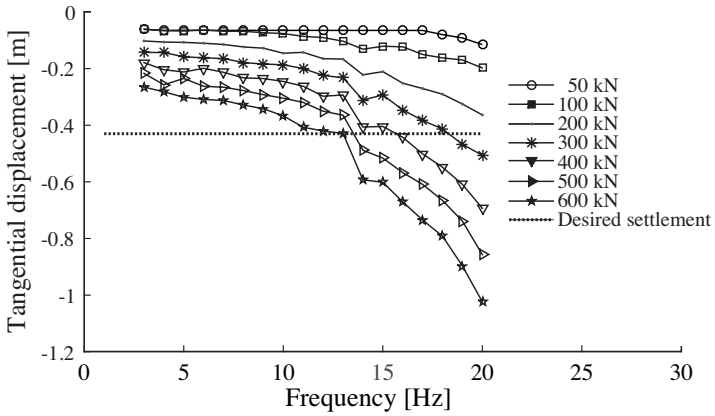

Figure 3.11: Tangential displacement after 90 seconds harmonic loading as a function of the frequencies and the amplitudes applied.

3.6. CONCLUSIONS

From the dynamic axisymmetric installation analysis, it is concluded that the tangential displacement caused by the self-weight is insufficient to achieve the desired contact overlap. With an initial velocity, however, significant displacements can be achieved, but dropping the slip-joint from a certain height is considered insufficiently controllable due to the challenging nature of the offshore environment. The predictions of the model indicate that the desired settlement can be achieved using harmonic loading, using various combinations of amplitudes and frequencies. These results are valid for an axisymmetric installation and indicate that the controlled installation of a slip-joint is possible. Though promising, the model is fairly simple and is not able to describe the vibrational shapes of a combined slip-joint system. Based on these promising results, a test campaign was set up in order to investigate the vibration-assisted installation procedure in more detail. This campaign is the topic of the next chapter.

4

EXPERIMENTAL CAMPAIGN FOR STUDYING A SLIP-JOINT CONNECTION

4.1. INTRODUCTION

Although, the slip-joint in full-scale is not yet applied offshore, an envisaged installation is considered that keeps the number of installation steps and the duration of an installation process to a minimum. Therefore, it is reasonable to consider that, first the upper cone slides over the lower one using the dead weight of the former. Next, a shaker is placed on top of the upper cone, and vibration assistance can be used to settle the upper cone to its final position, thus providing the required stability and load transfer. This procedure is similar to the currently employed procedure of installing the transition piece using a grouted connection except that the grouting process is replaced by vibration-assisted settlement induced by the shaker. The lumped model considered in Chapter 3 shows that, in theory, vibrations are effective during the installation of a slip-joint. The model's results indicate that the degree of settlement achieved is dependent on the amplitude and frequency of the vibration applied.

In this chapter, the results of a three-part experimental campaign intended to investigate and prove the effectiveness of the vibration-induced settlement in the installation and dismount of a slip-joint are presented. The chapter is divided into three parts, of which the first focuses on the experimental investigation of vibration-induced settlement by applying vibrations to scaled specimens of the slip-joint. This is done by mimicking the envisaged installation procedure at full scale with scaled specimens of the slip joint. The design of the setup, the measurement programme, the test cases for which data are collected, and the result obtained of the experimental investigation of the application of vibrations to scaled specimens of the slip-joint are presented in Section 4.2. The second part of this chapter presents an experimental modal analysis that serves to investigate the behaviour of a joint at certain resonance frequencies. The measurement method, the design and the results of the experimental modal analysis are presented in Section 4.3. In the third part of this chapter the measurements made of the dimensions of one

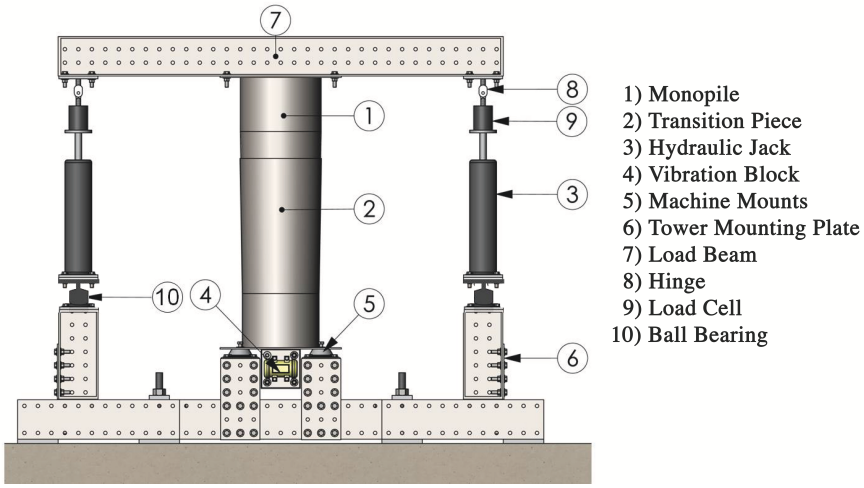

Figure 4.1: The experimental setup.

set of scaled cones are presented. By measuring the dimensions of one of the slip-joint specimens, the status of the cones prior to installation can be determined. In Section 4.4 the setup of the measurements, the data processing and the results of the dimensional analysis are presented. Finally, conclusions on the obtained result of the experiments are presented in Section 4.5.

4.2. EXPERIMENTS ON THE VIBRATION-INDUCED SETTLEMENT OF A SLIP JOINT

4.2.1. DESCRIPTION OF THE SETUP OF THE EXPERIMENTS

To simulate installations under both self-weight and dynamic loading, a setup is designed that allows for axial loading, movement in the direction of shaking, relative motion between the cones, and a slight inclination between the axes of the cones. In Figures 4.1 and 4.2, the experimental setup and a photograph of the built setup, respectively, are shown. A more detailed description of the setup is provided in the following sub-sections.

DIMENSIONS OF THE CONES IN THE SCALED EXPERIMENTS

The dimensions of the slip-joint are based on the monopile (MP) design of the OC3 project (Jonkman and Musial, 2010). The OC3 project uses a monopile of 6 m in diameter. with a wall thickness of 60 mm. The desired overlap length for the slip-joint is defined as being the same as for classic grouted connections, i.e. 1.5 D_{MP}, where D_{MP} is the diameter of the monopile. The cone angle of the transition piece (TP), β, is chosen smaller than the angle of the conical part of the MP, α. This is done to ensure full contact for the desired overlap. The experiments are performed on 1:10-scaled specimens of the slip-joint. In Table 4.1 the dimensions of the scaled slip-joint are given.

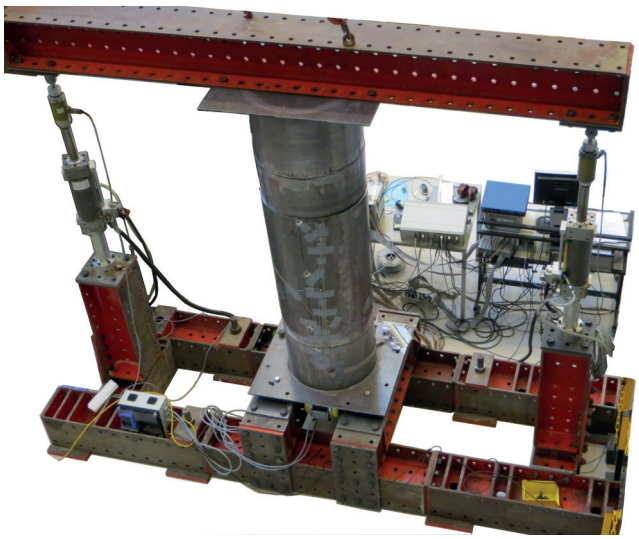

Figure 4.2: The experimental setup as built in the Stevinlab in Delft.

Table 4.1: Design parameters of the scaled slip-joint case study.

	Lower cone (MP)	Upper cone (TP)	Unit
Cone angle	α=1.05	β=1.0	°
Top outer diameter	0.584	0.594	m
Bottom outer diameter	0.600	0.610	m
Wall thickness	6	6	mm
Cone length	1.0	1.0	m
Total length	1.4	1.4	m
Total mass	0.15	0.15	tons
Steel type	S355	S355	

SCALING INFLUENCES

Similitude in terms of geometry and material are kept when a scaling of 1:10, equal to a scaling factor S_l=10 is applied. The dimensions of the wall thickness h, the diameter D and the length L are reduced proportionally by a factor S_l.

The axial force, F_{ax}, applied to the upper cone is scaled such that the axial stress, σ_{ax}, in the scaled setup is similar to the full-scale stress. Equation (4.1) indicates axial stress scales with a factor S_l^2, as it is related to the area of the cross section.

$$\frac{F_{axfs}}{F_{axms}} = \frac{\sigma_{ax} A_{csfs}}{\sigma_{ax} A_{csms}} = S_l^2 \tag{4.1}$$

Where A_{cs} is the area of the cross section and the subscript 'ms' stands for model-scale and 'fs' stands for full-scale. Equation (4.2) shows that the axial force F_g as a result of the mass m of the cone scales with a factor S_l^3, as it is related to volume.

$$\frac{F_{g_{fs}}}{F_{g_{ms}}} = \frac{m_{fs} g}{m_{ms} g} = S_l^3 \tag{4.2}$$

In order to keep the same axial stress levels, additional force is required in order to mimic the downward force and the stress level that occur as a result of the self-weight of a slip-joint. In equation (4.3) to (4.6) the required additional force is obtained:

$$F_{g_{fs}} = S_l^2 F_{axms} \tag{4.3}$$

$$F_{g_{fs}} = S_l^2 \left(F_{g_{ms}} + F_{add}\right) \tag{4.4}$$

$$F_{g_{fs}} = S_l^2 \left(\frac{F_{g_{fs}}}{S_l^3} + F_{add}\right) \tag{4.5}$$

$$F_{add} = \left(\frac{1}{S_l^2} - \frac{1}{S_l^3}\right) F_{g_{fs}} \tag{4.6}$$

The additional axial force required to reproduce the scaled stress levels is approximately 10 kN and is applied using two hydraulic jacks. This additional axial load creates similar stress levels in the MP as would be found as a result of the weight of the full-scale TP of 14 m in length.

ORIENTATION OF THE TEST PIECES

The cones representing the MP and the TP are placed upside down for reasons of safety and practicality. By attaching the shaker to the TP (the lower cone in Figure 4.1) the shaker is located close to the floor, thereby allowing for a safer execution of the experiments (as opposed to the shaker being installed at the top of the setup). Within this arrangement, the vibrations are applied to the transition piece, whereas the static load is applied, at the top of the setup to the cone that represents the MP, as depicted in Figure 4.3. This allows for decoupling of the dynamic and static loads, which reduces the impact of the vibrations on the static load actuators.

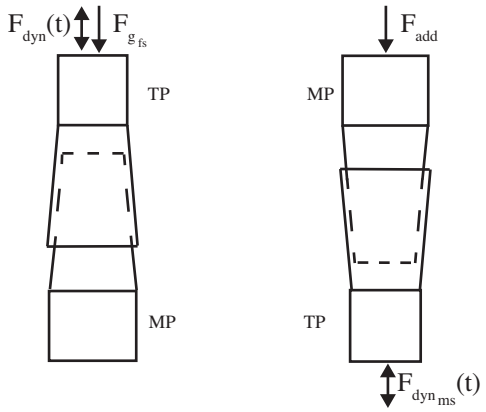

Figure 4.3: On the left: normal full-scale installation and on the right: the installation using the experimental setup.

SUPPORTING SPACE FRAME AND BEARINGS

The H-profile columns are connected by mounting plates, thread rods, and bolts. To allow a slight tilt of the MP, hinges are installed in-between the vertical columns and the load beam, as indicated in Figure 4.1. The columns are only mounted to the bottom frame via mounting plates on the outer sides of the column, thus allowing a slight bending movement if needed. Additionally, ball bearings at the top of the columns allow the cones to self-align.

The machine mounts allow the TP to vibrate while it is supported. These mounts are rubber bearings made by the manufacturer Euro-bearings, and are typically used to mount vibratory machines (Euro-bearings LTD, 2013). The conical shape of the mount provides equal stiffness in lateral directions and allows a vertical movement as well. The stiffness in axial direction of a single machine mount is k_{ax} = 4.2 kN/mm; in lateral directions, the stiffness is k_{lat} = 4.8 kN/mm.

ACTUATORS FOR THE DYNAMIC AND STATIC LOADS

To achieve vibration-induced settlement, a harmonic excitation is applied, in either the vertical or horizontal direction, at the 'top' of the TP. For the selection of a shaker, the operational specifications of currently used industry shakers were reviewed. The specifications of a shaker that is used for the vibratory driving of large monopiles (CAPE Holland, 2015) are used as a reference. This shaker (i.e. a vibratory driver), the CAPE model CV-230 (in 2013 still called the APE model 600), operates in the frequency band of 0-20 Hz. This vibratory device typically applies force in the vertical direction.

To determine the frequencies of the excitations to be used in the experiment, the effect of scaling on the natural frequencies of the TP is investigated. This is done using a finite element model of the TP implemented in the engineering simulation software package Ansys. In this model, the TP is fixed at the lower boundary and free at the upper boundary. In Figures 4.4 and 4.5, the mode shapes and corresponding frequencies of the

full-scale and a 1:10-scale TP, respectively, are shown. These figures show that the frequencies scale approximately inversely proportional to the scaling factor. Therefore, the shaker used in the experiments should ideally operate in the frequency band of 0-200 Hz.

The vibratory load is generated by either two motors with eccentric masses or an electrodynamic shaker. Both options are investigated in this experiment. The eccentric mass motors use the same principle as the commercial shakers used in in the offshore industry; a centrifugal force is excited by a spinning eccentric weight that is connected to a motor by means of a shaft. The resulting centrifugal force is given by Equation (4.7):

$$\vec{F}_{centrifugal} = m_{eccentric} r \omega^2 \tag{4.7}$$

In which r is the distance from the centre of the eccentric mass to the shaft centre. The eccentric force $\vec{F}_{centrifugal}$ points outwards from the centre and rotates with the rotational velocity. The magnitude of the eccentric force is a function of the rotational/vibrational frequency ω. The Wacker Neuson AR 53 (12/250) (Wacker Neuson, 2015) eccentric motor is chosen, in combination with a frequency controller from Invertek, the Optidrive P2 ODP-2 (Invertek drives, 2015), on the basis of the required frequency range and magnitude of the force required in order to to mimic (on scale) the CAPE model CV-230. Two of these motors rotating in opposite directions with the same angular velocity apply a harmonic force in either the vertical or horizontal direction. In this experiment, both directions of forcing are investigated. The two motors are mounted at the closed end of the TP; the locations of the motors are identical to those used in real offshore scenarios.

The electrodynamic shaker chosen is a Bruel & Kjaer type 4812, in combination with a type 2707 power amplifier (Bruel & Kjaer, 1971). This shaker generates a harmonic motion and is connected to the transition piece with a stiff rod. Four locations, of two different heights and two different circumferential positions, are used to introduce vibration using the shaker. Two locations lie close to the bottom, with an offset of 90 degrees of each other. The other two are located in the middle of the cone and, again have a 90-degree offset. These locations are used to investigate the influence of the point of application of the vibratory force on the settlement behaviour of the cone. With this shaker, the vibratory force always acts in the horizontal plane. In Figure 4.6, a picture including the shaker, the load cell, and the rod is shown.

The advantage of the electric shaker compared to the eccentric motors is that it allows for amplitude control for each frequency; therefore, the shaker can be used to study the effect of the amplitude of the vibratory force on settlement at each frequency of interest. The amplitude that the electrodynamic shaker can generate is relatively small when compared to the eccentric motors (approximately 250 times). Additionally, the shaker is used to investigate whether there are additional effective frequencies beyond the operational limits of the eccentric motors. A downside of the electric shaker system is that the frequency of vibration could not be logged by the data acquisition system. The frequency was therefore logged on paper, and the frequency is thus omitted in some of the presented results.

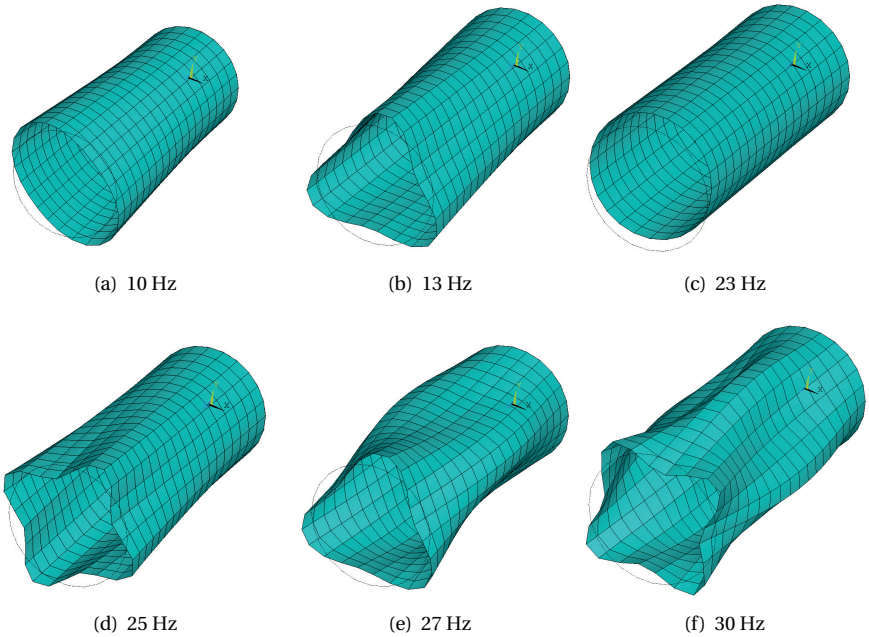

(a) 10 Hz (b) 13 Hz (c) 23 Hz

(d) 25 Hz (e) 27 Hz (f) 30 Hz

Figure 4.4: Mode shapes and the corresponding natural frequencies of the full-scale transition piece.

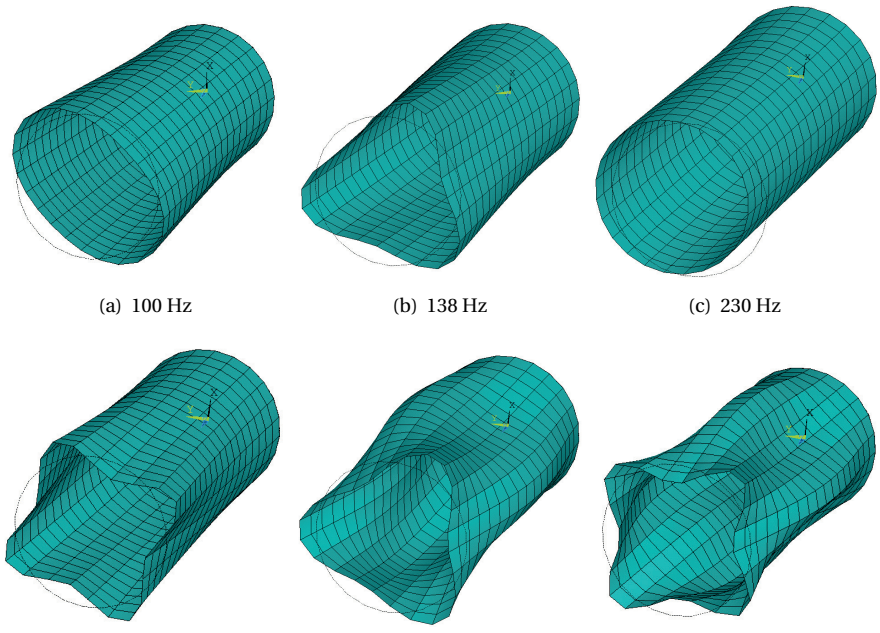

(a) 100 Hz (b) 138 Hz (c) 230 Hz

(d) 251 Hz (e) 276 Hz (f) 309 Hz

Figure 4.5: Mode shapes and the corresponding natural frequencies of the 1:10-scale transition piece.

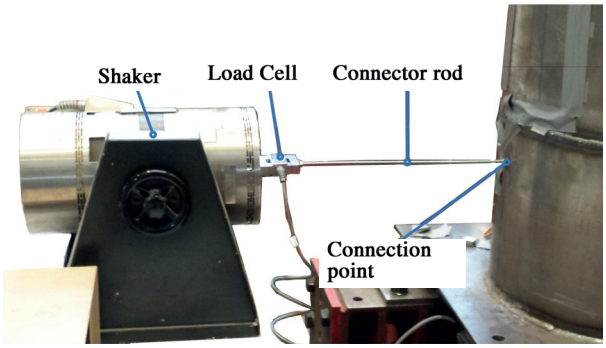

Figure 4.6: Electric shaker connection to one of the four connection points.

4.2.2. DESCRIPTION OF THE TEST CASES

The experimental setup is used to perform installation and dismount tests. The following main installation sequence is performed:

1. Lower the MP onto the TP under self-weight.
2. Simulate the full-scale self-weight.
3. Start of the application of vibration.
4. Increase of the frequency in steps or by a constant increment.

During the installation process vibration is applied and its frequency is increased in either small steps of maximum 5 Hz or by a constant increment. These procedures makes it possible to investigate which excitation frequencies are effective in terms of settlement, to understand the settlement mechanism, and to develop insight into the influence of the increment of the excitation frequency and the installation procedure. In the experiments that feature a step-wise increment of the frequency, the frequency is kept constant at the instance that settlement occurs. The frequency is increased further only after the settlement has stopped/stabilized. In the experiments that feature a ramping up of the frequency, various rates of frequency increment are used.

A reverse installation procedure is used for the dismount of the joint. The vibration is only applied after the application of a pulling force. By changing the frequency of the vibration thereafter, the frequencies that provide the most efficient dismount of the cones can be identified. As a rule, the following steps are used in the dismount experiments:

1. Initiate a pulling force that is similar in magnitude as step 2 of the installation.
2. Start the application of vibration.
3. Step-wise or constant increment of frequency until the upper cone dismounts.

To check the reproducibility of the measurement results, two identical sets of cones are used in the experiments. The use of two sets, additionally, allows for different sensor configurations. In total 84 test were performed on two sets of cones that focussed on either the installation, dismount or investigating the dynamic response of the cones. In Tables 4.2 and 4.3, a summary of the different batches of these experiments is provided. A more extensive description of the experiments and their results can be found in Appendix B.

Table 4.2: Overview of the experimental batches.

Nr.	Type of test	Set	Vibratory device	Frequency increase	Axial force[kN]	Result
1	Install	1	Eccentric motor	Step wise increase	10	13.4 mm
2-6	Dismount attempts	1	Eccentric motor	Various Linear increments	-6, -10, -15, -20	no dismount
7	Dismount	1	Eccentric motor	Step wise increase up to 85 Hz	-40	Successful dismount
8	Install	1	Ecc. Motor	Step wise increase up to 115 Hz	10	12 mm
9	Max. Axial force	1	none	none	10 to 60	No settlement
10	Dismount	1	Ecc. Motor	Step wise increase up to 128 Hz	-30	Successful dismount
11	Install	1	Ecc. Motor	Linear increase from 0-128Hz in 13 sec	10	11 mm
12	Install	2	Ecc. Motor	Slow step wise increase to 200 Hz	10	14 mm
13	Dismount	2	Ecc. Motor	Slow step wise increase to 128 Hz	-30	Successful dismount
14	Install	2	Ecc. Motor	Slow step wise increase to 200 Hz	10	11.5 mm
15	Dismount	2	Ecc. Motor	Slow step wise increase to 127.5 Hz	-30	Successful dismount
16	Install	2	Ecc. Motor	Linear increment 0-130Hz in 15s	10	10 mm
17	Dismount	2	Ecc. Motor	Linear increment 0 to 126 Hz in 13 s	-30	Successful dismount
18	Install	2	Ecc. Motor	Linear increment 0-126Hz in 13s	10	13 mm
19	Dismount	2	Ecc. Motor	Linear increment 0 to 124 Hz in 13 s	-30	at 125 Hz it dismount
20	Install	2	Ecc. Motor	Linear increment 0-126Hz in 13s	10	9.8 mm
21	Dismount	2	Ecc. Motor	Linear increment 0 to 127 in 13	0 to -30	at -30 kN it dismounts
22	Install	2	Ecc. Motor	Slow step wise increase to 200 Hz	10	11.4 mm
23	Dismount	2	Ecc. Motor	Linear increment 0 to 125 Hz	0 to -30 to -35	at -35 kN it dismounts
24	Install	2	Ecc. Motor	Slow step wise increase to 200 Hz	10	10.7 mm
25	Dismount	2	Ecc. Motor	Linear increment 0 to 125 in 13 s	0 to -30	Successful dismount
26	Install	2	Ecc. Motor	Linear increment 0-125Hz in 26s	10	12.5 mm
27	Dismount	2	Ecc. Motor	Linear increment 0 to 125 in 60 s	-20	Successful dismount
28	Install	2	Ecc. Motor	Linear increment 0 to 125 in 60 s	10	11.3 mm
29	Dismount	2	Ecc. Motor	Linear increment 0 to 120 in 60 s	-20	comes loose at 110 Hz
30-1 to 30-10	Impact/install	2	Hammer /Ecc. Motor	Between settlements hammer impact tests.		11.2 mm + Freq. response
31	Dismount	2	Ecc. Motor	Linear increment 0 to 120 in 60 s	-20	comes loose at 110 Hz
32	Install	2	Ecc. Motor	ramp up to 118 hz then in steps to 130		10 mm
33-1 - 33-2	Dismount	2	Ecc. Motor	Linear increment 0 to 118 to 128 to 116 Hz	-18	Dismount at 120 Hz
34-1 to 34-15	Install	2	Ecc. Motor	Step wise increase of the frequency	10	Separate files of settlement events
35	Dismount	2	Ecc. Motor	Linear increment 0 to 118	-20	Dismount at 110HZ
36-1 to 36-15	Impact/install	2	Hammer /Ecc. Motor	Between settlements hammer impact tests.	0 to 10	7.55 mm + Freq. response
37-39	Dismount	2	Ecc. Motor	in several attempts it comes loose	-20, 24, 36	Successful dismount
40-41	Install	2	Ecc. Motor	ramp up to 123Hz	10	12.7mm
42	dismount	2	Ecc. Motor	Linear increment 0 to 118	from +10 to -30	Dismount at -20kN and at 118Hz

Table 4.3: Overview of the experimental batches.

Nr.	Type of test	Set	Vibratory device	Frequency increase	Axial force[kN]	Result
43-44	Install	2	E.D. shaker	Sweep 20-400Hz in 180 s	0, 10, 18	3 mm
45	Install	2	E.D. shaker	Sweep 20-800Hz in 600 s	20	3.9 mm
46-49	Install	2	E.D. shaker	Sweep 20-250Hz in 230 s	20	no settlement
49-51	Install	2	E.D. shaker	Sweep 20-250Hz in 230 s	24	2.2 mm
52	Dismount	2	E.D. shaker	sweeping between 230 and 250 Hz	-27	Releases at 249.5 Hz
53	Install	2	E.D. shaker	249Hz, in step the amp is increased	28	10 mm
54	Dismount	2	E.D. shaker	249Hz	-28 to -30	Successful dismount
55	Install	2	E.D. shaker	Sweep 20-300Hz in 280 s; 249.5 Hz	32	1.5 mm
56	Install	2	E.D. shaker	249Hz, in step the amp is increased	28	6 mm
57	Dismount	1	E.D. shaker	Sweep from 20-300 Hz with 1Hz/s	24 to -34	Dismounts at 269 Hz.
58	Install	1	E.D. shaker	Step-wise from 20 to 400 Hz	10	8.5 mm
59	Dismount	1	E.D. shaker	Step-wise from 0 to 119 Hz	-30	Dismounts at 119 Hz
60	Install	1	E.D. shaker	Step-wise from 119 Hz to 200Hz	10	7.1 mm
61	Install	1	E.D. shaker	Sweep from 20-320 Hz with 1Hz/s	10	at 240Hz 1 μm
62	Dismount	1	E.D. shaker	Shaking with 119hz	-30	Dismounts at 119 Hz
63	Install	1	E.D. shaker	Step-wise from 0 to 300 Hz	10	4.7 mm
64	Dismount	1	E.D. shaker	Shaking with 119hz	-24	Dismounts at 119 Hz
65	Install	1	E.D. shaker	Shaking with 120hz	10	7 mm
66	Frequency response	1	E.D. shaker	Sweep from 20-300 Hz with 1Hz/s		Frequency response
67	Dismount	1	E.D. shaker	Shaking with 120hz	-24	Dismounts at 120 Hz
68	Install	1	E.D. shaker	Step-wise from 0 to 300 Hz	10	3 mm
69	Dismount	1	E.D. shaker	Shaking with 120hz	-20	Dismounts at 120 Hz
70	Install	1	E.D. shaker	Shaking with 120hz	10	4.6 mm
71	Frequency response	1	E.D. shaker	Sweep from 20-300 Hz with 1Hz/s		Frequency response
72	Dismount	1	E.D. shaker	Shaking with 120hz	-30	Dismounts at 120 Hz
73	Install	1	E.D. shaker	Shaking with various frequencies	10	10 mm
74	Dismount	1	E.D. shaker	Shaking with 120hz	-20 to -40	Dismounts at 120 Hz
75	Install	1	E.D. shaker	Shaking with 260 hz and then to 120 Hz	10	6 mm
76	Dismount	1	Ecc. Motor	Linear increment 0 to 118	-20 to -30	Dismounts at 121 Hz
77	Install	1	only axial forces	from 0 to 10 kN in 20 s	10	Shows stick slip behaviour
78	Install	1	Ecc. Motor	Step-wise from 0-200Hz	10	10 mm
79	Dismount	1	Ecc. Motor	Linear increment 0 to 118	-24	Dismounts at 120 Hz
80-1-80-5	Install	1	Ecc. Motor	Step-wise (multiple files)	10	10 mm
81	Dismount	1	Ecc. Motor	Linear increment 0 to 118	-22	Dismounts at 120 Hz
82	Install	1	Ecc. Motor	Slow ramp up to 120Hz in 60s	10.	7.9 mm
83	Install	1	Ecc. Motor	Linear increment 0 to 118	-22	Dismounts at 120 Hz
84	Install	1	Ecc. Motor	Slow ramp up to 120Hz in 200s	10	8.5 mm

4.2.3. MEASUREMENT PROGRAMME

Figure 4.7 shows a drawing of the two cones in which the placement of the sensors is indicated. Four displacement sensors, which measure distances up to 20 cm, are equidistantly placed around the circumference. These are used to measure the displacement that occurs during the installation and dismount experiments.

Strains and accelerations are measured at various heights and circumferential positions. The strains are measured at three heights, namely H10, H35, and H70. The height H is referenced to the open end of the TP, i.e. H10 means 10 cm from the open end of the TP. A ring of eight equally spaced strain gauges is placed at each of these heights. Strains are measured in the circumferential direction using strain gauges of 8 cm in length. The strain in this direction indicates the increase in the diameter of the cones averaged over the length of the gauge. The strain measurements are used to check for local and global deformations and the stresses that occur due to the deformations inflicted on the cones during installation.

Two rings of 16 accelerometers are equidistantly spaced around the circumference, at heights H5 and H50. The number of sensors is based on the mode shapes of the FE model, which are depicted in Figure 4.5. To be able to capture the shape of the modes (up to fourth circumferential mode and the first longitudinal mode), at least 16 sensors at two different heights are required. The results of the accelerometers are used to track the differences in the responses of a single cone and that of the combined system of the two cones.

Triaxial accelerometers of the type Analog ADXL 326 (Analog Devices, 2013) are used. The bandwidth of these accelerometers is 1600 Hz in the local x and y directions and 500 Hz in the z direction. The maximum acceleration that the sensor can measure is 16 g. The data acquisition equipment is shown in Figure 4.8. The output of the strain gauges is amplified using Wheatstone circuits and is fed to data acquisition boxes (DAQs) that are connected to the computer. The accelerometers are supplied with 3.33 V, and their output is fed to the DAQ's. The jack controller is used to control the axial load that is provided by the hydraulic jacks.

4.2.4. RESULTS OF THE VIBRATION-INDUCED SETTLEMENT EXPERIMENTS

In the following subsections a part of the results obtained during the experiments is given. The results of selected experiments which further substantiate the overall conclusions of the experiments describes here are given in Appendix B.

DISPLACEMENTS INDUCED BY ECCENTRIC MOTORS FOR THE STEP-WISE INCREASE IN FREQUENCY OF VIBRATION

Figure 4.9 presents both the settlement and the axial load applied to simulate the self-weight of the upper cone. The plots show that the increment of the applied force plays a role in the observed settlement behaviour of the joint to axial loads. When a slow increase in the axial force is applied, a stick-slip settlement behaviour is immediately observed. The measured displacements varied between individual tests, and it is noted

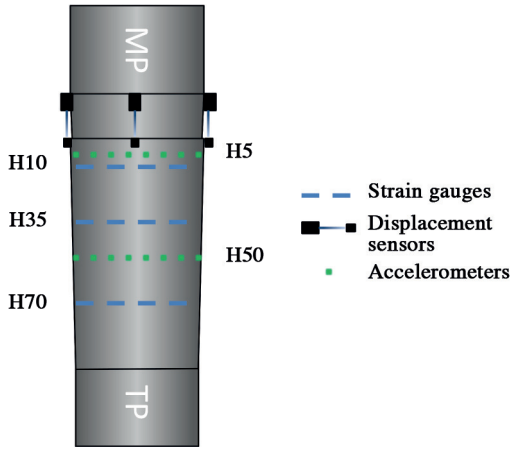

Figure 4.7: Illustration of the sensor placement on the cones during the experiments.

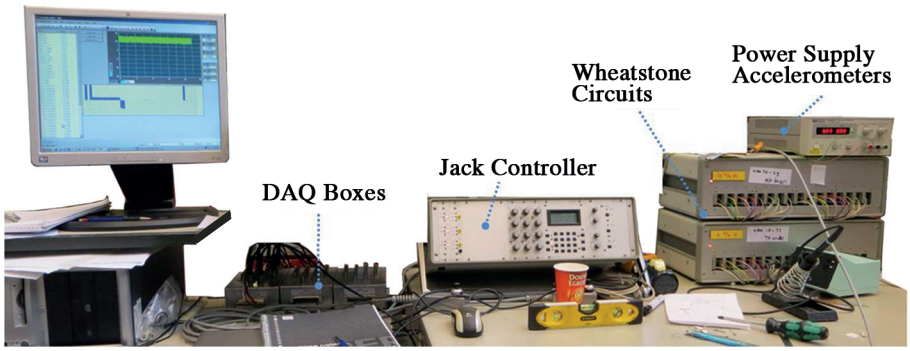

Figure 4.8: The setup of the data acquisition system at the Stevinlab.

that the observed settlement decreases with an increase in the number of repetitive tests performed on the same set of cones. Settlements of between 8 mm and 14 mm were observed after the application of the axial load.

In Figure 4.10(a), the settlement between the cones and the excitation frequency as a function of time are shown for a step-wise increase in frequency. It is observed that settlement occurs only at a number of specific frequencies. At each of these frequencies, the settlement first increases and then stabilizes to a certain level. This stabilization shows that a controlled installation under vibratory loading is possible. This settlement behaviour was observed in all of the installation tests. Small differences were found in the frequencies that were identified to be effective for each set of cones. A possible explanation for these differences is that these originate from the manufacturing tolerances. Changing the direction of the vibration of the eccentric motor from vertical to horizontal did not lead to changes in the settlement behaviour or the observed effective frequencies. This observation indicates that movement of the cones is mainly achieved as a result of structural vibrations perpendicular to the movement. The combination of the self-weight and shaking at certain (resonance) frequencies in one of the two directions is sufficient for settlement movements.

Figure 4.10(b) shows the static axial force applied by the hydraulic jacks and the amplitude of the vibratory force over time for the same test used to plot Figure 4.10(a). The two figures indicate that, although the amplitude of the dynamic force keeps increasing, settlement only occurs at several instances. After the last settlement event achieved at frequency of vibration of 110 Hz (at approximately 380 s), the amplitude of vibration tripled at 200 Hz. The absence of any settlements after a frequency of 110 Hz is applied demonstrates that the settlement is not proportional or even correlated with the amplitude of the applied force.

These results demonstrate that the application of a greater force does not automatically lead to larger settlement; rather, they illustrate the relevance of the frequency of vibration. These effective frequencies are presumed to be close to the resonance frequencies of the combined system. This observation is partly in accordance with the observation of Godfrey (1967) that vibrations reduce the friction coefficient for metal-to-metal contacts. In the experiments presented in this chapter, this reduction of friction coefficient cannot be reproduced directly. However, at certain frequencies this effective reduction of the friction coefficient can indirectly observed through the settlement that occurs.

SETTLEMENTS INDUCED BY ECCENTRIC MOTORS FOR A UNIFORM INCREASE IN EXCITATION FREQUENCY.

In Figure 4.11(a) the results of an installation test in which a vibration with an increment of increase in frequency of 2 Hz/s are presented. It is observed that the settlement keeps on developing after the target frequency of 120 Hz was reached and that the settlement eventually reaches an equilibrium. Furthermore, the figure shows that no additional settlement could be obtained by changing the frequency after this equilibrium was reached.

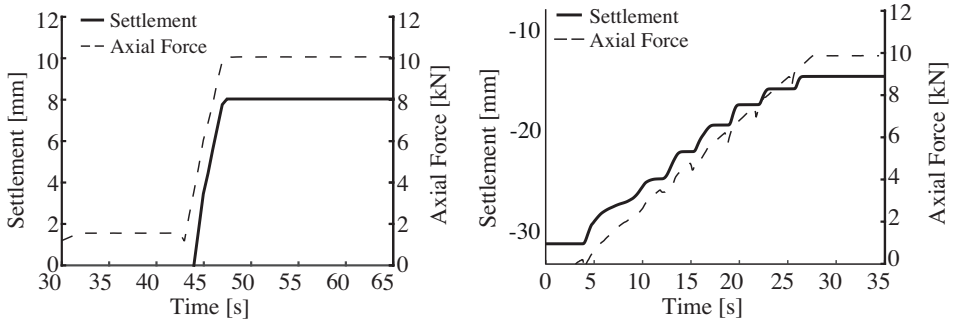

(a) With a large increment of the self-weight, Test 20.

(b) With a small increment of the self-weight, Test 77.

Figure 4.9: Settlement achieved as a result of the simulated self-weight.

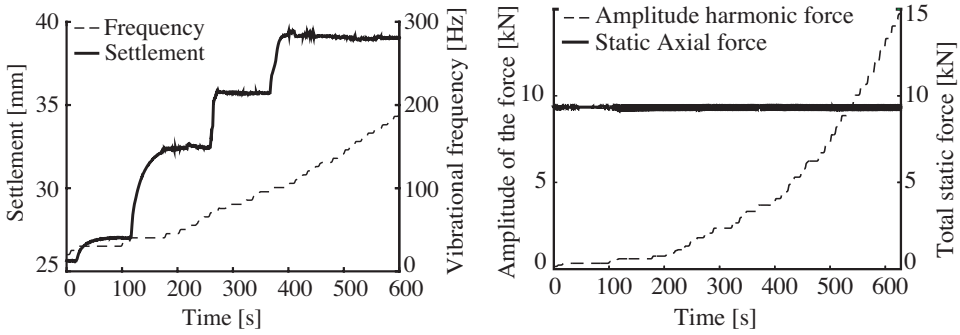

(a) The settlement of the upper cone and the vibrational frequency, Test 1.

(b) The applied dynamic and static force, Test 1

Figure 4.10: The settlement of the upper cone as a function of the vibrational frequency and the applied forces over time.

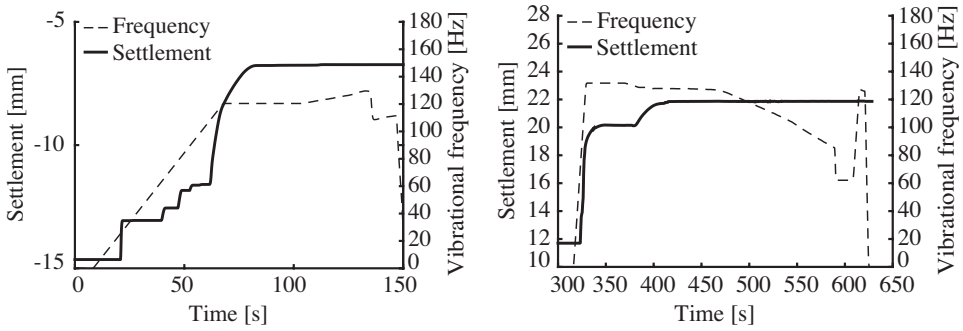

(a) Increment in frequency of 2 Hz/s, Test 82.

(b) Increment in frequency of 10 Hz/s, Test 16.

Figure 4.11: The achieved settlement and vibrational frequency over time for different increments of increase in frequency of the vibration.

Figure 4.11(b), in contrast, shows the results for an increment of the increase in frequency of 10 Hz/s. This increment was varied to investigate the time dependence of the settlement process. The figure shows that the frequency of the vibration (deliberately) slightly overshoots the target over a period of 13 s between 310 and 323 s. Hereafter, the frequency was lowered, and additional settlement was observed.

When comparing the two figures, it can be concluded that the final position is only reached when the settlement is given sufficient time to develop. Therefore, if the effective frequencies are passed rapidly, a smaller settlement than that which could be achieved is reached. Note that the two figures are obtained from two different sets of cones and that only the relative settlements are of importance. The recorded absolute settlement levels differ from test to test, as nullings of the sensors were performed at different positions from the start of the individual tests. The resulting behaviour of the settlement demonstrates that both methods of increasing frequency (a step-wise increase and a 'slow' but constant increase) are effective for the purpose of installation.

STRAINS INDUCED BY THE ECCENTRIC MOTORS

Figure 4.12 provides an illustration of the transition piece in which measurement positions of the strains gauges are indicated for convenience and interpretation of the results. The position of a strain gauge is denoted with a string location (S) and a height location (H). The circumference is divided by 16 equally spaced vertical lines/strings. A string connects the coordinates of one circumferential position to the height/axial positions on the pile. The height position is measured with reference to the open end of the TP. The strain gauges are placed at three heights, and eight gauges are placed at the even numbered strings at each of these heights. Strain gauge H10S2 refers to the strain gauge results at a location 10 cm from the open end of the TP and at the circumferential position of string 2.

Figure 4.13 gives the strains at the ring of gauges at height H10 for an installation test similar to that of Figure 4.10(a). This figure indicates that parts of the circumference are expanding, while other parts are compressed. A uniform and symmetric contact between two perfectly cylindrical rings would result in a uniform extension/strain value around the circumference. Considering the measured strain, one can conclude that the contact along the circumference is non-uniform. The presence of the weld contributed to the non-uniform behaviour, as the material around the weld is less flexible.

The observed strain levels are well within the elastic region which lies at approximately 1600 microstrains for S355 steel. The resulting strain levels show that no yielding of the material occurred during the vibration-assisted installation of the slip-joint.

ACCELERATION RESULTS USING THE ECCENTRIC MOTORS

Figures 4.14 and 4.15 present the response spectrum of the hammer impacts delivered after various settlement levels were reached. Each impact test is performed without active vibrations. A sensor is denoted with a letter for height (A or B), the direction of the measured response (R or T), and the circumferential location at the TP (1 to 16); sensors denoted with A and B belong to the ring H5 and H50. The R and T stand for the response direction in the radial and tangential directions, respectively, and the number 001-016 belongs to the string number that is indicated on the cones. Figure 4.12 shows the even string numbers located at the cone.

When comparing the measurement of the sensors taken at three settlement levels, multiple observations can be made; The first is that there are differences in response between all of the displayed situations. This demonstrates that the dynamic properties of the system change with increasing settlement depth. Second, the system shows unchanged frequency components at approximately 25 Hz between the measured responses. It can be observed that the response peak around 120 Hz is missing for the situation where no settlement has occurred, as represented by the blue line. A final observation is that the peak around 120 Hz slightly shifts to a higher frequency for increasing settlement. This indicates that the system stiffness increases with increasing settlement.

Unfortunately, the mode shapes could not be obtained from these acceleration measurements. This was a result of a poor quality of the synchronization of the channels of

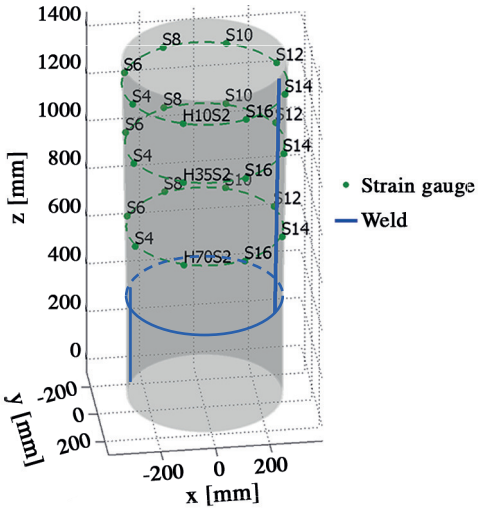

Figure 4.12: Placement of the strain gauges on the transition piece.

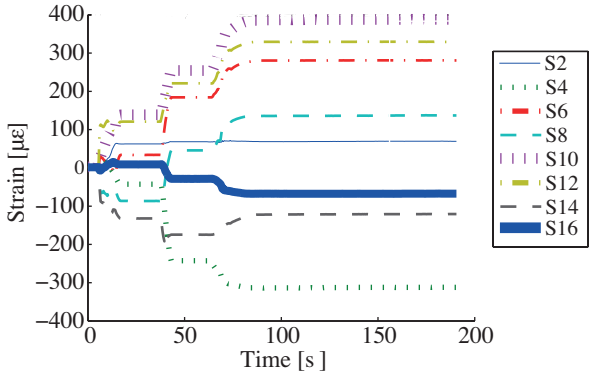

Figure 4.13: Strain gauges results at 10cm from the open end.

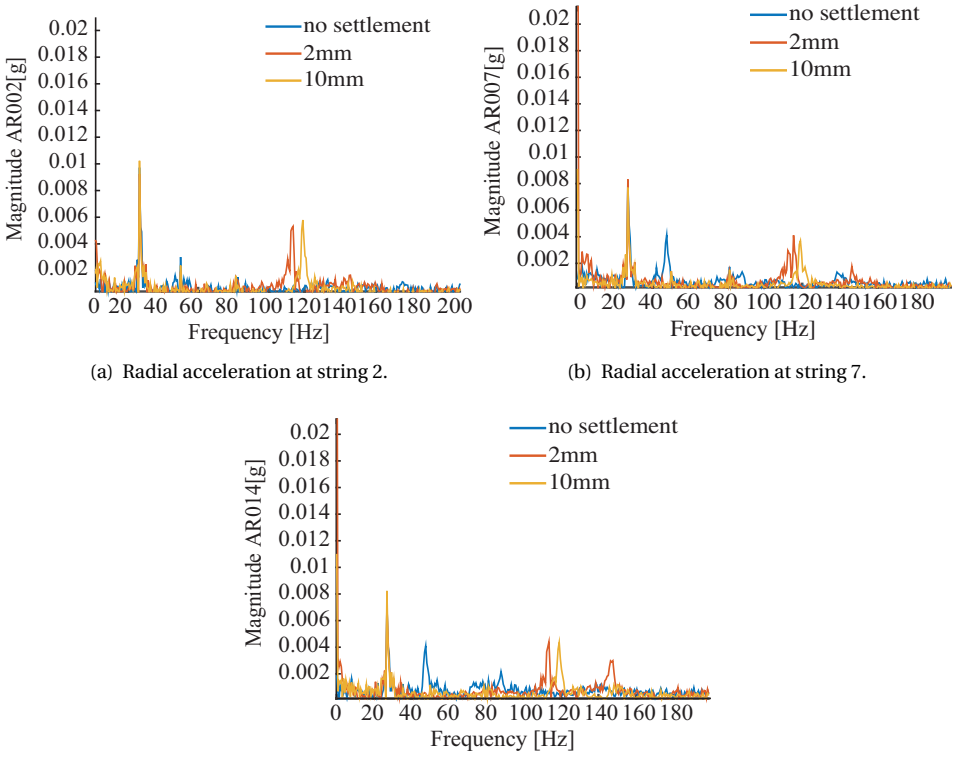

(a) Radial acceleration at string 2.

(b) Radial acceleration at string 7.

(c) Radial acceleration at string 14.

Figure 4.14: FFTs of the measured accelerations at H5 at three circumferential positions, plotted for various settlement depth.

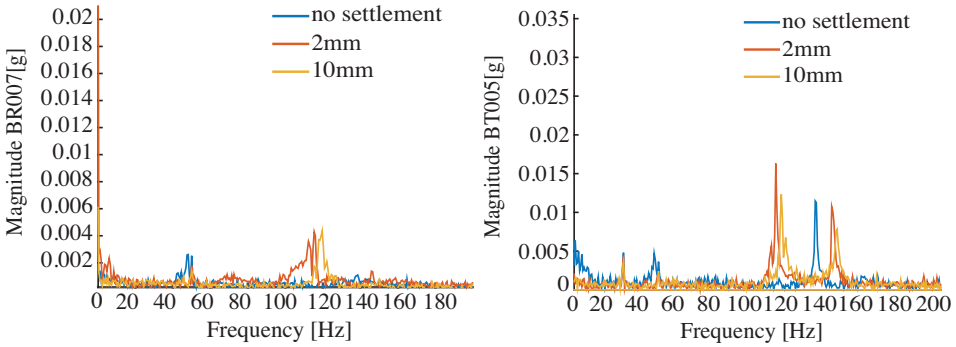

(a) Radial acceleration at string 7.

(b) Tangential acceleration at string 5.

Figure 4.15: FFTs of the measured accelerations at H50 at two circumferential positions, plotted for various settlement depth.

the DAQ boxes. An undefined time lag is present between every measured acceleration; furthermore, time lags between the three DAQ boxes made it difficult to determine the actual phase differences between the measured signals. Therefore, an additional experimental modal analysis was performed. The details of the experimental modal analysis are provided in Section 4.3.

SETTLEMENT INDUCED BY AN ELECTRIC SHAKER

The first installation experiments with electric shaker (Tests 44-51) were used to find out if the electric shaker was effective in installation of the slip-joint and investigate the effects of the choice of shaker and the amplitude of vibration on the settlement results. Additionally, in the first tests frequencies up to 800 Hz were applied in order to identify the (potential) effective frequencies. The most effective frequencies in the two sets of cones were found at approximately 120 Hz for both sets and additionally at 248 Hz for set 2 and 262 Hz for set 1. Note, that the frequencies of vibration were manually noted and are therefore not given in the following figures. Additional results of the use of the electric shaker can be found in Appendix B.7 and B.8.

In Figure B.19(b), the extent of displacements of the cones are given for installation test 65 in which the frequency of the vibration, applied with an electric shaker, is kept constant at 120 Hz and the amplitude of the vibration is varied. This figure shows that a final settlement position is reached after 100 seconds. The output of the load cell at the shaker is plotted in the same Figure, which shows that the applied force in the first 100 seconds increases from 0 up to 0.1 kN. Thereafter, the maximum applied force increases to just above 0.2 kN. No additional settlement was observed, even despite the force doubling after the final settlement position is reached. Furthermore, both figures show that the settlement events occur when an amplitude of 0.02 kN is applied and that after 100s no additional settlement is observed while an amplitude of 0.3 kN is applied. Considering both the settlement and applied force by the shaker, it can be observed that, the amplitude has a limited influence on the final settlement position. The operational frequency range of the electric shaker is greater than that of the eccentric motor which allows investigation into the other potentially effective frequencies of the system. Therefore, after reaching the settlement shown in Figure 4.16(a), the frequency was slowly increased up to 2 kHz. No additional settlements were observed during this process. However, when a frequency higher than 120 Hz was used prior to any settlement, a new effective frequency was found at approximately 248 Hz (Test 53) and 262 Hz (Test 75) for set 2 and 1, respectively.

This shows that more effective resonance frequencies that allow vibration-induced movement of the cones are present. An example of such a case is given in Figure 4.16(b). This figure presents the settlements and forces at the shaker in test 53. In this test an axial force of 28 kN and a constant frequency of 248 Hz were applied. During the test, the amplitude of the force was increased in a step-wise manner. The figure shows that the first four amplitude steps resulted in a settlement step, with a total settlement of 5 mm. Each settlement event reached an equilibrium depth after a short period. After the fourth step, the additional increase of the amplitude had no effect. These results demonstrate that the settlement level of the joint is controllable by the applied ampli-

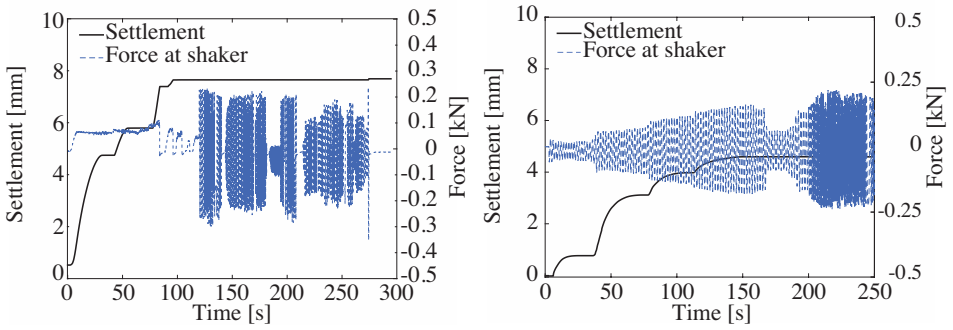

(a) Shaker force and displacements, Test 65

(b) Shaker force and displacements, Test 53

Figure 4.16: Displacement of the cones and the applied force of the electric shaker while vibrating with a frequency of (a) 120 Hz and axial force F_{ax}=10 kN and (b) 248 Hz, axial force F_{ax}=28 kN

tude of the force and that the settlement stabilizes after each event.

The tests performed with the electric shaker demonstrate that it is not the amplitude of the vibration but its frequency that determines whether settlement/movement occurs or not. The degree of settlement is, however, not insensitive to the magnitude of the vibrations, as a minimum force level is required to induce relative displacements. Furthermore, the amplitude presents itself a controller of the settlement level. Note that the direction of the vibration applied with this shaker is horizontal and that the settlement results are similar to that of the eccentric motors. The combination of the lower amplitude and the direction of application of the vibration demonstrates that shaking at certain (resonance) frequencies is effective in terms of vibration-induced movement.

The results obtained with electric the shaker demonstrate that the settlement limit is reached with vibrations that are within the operational frequency range of 0 to 200 Hz. This makes it unnecessary to go beyond this frequency range for effective installation and dismount purposes.

DISMOUNT TEST RESULTS FOR VIBRATIONS WITH THE ECCENTRIC MOTORS

Figures 4.17(a) and 4.17(b) present the displacements and vibrational frequencies of tests 15 and 83 and represent the results of two types of dismount tests. These figures demonstrate that a slip-joint can be dismounted in exactly the same manner as it is installed. Figure 4.17(a) follows the exact procedure of installation (used in section 4.2.4), using a step-wise increase in frequency, with the exception that a pulling force is applied in order to separate the two parts. Figure 4.17(b) is similar to that of the frequency ramp-up test, except that a pulling force is used. Both tests give the same end result, which is that the cones separate at a frequency of approximately 120 Hz.
Besides the attempts to dismount the cones with other frequencies than 120 Hz, many other attempts were unsuccessful in dismounting except when the frequency of 120

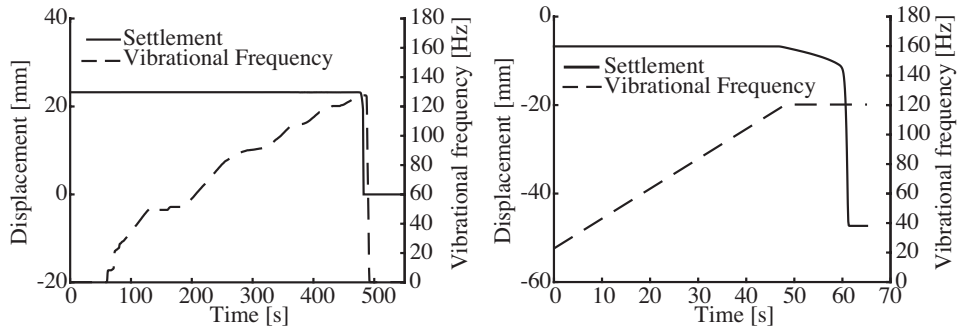

(a) Step-wise increase, Test 15

(b) Constant increase, Test 83

Figure 4.17: Displacement of the upper cone for dismount tests using eccentric motors and applying different methods of increasing the frequency of vibration up to 120 Hz in combination with a pulling force of 15 kN

Hz or a greater pulling force was applied. This confirms the importance of this specific frequency and indicates that this frequency is the most effective in allowing settlement to occur in this case.

Figure 4.17(b) clearly shows the time dependence of the vibration-induced settlement. At the instant that the frequency of 120 Hz is obtained, the cone starts to move, but it requires time to finally become separated. This again confirms the previous observation, made in section 4.2.4, that the duration of vibrations at a frequency influences the amount of movement/settlement to occur.
An effective pulling force of 15 kN is necessary to dismount the joint. This magnitude is similar to the self-weight of the transition piece, indicating that, on full-scale, the same lifting equipment as used for installation can be used for dismounting.

DISMOUNT RESULT FOR VIBRATIONS APPLIED USING THE ELECTRIC SHAKER

The exact same end results as presented for the eccentric motors were obtained when an electric shaker was used. Again, the most effective frequency for this procedure is found to be 120 Hz. An additional effective frequency for dismounting was found at 249 Hz during the first few dismount test with the electric shaker. A larger pulling force was, however, required in these dismount tests. Overall, an electric shaker is thus as effective as the eccentric motors when it comes to the dismount of the cones. That both actuators lead to the same behaviour underlines the dominant influence of the frequency of vibration in the behaviour of the joint when it is subjected to vibrations.

4.2.5. COMPARISON OF THE RESULTS OBTAINED WITH THE ECCENTRIC MOTORS AND THE ELECTRIC SHAKER

Both actuators have shown to be effective in creating settlement for installation purposes. The settlement that is obtained with both actuators is comparable; the resulting displacements obtained with the electric shaker are, however, slightly smaller. This may

(a) Wear marks on the TP

(b) Wear marks on the TP

Figure 4.18: Wear marks on the monopile and transtions piece of set 1 taken after test 42.

be attributed to the wear of the cones that occurred due to repetitive installation and dismount tests. In Figures 4.18 and four photographs of the inner surface of the TP and the outer surface of the MP show the wear marks of set 1 after test 42.

The electrodynamic shaker tests were performed after the execution of the tests with the eccentric motors. A slight decrease in final settlement position was observed after repetitive testing of installation in both sets of cones. From the 10^{th} repetitive installation test the decrease in final settlement level increased. This observation is partly in line with that made by Nolle and Richardson (1974), who demonstrated with experiments that the friction coefficient between surfaces in contact increases as a result of repetitive testing.

Settlements can be obtained with vibrations at the same (resonance) frequencies using both types of actuators. For both types, the final settlement level is obtained with vi-

bration at the frequency of approximately 120 Hz. With regard to the force magnitude and its amplitude, large differences are observed between the two actuators, with the average force of the eccentric motors being 50 times higher when compared to that of the electric shaker. At 120 Hz, the amplitude of the force of the electric shaker is found to be up to 250 times smaller than the one of the eccentric motors in installation test. This difference in force magnitude and the similarities in terms of the settlement obtained clearly demonstrates that the frequency of the vibration is dominant in the settlement process. Furthermore, given the limited amount of force required, it can be expected that such electric shakers will be widely adopted.

The different approaches adopted to the application and incrementing of the frequency indicate that all of the methods lead to similar settlement levels. The direction of the vibration, be it either horizontal or vertical, did not lead to differences in the results. This shows that the system is unaffected by the direction of the vibratory load, which would make it more easily applicable for practical purposes. Of all of the installation methods used, the 'slow' frequency ramp-up method demonstrates the highest potential to be used in practice, as it requires the least instructions and knowledge of the dynamic properties of the system.

Both actuators are effective for dismount, given the condition that one of the effective resonance frequencies is used. The amplitude of the vibration is less relevant, but it can be used to influence the final settlement position up to a certain amplitude magnitude. These observations demonstrate the effectiveness of vibrations in creating settlement in this joint.

4.3. EXPERIMENTAL MODAL ANALYSIS

In the experiments described in the previous section, settlement of the slip-joint was observed to only occur at specific frequencies. In order to obtain a better understanding of the physical behaviour, an experimental modal analysis is performed of a situation in which the slip-joint has reached is final stick position. This section describes the measurement method and setup, the processing of data, the resulting frequency responses (transfer functions), and the operational deflection shapes or mode shapes of the cones.

4.3.1. MEASUREMENT METHOD AND DESIGN

The goal of this experiment was to identify the mode shapes and corresponding frequencies of the scaled slip-joint specimen. An experimental modal analysis was performed using a multi-setup strategy (the so-called roving sensor method). PCB Piezotronics' high sensitivity tri-axial integrated circuit piezoelectric (ICP) accelerometers (model: 356B18) were used to measure the responses produced by hammer impulses at specific locations at the cone. The ICP 086D05 impulse hammer was used, in combination with a soft tip. According to the operational manual, this tip is appropriate for a frequency range of 0-200 Hz, which was confirmed by testing several tips and examining their responses. For details on the PCB equipment, refer to PCB Piezotronics (2007a,b,c).

An individual impact is simultaneously measured by five accelerometers. To sense the complete cone with five sensors these sensors need to be ranged around it. In total, 320 locations along the cone surface are measured. Impacts are applied in two directions using the impulse hammer. Given the principle of reciprocity (Barber, 2010), it is possible to determine the total response of the structure in this manner. Orlowitz et al. (2015) compared the use of simultaneous and multi-setup strategies in operational modal analysis. They showed that, in comparison to the use of simultaneous measurements, errors can occur in damping estimations when using a multi-setup strategy. For determining mode shapes, no major differences were identified between the strategies; therefore, the use of the multi-setup strategy is acceptable when the goal is to gain insight into the mode shapes.

Mueller-BBM-Vas' PAK MKII data acquisition system is used (Mueller-BBM, 2013). This DAQ is different than the one used in section 4.2 and measures the output of the accelerometers with a high phase accuracy (to be specific, a <0.5 ° @ 10 kHz phase accuracy) between the measured signals.
The ICP hammer is applied at two locations. The two impact locations have an angle difference of 90 degrees, with the result that the responses of the cones to two force directions are measured. Figure 4.19 offers a photograph of the execution of one of the performed measurements, in which the accelerometers and the impact hammer are indicated. The short horizontal stripes on the pile mark the measurement locations of the accelerometers (five of the 320 locations are pointed out in the photograph).

4.3.2. DATA PROCESSING

The sensor data for each setup are acquired in local coordinates. To create a single model of the structure, the data is therefore first converted to a global coordinate sys-

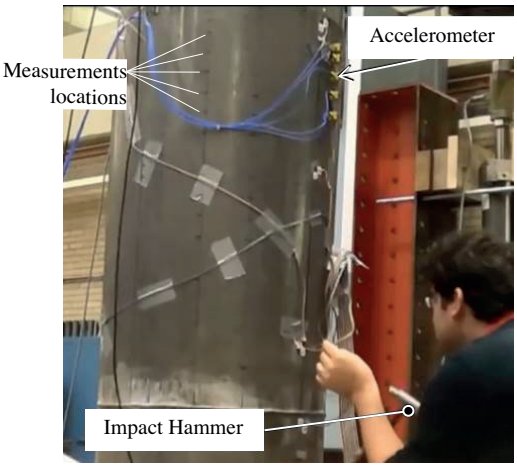

Figure 4.19: Experimental modal analysis execution.

tem. Frequency response functions (FRFs) are created directly from the measurements taken by the PAK system; this system allows a user to directly select the window of the input (hammer impulse) in order to do so. Figure 4.20 gives the modulus of the FRFs of the measurements at the two driving points. For each frequency of the FRFs, an operational deflection shape (ODS) can be obtained when the amplitudes and phases of all measured signals are combined and plotted with the correct sensor coordinates and directions. Only at response peaks that are present in several FRF measurements can a mode shape be found. For a clear explanation of the differences between a mode shape and an ODS, the reader is referred to Richardson (1997).

To obtain the mode shapes of the measurements, SDtools' Structural Dynamic Toolbox (2008), is used. For detailed information on the toolbox, the reader is referred to this software's user manual (SD Tools, 2016). This toolbox uses a frequency domain decomposition method for estimating mode shapes. A clear explanation of the classical frequency domain decomposition method is given in Brinker et al. (2001).

4.3.3. IDENTIFIED MODE SHAPES

A mode shape can be found by selecting one of the response peaks. The SDT toolbox uses the amplitude and phase responses of all measurements corresponding to that specific (resonance) frequency. The mode shapes at 86 Hz, 106 Hz, and 120Hz are found in this fashion and are plotted in Figures 4.21 to 4.23, respectively. The figures show the vibrational pattern of the mode shapes during one cycle of vibration at various instances in time. Each of the dots presents the response at that location to the specified frequency.

Each mode of a shell vibration is characterized here by a modal number (m) in the circumferential direction and a modal number (n) in the longitudinal direction, as is used, for example, in the work of Watkins and Clary (1965). The mode shape at 86 Hz has a

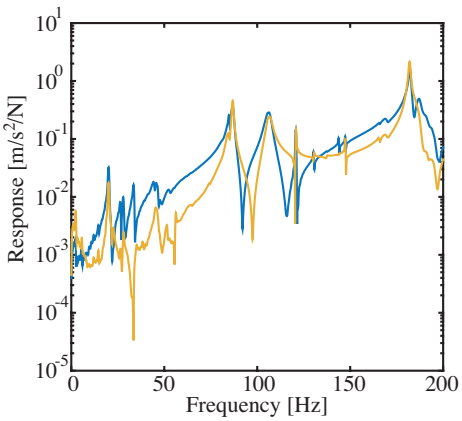

Figure 4.20: The modulus of the frequency response function of the two driving points used in the modal experiments.

triangular, antisymmetric shape and is characterized by the third circumferential mode m=3 and the longitudinal mode n=0. At 106Hz, the shape of vibration is more squared and resembles the fourth circumferential mode m=4 and the longitudinal mode n=0. The mode shape at 120Hz is a symmetric one and is characterized by the second circumferential mode m=2 and the first longitudinal mode n=1. Remarkably, this latter shape shows that the lower end, which is located further away from the initial contact (the open end of the TP), is more flexible. With regard to the mode shapes, it is important to note that not only symmetric mode shapes but also asymmetric ones are effective in terms of achieving settlement. A video-link to the modal shapes is available at `https://youtu.be/Wt4ODFMCUkk`.

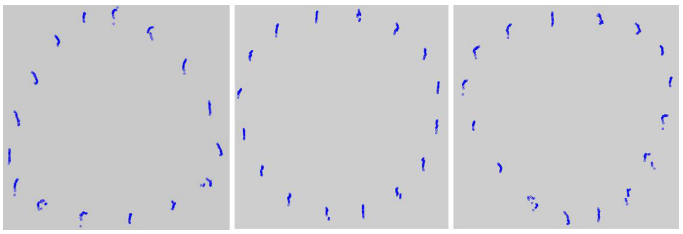

Figure 4.21: Resulting operational mode shape at 86Hz.

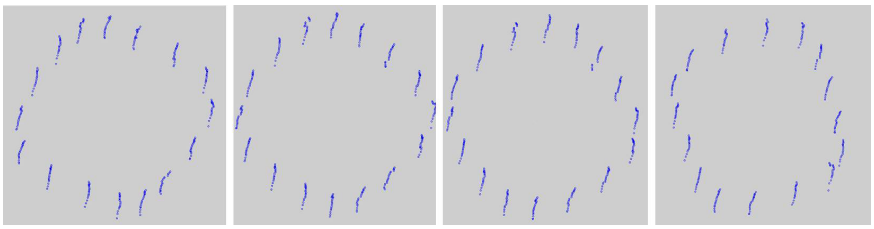

Figure 4.22: Resulting operational mode shape at 106Hz.

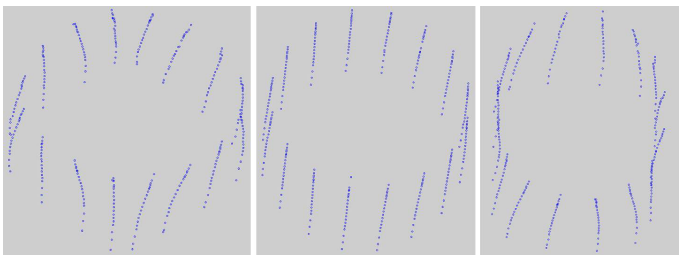

Figure 4.23: Resulting operational mode shape at 120Hz.

4.3.4. CORRESPONDENCE OF THE IDENTIFIED MODE SHAPES WITH OBSERVED EFFECTIVE FREQUENCIES FOR SETTLEMENT

The results of multiple installation tests conducted with the eccentric motors shown in section 4.2 and Appendix B show that settlement occurs at frequencies of approximately 80, 105, and 120 Hz; these frequencies correspond well with the mode shapes and their corresponding frequencies that were obtained by means of an experimental modal analysis. This correspondence proves that the mode shapes do have an effect on settlement behaviour. In particular, the mode shape around 120 Hz is effective in both the installation and dismount of the cones. This frequency is also found to be effective when the electrodynamic shaker with a significantly smaller amplitude is used. This effective mode shape is symmetric and is characterized by the circumferential mode m=2 and longitudinal mode n=1.

The main difference between the individual effective mode shapes is the presence of the longitudinal waveform of n=1 at 120 Hz. When observing the shape at this frequency, a particular behaviour is noticed: The amplitude of the response becomes larger when moving away from the area of contact and the open end of the TP. This can be explained in two ways: The first is that, with increasing distance from the open end, the stiffness decreases. The second explanation is that the areas that are in contact have a higher local stiffness than that of the areas that are not in contact.

The mode shapes do not show any discontinuity at the transition from the lower cone to upper cone. This observation demonstrates that the cones act as a combined system or a bonded condition. The settlement and mode shapes observed at specific frequencies are found to be closely related in most cases. However, some settlement events also occurred at frequencies that did not correspond to one of the modes of the system. This can be explained in two ways: The first possible explanation is that this particular settlement event is driven by the amplitude of the dynamic force. During each cycle of vibration, the axial load will temporarily surpass the static friction force, creating relative movement of the cones. The second possible explanation is that the dynamic properties and mode shapes change during the settlement process. The experimental modal analysis is only performed after full settlement is obtained. The measured accelerations presented in Figures 4.15 and 4.14 do show a change in resonance frequencies over an increasing settlement depth, therefore, it can be assumed that the effective frequencies that allow settlement change with every settlement occurrence.

4.4. MEASUREMENT OF THE DIMENSIONS OF THE SCALED CONES

4.4.1. MEASUREMENT SETUP AND PROGRAM

The goals of this experiment are to capture the status of the manufactured cones and to make a prediction concerning the development of the contact between the cones during the installation experiments on the basis of the measurements. Therefore, a single-point laser is used to perform measurements of the inner surface of the scaled test specimens. On the basis of the dimensions, an impression of the out-of-roundness and manufacturing tolerances can be obtained. Having measured the geometry, an estimation of the initial contact point is made, and an impression of the development of contact is obtained.

The RF603L laser used can measure distances of up to 50 millimetres, with an accuracy of 0.05 millimetre (RIFTEK Sensors & Instruments, 2012). The laser is attached to a beam that rotates around the centre of the cones. The beam is slightly smaller than the radius of the cones, and the laser measures the distance from the laser emitter to the cone surface. Figure 4.24(a) depicts the laser setup.

Before starting a measurement, the sensor is first positioned and fixed at the desired axial location inside the cone using an extendible beam. The laser then starts to measure, and the beam rotates 370 degrees clockwise, measuring the distance from the laser to the surface of the cone for every degree (the forward loop). The beam then rotates counter-clockwise to the original position, measuring the distances a second time (the backward loop). This process is repeated for all of the relevant axial positions, using steps of 1 to 2 cm. Rotations of 370 degrees are used to create an overlap in the measurements. This overlap is desirable, as it allows for the removal of the influence of transient behaviour at the start and end of a measurement. Furthermore, the forward and backward loops provide two sets of data on which the actual distance can be based. Figure 4.24(b) shows a photograph of the measurement setup used in the Stevinlab at TU Delft, in which the laser setup and the extendible beam are shown. A data point contains the measured distance at a certain angle and axial position of the laser. The acquired data are used to create a virtual 3D model of the two cones.

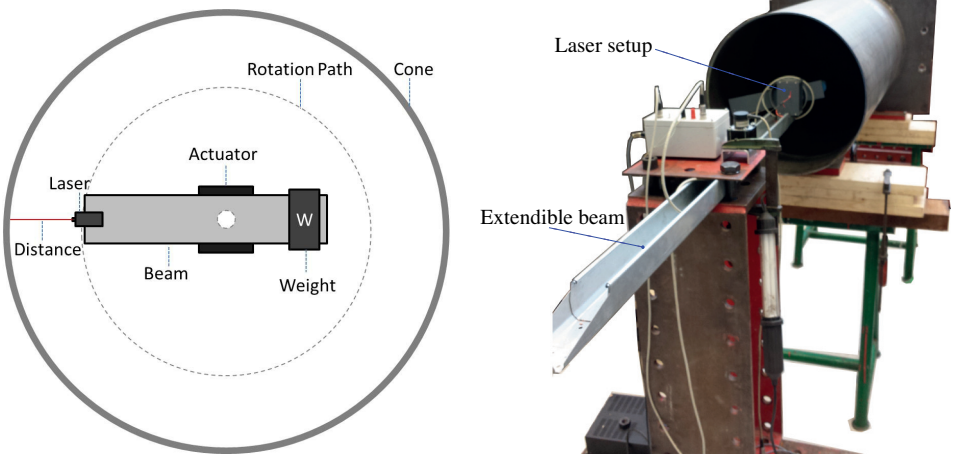

(a) Laser setup for the measurement of the dimensions the slip-joint.

(b) The setup used at the Stevinlab, Delft.

Figure 4.24: Measurement setup for the determination of the dimensions of the scaled slip-joint specimens.

4.4.2. DATA PROCESSING

One of the obtained measurements at a single axial position is plotted in Figure 4.25. Here, the measured distance over the angle for the forward and backward measurements is shown. The sinusoidal shape of the measured signal is quite striking. Measuring distance from the centre of a perfectly round cylinder should produce a straight line; however, the figure clearly shows that this is not the case for this specimen.

Figure 4.26(a) shows the dimensions that result when the unprocessed data points at the various axial positions are combined and plotted; it indicates that the measurement setup and execution of the measurement resulted in errors. It is clear that the axis of measurements is not fully straight along the length of the cone. To correct the measurements, the following four steps were taken:

1. - Translation;
2. - Averaging;
3. - Rotation; and
4. - Interpolation

The first step is to the translate measurement of the backward loop to the forward loop. This is necessary because, in the event of a change in the direction of the rotation, the laser holds the same position for a short period and measures this distance. The angle, however, increases during this brief period, causing an error in the measured angle and distance between 360 and 370 degrees for the backward loop, as shown in Figure 4.25.

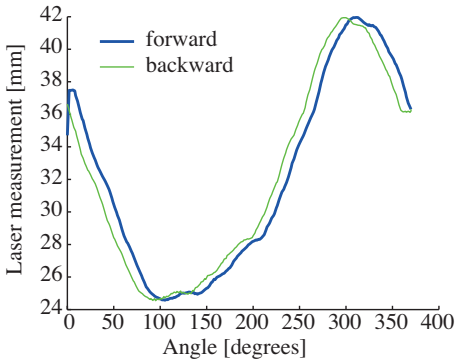

Figure 4.25: A single measurement, showing data points for both the forward and backward loop.

Subsequently, in order to minimize the measurement errors, the average of the two measurements is taken.
The rotation of the data points around the axis of the cone is necessary, as the measured data points were not obtained from a fixed central line. This causes an error when relating the measurements to one another: For example, in a joined coordinate system, the 0 degree location of three different sets of measurements should lie in a straight line. This was not the case; therefore the measurements at some axial positions needed to be corrected by adding a rotation to the data.
Between the measured rings, the data are interpolated to create a more continuous data set. This allows a more detailed analysis of the cones' contact areas. Figure 4.26(b) presents the dimensions that result after processing.

MEASUREMENT RESULT

Figure 4.27 presents a top view of the monopile part of cone set 2. In this figure the measured distance of the laser is plotted, not the actual dimensions. As a result, the imperfections and the out-of-roundness of the cone become clearly noticeable. It is clear that the specimens are far from being perfectly conical.

4.4.3. CONTACT AREAS BASED ON MEASURED DIMENSIONS

Based on the measured dimensions, impressions of the initial contact and the development of this contact are obtained. This is accomplished by first aligning the axis (based on the processed data) of the monopile and transition piece. The distance between the two sets of data is then manually decreased until 'contact' is established; this occurs when, locally, any of the data points of the monopile measurements are equal to or larger than that of the transition piece.

Figure 4.28 shows the development of the contact of the measured set of cones, from the initial instant of contact to their final settlement position. The blue lines in the figure represent the longitudinal weld location. Initial contact appears, with an overlap of 650 mm, at a single circumferential position. By increasing the overlap length between the individual cones, the development of the contact becomes clear: It first develops at the

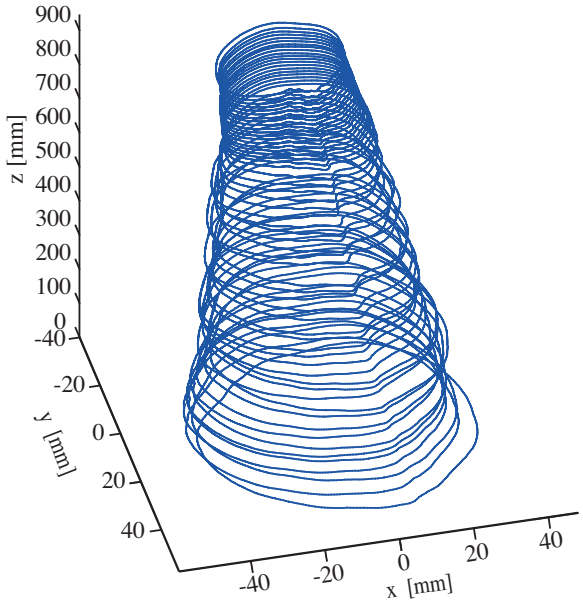

(a) Before data processing

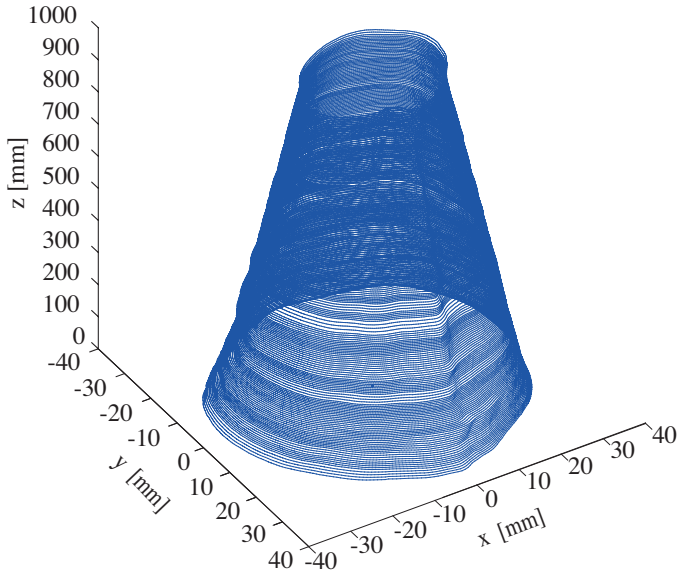

(b) After data processing.

Figure 4.26: The measured geometry of the monopile part of the scaled slip-joint specimen of set 2 before and after data processing.

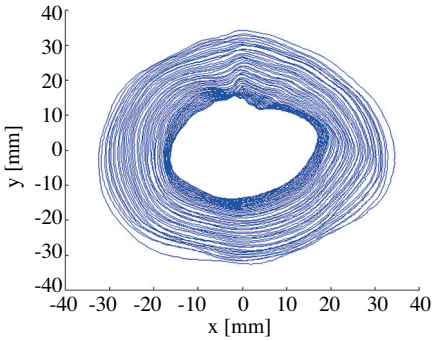

Figure 4.27: Top view of the measured monopile part.

initial contact point in a vertical direction; a second contact area is formed with increasing overlap of the cones. The contact develops further at these two distinct areas and expands in the circumferential direction with the increase in settlement/overlap.
The figures show that a large section of the surfaces are not in contact. Note that these plots are based on measurements and no deformation of the cones is taken into account. The (local) deformation will increase the contact surfaces, and the contact status presented should therefore be considered to be conservative (minimal).
These measurements and the estimation of the contact provided in Figure 4.28 provide an explanation for the non-uniform strain behaviour measured during the installation test, as presented in Section 4.2.4.

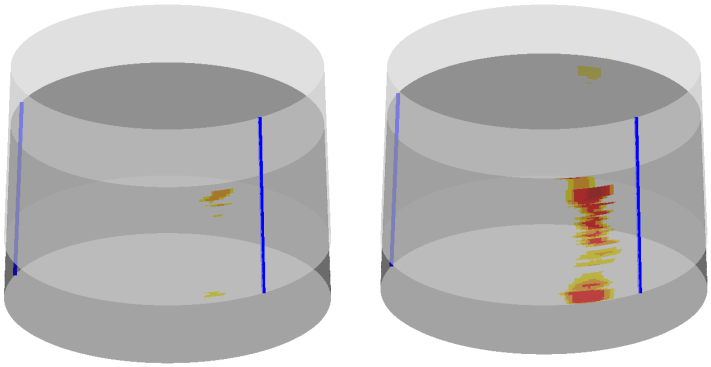

(a) 650 mm (b) 700 mm

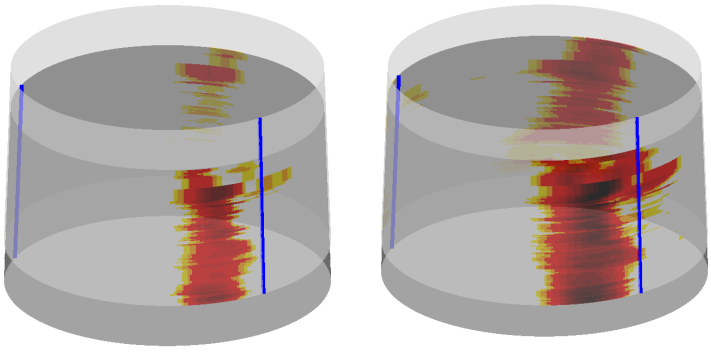

(c) 750 mm (d) 800 mm

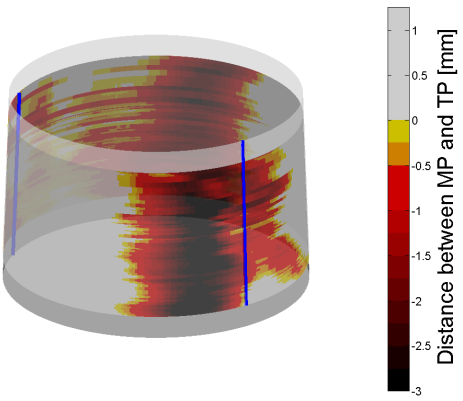

(e) 860 mm

Figure 4.28: Contact development as function of the overlap based on the measurements of the slip-joint's dimensions conducted on the cones of set 2.

4.5. CONCLUSIONS

A new method for installing and dismounting slip-joints for offshore wind turbines has been investigated experimentally. This method consists in the application of vibrations to the upper part of the joint in order to allow relative movement between two cones. The use of vibrations during the installation and dismount was investigated using a 1:10-scale model of the slip-joint. A set of eccentric motors and an electrodynamic shaker were used to apply the vibration on two identical sets of slip-joints.

The results of the installation and dismount tests demonstrate that the shaking frequency is key to the successful installation/dismount of a slip-joint. Specific (resonance) frequencies of the vibration were found to be effective and allow for relative movement. The settlement obtained was found to not be proportional to or even correlated with the amplitude of the applied force. The cones demonstrate a stabilizing behaviour during the sliding events.

The installation tests performed with a constant increment of frequency up to 120 Hz demonstrated that, when the increment of the frequency is too large, the settlement has less time to develop. As a consequence of this, smaller settlement distances will be obtained than would be obtained using a smaller increment of frequency increase. The same tests also indicated that the method of a constant increase in frequency of vibration leads to similar displacements as the stepwise increase in frequency, if a relatively small increment of the frequency is used. This method of constantly increasing the frequency of vibration has the advantage of simplicity and could therefore be an option for actual full-scale implementation.

The strain levels measured during the tests remained well within the elastic regions. These measurements showed a non-uniform deformation around the circumference, indicating a non-uniform contact. This non-uniform contact can be explained by the result of the measured geometry of the cones of set 2 and the prediction of the contact based on these measurements.

The dismount tests showed that the cones could be dismounted most effectively when vibrating at 120 Hz, which correspond to the second circumferential mode and first longitudinal mode. This emphasizes the importance of this specific frequency and indicates that this frequency is the most effective in allowing settlement/ relative movement to occur.

The use of the electric shaker made it possible to investigate the influence of the amplitude of the vibration applied and to inspect the effectiveness of frequencies outside the eccentric motors' working spectrum of 0-200 Hz. The results of these tests showed that similar settlement levels are obtained with an amplitude 250 times smaller than that provided by the eccentric motor (when rotating at 120 Hz).
The stabilizing behaviour of the settlement and the ability to control the settlement level demonstrate that the application of vibrations represents a controllable method for installing and dismounting of a slip-joint.

The experimental modal analysis demonstrated that some of the frequencies observed as being effective in terms of producing settlement events correspond to natural frequencies of the combined system. In particular, a frequency of 120 Hz is effective in both the installation and dismount of the pieces and corresponds to one of the measured modes. This effective mode shape is characterized by a circumferential mode m=2 and a longitudinal mode n=1 of a conical shell. Furthermore, this mode shape is effective in achieving settlement using an electrodynamic shaker that provides a significantly smaller amplitude.

Based on the measured dimensions, impressions of the manufacturing tolerances, the initial contact, and the development of the contact have been obtained. The measurements of the individual cones indicate that the cones are far from being perfectly conical. By overlapping the measurements of the two cones, an initial contact point and the development of the contact areas can be estimated. The contact between the two cones develops at two distinct areas and expands in the circumferential direction with an increase in settlement. The contact is observed to be asymmetric, which is in line with and explains the strains measured around the circumference during the installation experiments.

These experiments prove that the vibration assisted settlement of a slip-joint is possible and that the frequency of vibration is key to a successful settlement process. Vibration-induced settlement can thus be used in either the installation or dismount of a slip-joint. In the next Chapter a finite element model of a slip-joint is presented with which predictions of the settlement behaviour of the two cones under influence of vibration are attempted.

5

A FINITE ELEMENT MODEL OF A SLIP-JOINT UNDER THE INFLUENCE OF VIBRATIONS

5.1. INTRODUCTION

The experiments presented in Chapter 4 demonstrate the effectiveness of vibrations in terms of inducing a relative movement of the upper cone of a slip-joint. Furthermore, the experimental data show which structural modes are most effective for achieving settlement between the cones of this joint. This data also provide a basis for the refinement of the lumped element model presented in Chapter 3. This Chapter presents a finite element model that can capture the behaviour of a slip-joint's cones when vibrating in their most effective modes. This model includes the structural modes of the two cones, whereas the lumped-element model discussed in Chapter 3 only includes the rigid body motions. The goal of the finite element modelling is to qualitatively reproduce the results of the conducted experiments. Therefore, this numerical analysis focuses on capturing and understanding the stick-slip behaviour that is observed at various forcing frequencies. This is done by means of a time-domain analysis that mimics the installation process executed in the experiments. A step-wise increase of the frequency is used with reference values for parameters such as the friction coefficient.

Section 5.2 describes the finite element model and discusses its uncertainties. In Section 5.3, this model is used to reproduce the results obtained in the experiments. Several time-domain analyses are executed for cases similar to the experiments in Chapter 4. In order to investigate the uncertainties in the model, Section 5.4 presents a parametric study. In Section 5.5 a discussion on the presented results is given and the conclusions are presented in Section 5.6.

5.2. DESCRIPTION OF THE MODEL

5.2.1. DETAILS CONCERNING ELEMENT TYPE AND SIZE, BOUNDARY CONDITIONS AND CONTACT MODELLING

The finite element (FE) software package ANSYS (version 15.0) is used to model the installation procedure of the slip-joint. The FE model used consists of a TP and MP part, as indicated in Figure 5.1. Both cones consist of 8-node, 2^{nd}-order SHELL281 elements. Each node has six degrees of freedom (DOFs). The boundary conditions at the bottom of the MP restrict displacements and rotations in all of the six DOFs, i.e. the bottom is clamped. The top of the MP (the part that makes contact with the TP) is free.
To allow computational convergence during initial contact, it was necessary to use boundary conditions different to those that were applied for the transient analysis. In the stage of initial contact, the top of the TP is first constrained in four directions, and only displacements in the z (axial) direction and a rotation around the z-axis are allowed. These constraints at the top of the TP are removed once the TP has settled under an axial force of 10 kN, which is equal to that of the experiments fo Chapter 4. The static and dynamic forces are applied directly to the nodes at the top of the TP, as shown in Figure 5.1. The bottom of the TP is in contact with the MP and is not subjected to any external forces.

An element size of 80 mm and a total of 1,488 elements are used in the model. The relatively large element size reduces the calculation time significantly and serves the goal of capturing the settlement behaviour of the cones under the influence of vibrations in a qualitative manner. To accurately get stress levels at the local positions, a smaller mesh size is required. Young's modulus, the Poisson ratio and the density of steel are taken as 210 GPA, 0.3, and 7850 kg/m^3, respectively.

The contact between the two cones is modelled using surface-to-surface elements Conta174 and Targe170. These contact elements are chosen because they are applicable for a surface-to-surface contact situation. As the two cones have different cone angles, it is appropriate to use the so-called 'asymmetric' approach to contact modelling. This asymmetric approach to modelling means that the contact pair consists of one contact and one target surface; it allows the target area to penetrate the contact area during the solution but not vice versa. For the contact force calculations, the Augmented (penalty-based) Lagrange algorithm is used, given its effectiveness to the frictional contact problem. The inclusion of the shell thickness effect is activated through keyoption (7-11). Using this keyoption, the contact distance is calculated using the thickness of the shell instead of the mid-surface nodes of the surfaces.

5.2.2. THE APPLIED FRICTION MODEL

The friction model is one of the uncertainties of the model. An appropriate friction model is chosen from literature on friction models and coefficients.
Rabinowicz (1958), among others, demonstrated that the friction coefficient depends on relative velocity and, furthermore, that the transition from stick to slip depends on

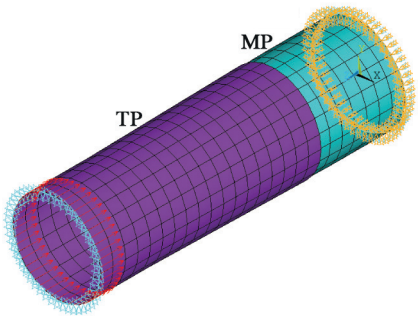

Figure 5.1: FE model of the slip-joint with the initially applied boundary conditions and forces indicated.

the relative motion of two items in contact. In another paper (Rabinowicz, 1956), he also stated that the static coefficient of friction depends on the period of time for which surfaces have been in contact. Blau (2001) lists eight factors that influence the frictional behaviour and states that the large number of factors and uncertainty are the main reasons why, even today, no universal predictive theory exists for friction. This emphasizes the difficulty in choosing correct friction coefficients that would allow the FE model to qualitatively and quantitatively reproduce the settlement results of the experiments discussed in Chapter 4.

The friction model that is used in the FE model presented here is defined using both a dynamic, μ_d, and a static, μ_s, friction coefficient. In ANSYS such a friction model is defined as follows:

$$\mu = \mu_d + (\mu_s - \mu_d) e^{-d_c V_{rel}} \tag{5.1}$$

This friction model is a function of the relative velocity, V_{rel} and a decay function d_c. Investigating the theory behind this model, it transpires that ANSYS uses a dynamic friction model that was proposed by Bo and Pavelescu (1982), who refer to Symmons (1969) for a value of d_c for steel-to-steel contacting surfaces. A typical value of d_c is supposed to be between 0.5 and 1 and is obtained empirically. The PhD work of Symmons could, however, not be accessed. In other literature (Armstrong-Hélouvry, 1991; Tullis, 1987; Mac Donald, 2007), the exponential decay function for friction is mentioned for friction models of all kind of materials. However, a table with values of d_c cannot be found anywhere. In Kaldunski (2016), a value for d_c of 10 is used; it is, however, unclear how this value was obtained. The documentation provided by ANSYS gives no references to sources. but states that a value of the decay function can be determined if the static and dynamic friction coefficients are know and at least one data point is known that correlates the apparent friction coefficient μ_1 with a relative velocity V_1 as follows:

$$d_c = -\frac{1}{V_1}\mathrm{Ln}\left(\frac{\mu_1 - \mu_d}{\mu_s - \mu_d}\right) \tag{5.2}$$

Publications and tables with values for friction coefficients for steel-to- steel contact are available, but their values vary. Choosing a representative friction coefficient for steel-to-steel contact is therefore not a straightforward choice. Godfrey (1967) quantified the dry friction coefficient of steel on steel to be between 0.15 and 0.36, with an average of 0.28. Furthermore, he demonstrated that the use of vibrations can decrease the friction coefficient to nearly zero without losing contact. Gaylord and Shu (1961) found the static dry friction coefficients of steel on steel to be between 0.2 and 0.5, depending on pressure and the number of repetitions of a friction test.

Like many others, Barret (1990) refers to for example, Campbell (1939) for the dry friction coefficients of μ_d of 0.42 and μ_s of 0.78.

Nolle and Richardson (1974) investigated the influence of vibrations on the static friction coefficient and showed that the type of contact (Point, sphere on plane or flat) influences the coefficient. In their paper they emphasize the wide variation of the friction coefficients used in engineering handbooks. Nolle and Richardson refer to handbooks (Marks, 1967; Kutz, 2009; Oberg and Jones, 1969) that provide a range for μ_s between 0.3 and 1.0. The results of their own experiments give an average μ_s of 0.4, and they show that the number of test repetitions also increases the static friction coefficient. Similarly to Godfrey (1967) they also demonstrate that the use of vibrations reduces the static friction coefficient. The wide range of the resulting friction coefficients discussed above illustrates the difficulty in choosing a value for the static and dynamic friction coefficients.

For the simulations in this chapter a μ_d of 0.4, a μ_s of 0.5 and a decay function d_c=100 are used. This friction model that is illustrated in Figure 5.2 has a rapid decay to allow the model to slide with small relative motions. The effect of the magnitude of parameter d_c on the model predictions is discussed in section 5.4.

5.2.3. THE MATERIAL DAMPING

A constant damping ratio of 1 % for all modes is used to specify the hysteretic damping directly using the DMPRAT command. This is a proper choice for a single material system. Other options for damping modelling in Ansys are discussed in Cai et al. (2002).

5.3. PREDICTIONS OF THE FINITE ELEMENT MODEL

5.3.1. CASE STUDY

The installation sequence is similar to that used for the experiments discussed in Chapter 4. The dimensions of the two cones are chosen to be equal to those used in Chapter 4, which are presented in Table 5.1 for convenience. At the top of the TP part, a static force and a dynamic force are applied directly at the nodes. To simulate self-weight, an axial

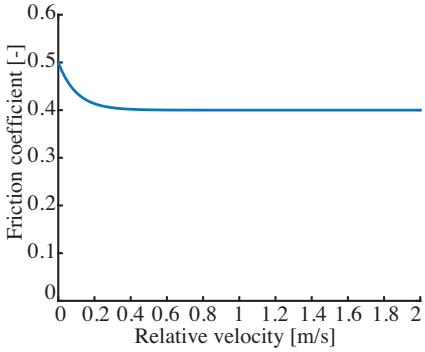

Figure 5.2: Friction model used in ANSYS

Table 5.1: Dimensions of the scaled slip-joint case study.

	Lower cone (MP)	Upper cone (TP)	Unit
Cone angle	α=1.05	β=1.0	°
Top outer diameter	0.584	0.594	m
Bottom outer diameter	0.600	0.610	m
Wall thickness	6	6	mm
Cone length	1.0	1.0	m
Total length	1.4	1.4	m
Total mass	0.15	0.15	tons

force of 10 kN is first applied. This force is applied with a constant increase of its magnitude from 0 to 10 kN over 2 seconds. After the initial step, the simulation is continued with the application of an additional dynamic force that is similar to the dynamic force F_{ecc} of the two eccentric motors. The maximum value of the applied force is frequency dependent and is given by:

$$F_{ecc} = 2\left(M_{ecc} r \cdot \omega^2\right) = 2\left(0.0046 \cdot 4\pi^2 f^2\right) = 0.3632 f^2 \tag{5.3}$$

where M_{ecc} is the eccentric mass in the motor, r is the distance between the centre and the eccentric mass in the motor, and f is the frequency in Hz.

5.3.2. PREDICTIONS OF THE MODEL AFTER THE INTRODUCTION OF AXIAL LOADS

Figure 5.3(a) depicts the force, as used for the introduction of the self-weight, at one of the nodes on the upper boundary of the transition piece. A constant increase from zero to 105 N is observed. Note that the total applied force is obtained by multiplying this nodal force by the number of nodes located at the edge and then again by two. The latter is due to the fact that the force at the element is obtained at one node. The total applied

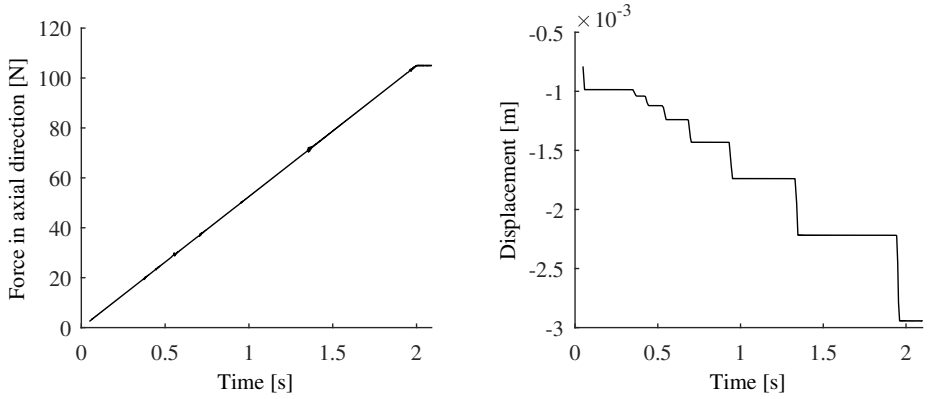

(a) The applied axial force.

(b) The displacement of the TP.

Figure 5.3: The applied axial force at a single node at the top of the transition piece for the simulation of the introduction of the self-weight of the transition piece and the resulting displacement of the transition piece.

force at the node is therefore doubled, as two elements connect to the same node.

From 2 to 2.1 seconds, the boundary conditions at the top of the TP change when the constraints are released. After 2.1 seconds, the axial force remains constant. Figure 5.3(b) presents the displacement that occurs at the lower boundary of the transition piece. This figure clearly shows the stick-slip behaviour of the settlement of the transition piece, resembling observations made during the experiments that were conducted in similar conditions.

The status of the contact between the two surfaces at 2.1 seconds is presented in Figure 5.4. This figure shows that only the bottom part of the TP is in contact with the MP. This is according to expectations as two different cone angles are used, and the contact should therefore initially take place over a small area. The figure shows that a part of the contact is sticking and another part is in sliding.

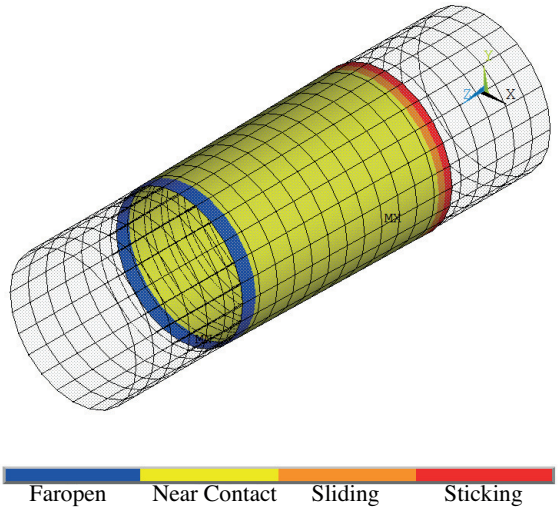

Figure 5.4: Status of the contact between the surfaces after applying the axial load.

5.3.3. THE MODE SHAPES AND THEIR CORRESPONDING FREQUENCIES AFTER INITIAL SETTLEMENT

After the self-weight of the transition piece is simulated, a modal analysis is performed in order to identify frequencies of the combined system that may prove effective in inducing settlement events when they are applied as external vibration frequencies. Figures 5.5 and 5.6 present the first 10 mode shapes that may be effective. These shapes are found at frequencies of 68, 132, 142, 160, 162, 227, 266, 276, 295, and 321 Hz. Note that the frequencies do not match the frequencies found during the experimental modal analysis, as the model does not include the bottom plate or the boundary conditions that are representative of the experimental setup.

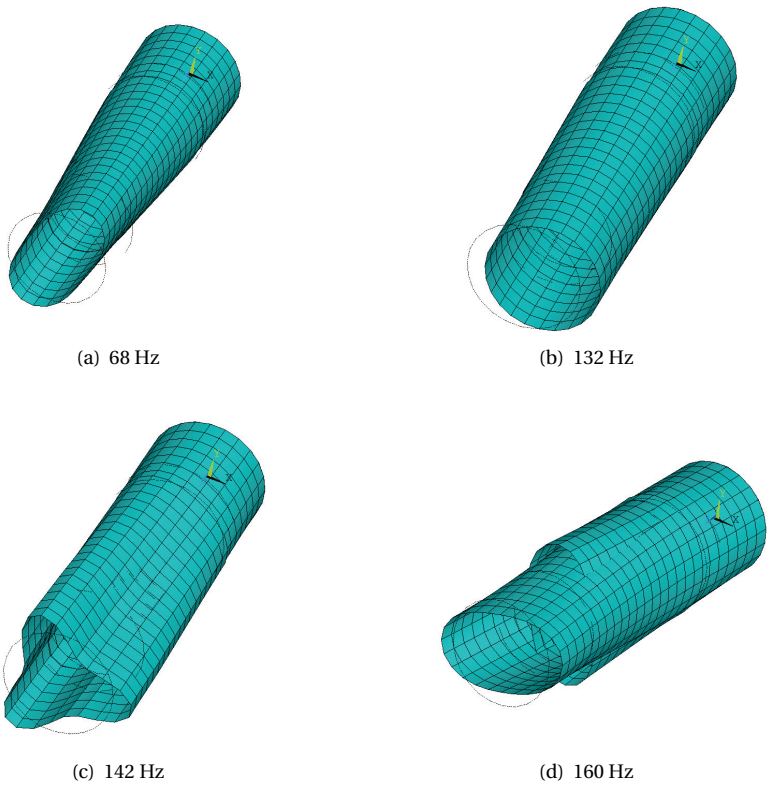

(a) 68 Hz (b) 132 Hz

(c) 142 Hz (d) 160 Hz

Figure 5.5: Modes shapes 1-4 of the combined system after initial settlement.

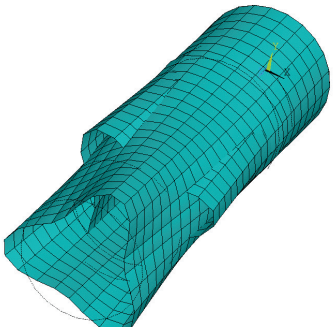

(a) 162 Hz

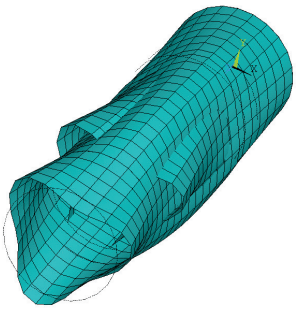

(b) 227 Hz

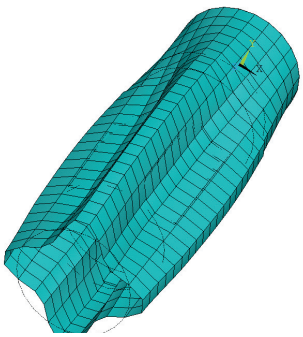

(c) 266 Hz

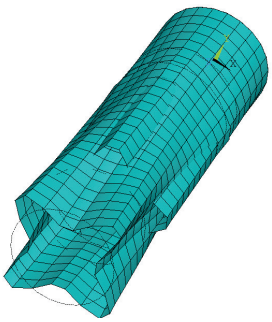

(d) 276Hz

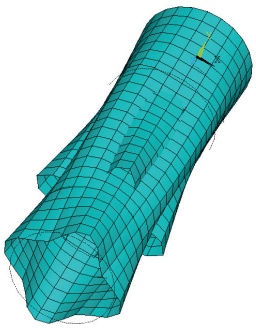

(e) 295Hz

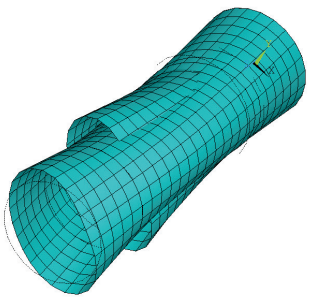

(f) 321 Hz

Figure 5.6: Modes shapes 5-10 of the combined system after initial settlement.

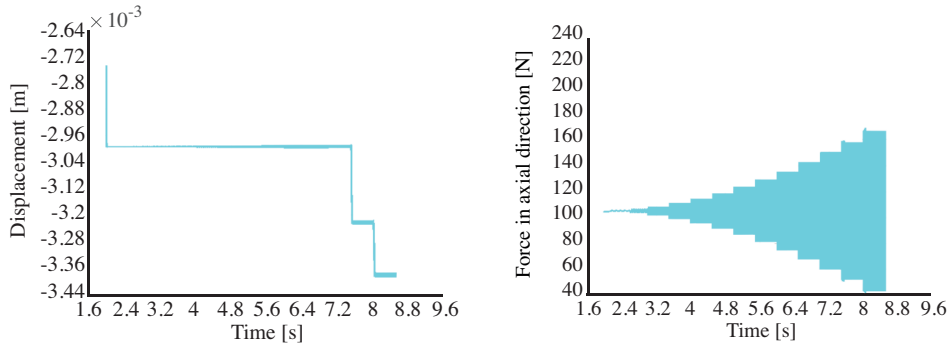

(a) The displacement of the TP.

(b) The applied force at a single node.

Figure 5.7: (a)The displacement of the transition piece achieved by the application of a vibratory load and (b) The applied vibrational load of the eccentric motors given for a single node of the upper boundary of the TP.

5.3.4. PREDICTIONS OF THE MODEL IN CASE OF EXCITATION BY ECCENTRIC MOTORS

Figures 5.7(a) and 5.7(b) present the displacement of the transition piece and the applied force in the axial direction at a node that is located at the upper boundary of the TP. From 2.1-2.5 seconds the simulation starts with a dynamic force and a frequency of 10 Hz that is applied at the upper boundary of the TP, which mimics the step taken in the experiments presented in Chapter 4. A frequency increase from 10 to 130 Hz in steps of 10 Hz is applied, with each step taking 0.5 seconds.

Figure 5.7(a) shows that only two sliding events occur, one at 7.5 s and one at 8 s. The frequency of the applied force at these instances is 120 Hz and 130 Hz, respectively. These results demonstrate that settlement does not only occur for a vibration with a frequency close to one of the natural frequencies. Based on this simulation it is unclear whether this event is driven by frequency or amplitude. Figure 5.7(b) shows that the amplitude of the dynamic force increases quadratically with increasing frequency.

5.3.5. PREDICTIONS OF THE MODEL IN CASE OF EXCITATION AT THE NATURAL FREQUENCIES

To determine if the resulting displacement that is observed is amplitude- or frequency-driven, another simulation is executed. In the following simulation, the force amplitude is limited to 3.6 kN. This force amplitude corresponds to the magnitude that is delivered by the eccentric motors at 100 Hz (see Equation (5.3)). This amplitude did not lead to any displacement in the previous simulation, as can be seen in Figures 5.7(a) and 5.7(b). This amplitude, in combination with those frequencies that correspond to natural frequencies (f_n), is used to investigate if the model will settle. Table 5.2 presents the loading sequence that is introduced in the simulation.

Table 5.2: Loading sequence for the finite element model

Time[s]	Loading detail
0.0-2.0	The static load is applied with a linear increase from 0 to 10 kN.
2.0-2.1	The static load is kept constant and the constraints at the top are removed.
2.1-2.2	On top of the static load, a vibration is applied that is equal to a vibration generated by the eccentric motor at 68Hz. (f_1)
2.2-2.3 s	The vibration is adjusted to match a vibration generated by the eccentric motor at 100Hz.
	After this step the amplitude of the force is kept the constant to that of 100 Hz, 3.6 kN in total and 75 N per node.
2.3-2.4	The frequency of the vibration is adjusted to 132 Hz (f_2).
2.4-2.5	The frequency of the vibration becomes 160 Hz (f_4).
2.5-2.6	The frequency of the vibration becomes 162 Hz (f_5).
2.6-2.7	The frequency of the vibration becomes 142 Hz (f_3).
2.7-2.8	The frequency of the vibration becomes 120 Hz (not a mode).
2.8-2.9	The frequency of the vibration becomes 227 Hz (f_6).
2.9-3.0	The frequency of the vibration becomes 266 Hz (f_7).
3.0-3.1	The frequency of the vibration becomes 276 Hz (f_8).
3.1-3.2	The frequency of the vibration becomes 295 Hz (f_9).
3.2-3.3	The frequency of the vibration becomes 321 Hz (f_{10}).

Figure 5.8(a) and Figure 5.8(b) present the displacement of the TP and the axial force, from 2.1 to 2.8 s, at one of the load- application nodes located at the end of the TP. These figures show that settlement occurs when a change in the frequency of the vibration occurs, even though no additional force is introduced at 2.3 s and 2.4 s. These settlement events can therefore be considered as being driven by frequency, rather than amplitude. The frequencies of the applied vibrations correspond with the natural frequency of the second and fourth mode. Figure 5.9 presents the displacement of the TP for 2.8 to 3.3 s of Table 5.2. The figure shows that settlement occurs at 2.8s and 3.2s. At these instances the applied vibration frequency corresponds to the 6^{th} and 10^{th} natural frequency. Note that, between 2.7 and 2.8 s, no settlement events occur while shaking at 120 Hz. This demonstrates that the settlement at 120Hz in Figure 5.7(a) is amplitude driven and that both frequency and amplitude driven settlements can be obtained with the presented model.

The settlement events demonstrate a stick-slip behaviour and resemble the frequency-driven settlement behaviour observed in the experiments discussed in Chapter 4. The settlement for each effective settling frequency shows that, after a certain period, settlement reaches an equilibrium depth. These results demonstrate that this model is able to qualitatively reproduce the behaviour observed in the experiments.

The settlement depths obtained at the end of the simulations presented in Figure 5.8(a)

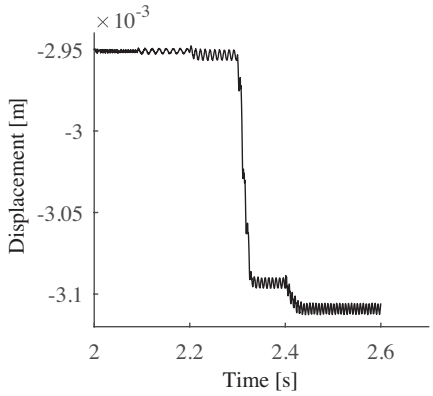

(a) The displacement of the TP.

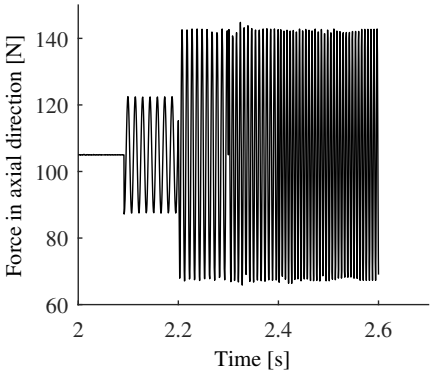

(b) The applied vibrational load in axial direction at one of the nodes at the upper boundary of the TP.

Figure 5.8: Displacement of the transition piece achieved while shaking with 68, 100, 132, 160, and 162 Hz from 2.1 to 2.6 s for the duration of 0.1 s per applied frequency and the axial load that is applied at one of the nodes located at the top of the transition piece.

and 5.7(a) show slightly different levels; this is attributed to the larger amplitude used in the simulation of Figure 5.7(a). This result indicates that the amplitude of the force influences the final settlement depth achieved in the FE model. This influence of the amplitude of vibration was observed during the experiments that were conducted with the electrodynamic shaker.

The results of the model show that the second, fourth, sixth, and 10^{th} modes are (most) effective in creating settlement. Considering the modal shapes of these effective frequencies presented in Figures 5.5 and 5.6, no clear correlation between the shapes and the effectiveness can be identified. However, some of the effective mode shapes resemble those of the 'breathing' modes. The mode shape of 321 Hz (10^{th} mode) is characterized by the circumferential mode m=2 and the longitudinal mode of n=1, which is the most effective mode shape in the experiments.

The FE model is thus capable of reproducing the observations made in the experiments discussed in Chapter 4, which demonstrated that the vibration-induced settlement of a slip-joint is frequency driven. Although settlement can be achieved by the application of larger amplitudes, the model's results show that, using smaller amplitudes, similar settlement can be obtained by selecting vibrational frequencies that correspond to the natural frequencies of the combined system. In the following section, the results obtained while shaking the system with only the frequency of the 10^{th} mode are presented in order to investigate whether a single frequency excitation produces equal settlement levels as a simulation in which the frequency of the force is changed to several effective frequencies (as presented in Table 5.2).

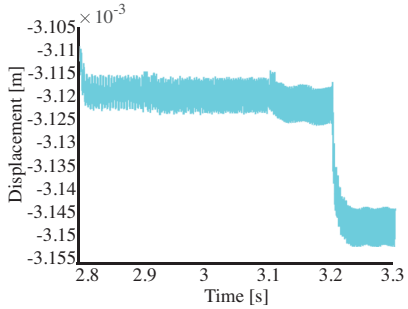

Figure 5.9: The displacement between 2.8 to 3.3 s while applying vibration of consecutively 227, 266, 276, 295, and 321 Hz during 0.1 s.

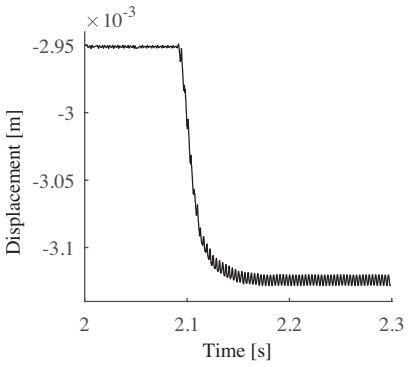

Figure 5.10: Displacement of the transition piece as a result of the applied vibration of 321Hz after 2.1 s.

5.3.6. PREDICTIONS OF THE MODEL WHILE VIBRATING WITH 321 HZ

Figure 5.10 presents the resulting displacement after initial installation under self-weight and for a harmonic vibration with 321 Hz from 2.1 to 2.3 s. The amplitude of the axial force is kept equal to 3.6 kN, as in the previous simulation. Figure 5.10 shows a slight difference in the final settlement depth in comparison to Figure 5.9. This difference indicates that vibrating with only this frequency may not be as effective as using a broader excitation band. The minor difference of only 3 μm may, however, also be a result of the numerical accuracy.

5.3.7. PREDICTION OF THE MODEL FOR DISMOUNTING BY VIBRATIONS

The dismount simulation starts at the end of the installation simulation of Figure 5.10, in which the single frequency excitation at 321 Hz is used to produce the settlement event. Figures 5.11(a) and 5.11(b) show the result of a successful dismount simulation.

Prior to the successful dismount of the transition piece, which takes place after 2.5 sec-

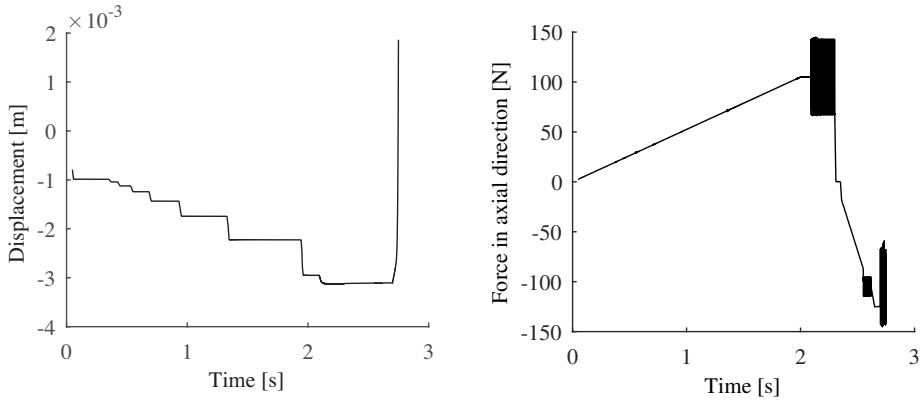

(a) The displacement of the TP.

(b) The applied forces in axial direction.

Figure 5.11: The applied forces in axial direction and the resulting displacement of an installation/dismount test, taken from a single node located at the top of the transition piece (Installation during 0-2.3 s and the dismounting starts after 2.3 s).

onds, several attempts are made to dismount the cone. In Figure 5.11(b), it is shown that the axial force increases into a pulling force after 2.3 seconds. This force simulates a net pulling force equal to the simulated weight of the cones (per node 105 N); this magnitude of force does not achieve a successful dismount. Subsequently, a vibration of 321 Hz is used with an amplitude of 0.8 kN, and no dismount is achieved. The vibration is then stopped and the axial force is increased to 125 N per node; minimal movement can be detected. The axial force is then reduced to 105 N per node, and a vibration of 321 Hz with an amplitude of 3.6 kN (per node 75 N) is used, which results in a successful dismount.

5.4. A PARAMETRIC STUDY FOR ASSESSING THE MODELLING UNCERTAINTIES

The FE model has uncertainties associated with the choice of correct parameter values and adopted models, as previously discussed in Section 5.2. This section demonstrates how the behaviour of the joint can be influenced by the choice of the parameters. Changing certain parameter values can lead to predictions of either no settlement or settlement event occurring at each frequency of the force applied. The effects of the following models and parameters are assessed:

1. Damping model;

2. The element size; and

3. The friction model.

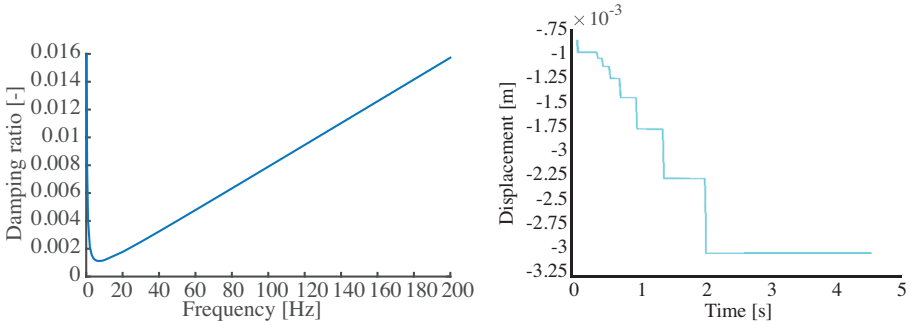

(a) The Rayleigh damping used.

(b) The achieved displacement with rayleigh damping.

Figure 5.12: The Rayleigh damping used in the parameter study and the achieved displacement while a vibration of 68 Hz, 132 Hz, 142 Hz, 160 Hz, 162 Hz is applied.

5

5.4.1. THE INFLUENCE OF THE RAYLEIGH DAMPING MODEL

An alternative to uniform modal damping in this model is the Rayleigh damping model. The damping ratio of mode n, according to the Rayleigh damping model is defined as:

$$\zeta_n = \frac{\alpha}{2}\frac{1}{\omega_n} + \frac{\beta}{2}\omega_n \tag{5.4}$$

where ω_n is the natural frequency and α and β are constants, which can be chosen such that at 132 Hz, which is found to be one of the effective frequencies for settlement in the model, approximately 1 % of critical damping is achieved. Figure 5.12(a) presents the Rayleigh damping curve that is used in the following simulation. This damping does not lead to large differences in the results for the case shown in Figure 5.7(a). Furthermore, it does not affect the results obtained while applying the vibration of an eccentric motor up to 140 Hz. If, however, the amplitude of the force is reduced in a manner similar to the simulation given in Figure 5.8(a), a change in result is observed.
Figure 5.12(b) shows the results of the model with Rayleigh damping for similar loading steps as in Table 5.2. After 2.6 s, the amplitude of the applied vibration is kept constant at 3.6 kN; subsequently, the frequency of vibration is increased every 0.5 s from 132 to 142, 160, and 162 Hz. However, no settlement is predicted.

5.4.2. THE INFLUENCE OF THE ELEMENT SIZE ON THE RESULTING SETTLEMENT BEHAVIOUR

Figure 5.13(a) presents the displacement of the TP for the same case as discussed in Section 5.3.6, using an element size of 40 mm in stead of 80 mm. The figure shows more settlement events during which the static axial load is applied as compared to the events predicted with 80 mm elements size. The final level of settlement that is obtained is comparable. Figure 5.13(b) presents the results of Figure 5.13(a), from 2 to 2.3 s. It shows that reducing the element size results in less settlement under self-weight and in a greater degree of settlement as a result of vibrations when compared to Figure 5.10. The behaviour

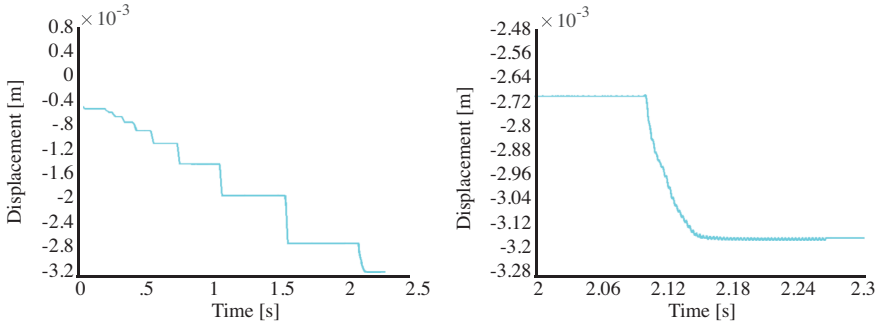

(a) Between 0 to 2.3 s (b) Zoomed in at 2 to 2.3 s

Figure 5.13: Displacement of the slip-joint model using 40 mm element size and applying vibration at 321 Hz after initial settlement under self-weight.

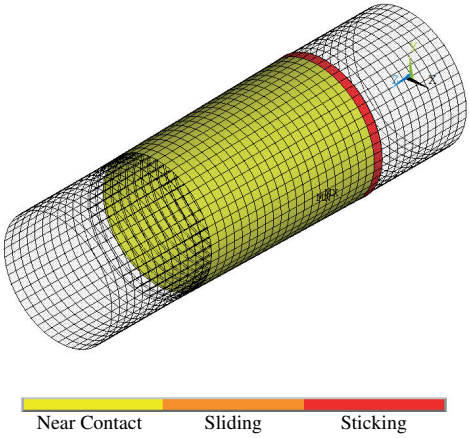

Figure 5.14: Contact status after 2.09s using 40 mm elements.

of the vibration-induced settlement of the joint does not change. The settlement event stabilizes after a certain period. Figure 5.14 shows the contact status after 2.09s. Comparing Figure 5.14 and 5.4, it can be seen, that for a smaller element size, the transition of the contact status between sticking, sliding and near contact is more visible. Thus, the resolution of the results improves and the vibration-induced settlement behaviour does not change when the element size is reduced.

5.4.3. THE INFLUENCE OF THE FRICTION COEFFICIENT ON THE RESULTING SETTLEMENT BEHAVIOUR

In the friction model several parameters can be changed. In this section, in order to investigate the influence of these parameters the friction coefficient and the decay function are varied.

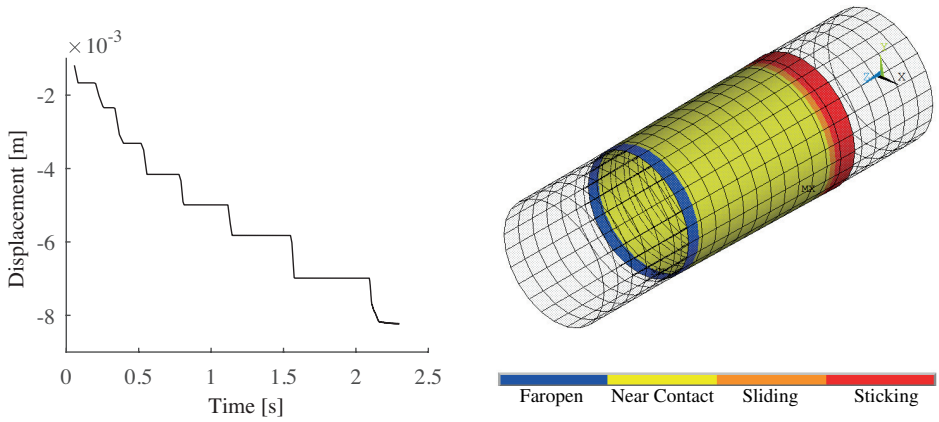

(a) Applied load in axial direction for 321 Hz.

(b) Contact status after 2.1s.

Figure 5.15: Predictions of the slip-joint model using μ_s=0.05 of (a) the displacement of the transition piece and (b) the contact status, when a vibration with a frequency of 321 Hz is applied after 2.1s.

Results are generated for a loading case equal to that considered in Section 5.3.6. The friction model is altered such that a static/dynamic friction coefficient of 0.0625/0.05 and a decay number dc= 100 are used.

Figures 5.15(a) and 5.15(b) present the displacement of the TP that is achieved for the reduced friction coefficient and the contact status at the end of the self-weight simulation. Larger settlement levels are obtained for both the simulated self-weight phase and the vibrational phase when compared to Figure 5.10.

The predicted settlement level a result of the simulated self-weight, which is finished after 2s, is comparable to the settlement levels obtained in a number of the experimental installation tests. It is thus possible to (partly) reproduce the experimental results by the use of simulations by varying the friction coefficient. The settlements that occur as a result of the applied vibration are smaller than those that were obtained in the experiments. It is therefore concluded that the frictional model may need to be improved to be able to predict the settlement resulting from both quasi-static and dynamic loads.

The contact after settling shows a clear transition from stick to slip and from slip to the 'near contact' status. The contact area, as expected, increased in comparison to the simulation that features larger friction coefficients.

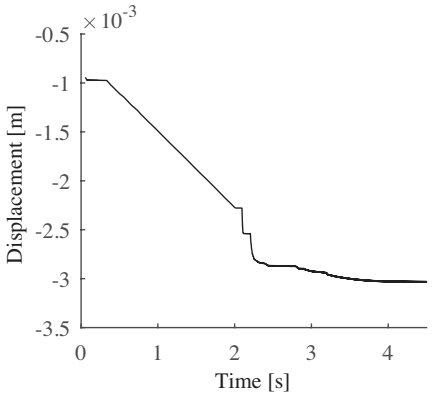

Figure 5.16: Settlement using d_c=1, achieved from 0 to 2.1s under self-weight and above 2.1 s mode 1, 2, 4, 6, 7, 8, 9, 10 is consecutively applied.

5

5.4.4. THE INFLUENCE OF THE FRICTION DECAY FUNCTION ON THE RESULTING SETTLEMENT BEHAVIOUR

Figure 5.16 presents the results for the load case of Table 5.2 using d_c=1. The results show that, for frequencies corresponding to modes one, two, four, six, seven, eight, nine, ten and also at a frequency of 100 Hz, a settlement event takes place. This result indicates that the frequency dependence of the settlement with a *dc*=1 changes compared to the other results, which illustrates that the model is highly sensitive to parameter changes. Furthermore, during the application of the simulated self-weight of the transition piece the stick-slip behaviour disappears. These two observation make it clear that the simulations are sensitive to the used d_c number.

Based on the parametric study, it can be concluded that it is a challenge to select the correct values for the parameters *a priori* in order to reproduce the experimental results.

5.5. DISCUSSION OF THE RESULTS

In this section the correspondence of predictions of the FE model and the experimental observations is discussed. The focus is placed on the effective frequencies and the corresponding modal shapes. Additionally, a closer look is taken at the physics of initiation of the slip. The effective frequencies observed in the experiments are different from those predicted by the finite element model. The reason for this difference is that the specifics of the experimental setup (the bottom plate, fixation details, etc.) were not implemented in the FE model. This was done consciously as the purpose of the FE analysis was not to reproduce the effective frequencies quantitatively but to understand the physics of the stick-slip behaviour associated with the elastic deformations of the cones.

Despite the fact that the effective frequencies do not match, the modal shapes corresponding to some frequencies are the same as those observed in the experiments. Especially, the most effective frequency was found to correspond to the modal shape m=2, n=1 (second mode in the circumferential direction and first mode in the axial one) both in the experiments and simulations. This means that the simulations are likely to be usable for understanding of the physics of the settlement process. On the other hand, not all predictions of the FE model can be interpreted straightforwardly. For example, it is not immediately clear why the axially symmetric FE model loaded by an axially symmetric force predicts settlement at the frequencies that correspond not only to symmetric but also to anti-symmetric modes. Furthermore, the FE model often predicts settlement at the instant at which the frequency of the load is changed abruptly. This gives rise to a doubt as to whether the settlement is initiated by this abrupt change or it is truly a consequence of the resonance in the system.

The latter question is addressed first. A sinusoidal load is applied at an effective frequency of 321 Hz such that the load amplitude increases gradually as shown in Figure 5.17(a). The displacement of the transition piece caused by this load is presented in Figure 5.17(b). These figures clearly demonstrate that the settlement occurs also in the case when the load frequency remains unchanged and no abrupt changes in the load take place. In order to make it obvious that the settlement is associated with resonance, the settlement process induced by the load of 321 Hz (Figure 5.17(a)) is compared to that induced by the load of 100 Hz, which has the same final magnitude and increment, as shown in Figure 5.18. The latter load shows to produce no settlement i.e. its frequency is not effective. The axial accelerations of the transition piece caused by the two loads are shown in Figures 5.19(a) and 5.19(b), which demonstrate the resonance increase of the system response at the effective frequency and a truly marginal response to a non-resonant load.

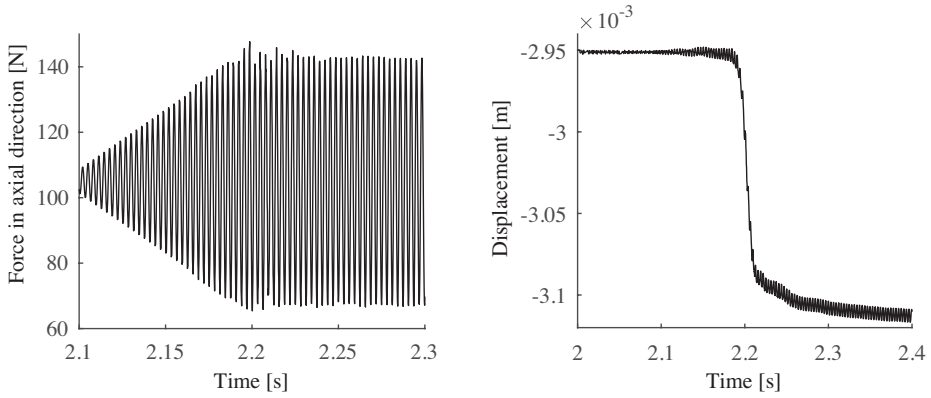

(a) Applied load in axial direction for 321 Hz.

(b) Predicted displacement for 321 Hz.

Figure 5.17: a) The applied sinusoidal load in axial direction of 321 Hz and b) the predicted displacements of the transition piece, after 2.1 s as a result of the applied load.

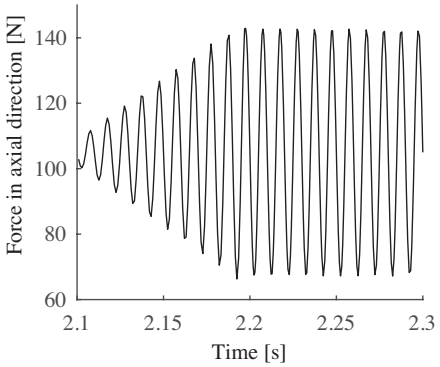

Figure 5.18: a) The applied load in axial direction of 100 Hz that is applied after 2.1 s and gradually increased in amplitude.

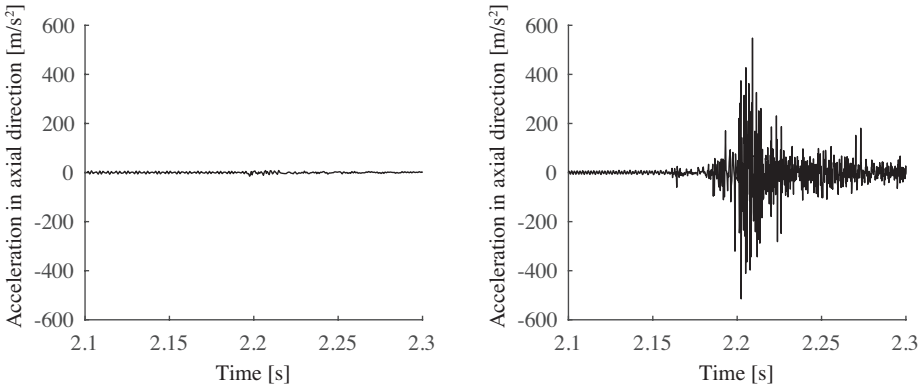

(a) Axial acceleration for 100 Hz.

(b) Axial acceleration for 321 Hz.

Figure 5.19: The acceleration in axial direction of the transition piece while a vibration of a) 100 Hz and b) 321 Hz is applied.

Let us now address the question of settlement at the frequencies corresponding to the anti-symmetric modes. Strictly speaking, in a symmetric linear system loaded by a symmetric load, excitation at a natural frequency that corresponds to one of the anti-symmetric modes should result in the zero response in the steady-state regime. However, both in the transient phase and due to a non-linearity, the response will not be zero. Therefore, it is not impossible to observe some settlement at the frequencies corresponding to the anti-symmetric modes. The settlement process at these frequencies should be greatly amplified though if an asymmetry of the load were introduced. In order to prove the latter statement, the system is subjected to the load of 132 Hz whose axisymmetric component shown in Figure 5.20(a) is supplemented by a small (5% of the axisymmetric component) lateral component shown in Figure 5.20(b). The resulting settlement is shown in Figure 5.21. One can see that during the time interval (t<2.3s) when the system is subject to the axisymmetric load only, a marginal settlement occurs. However, as soon as the lateral load is switched on, resonance starts to develop leading to a significantly larger settlement than the one caused by the symmetric load. This reconfirms the resonance character of the settlement.

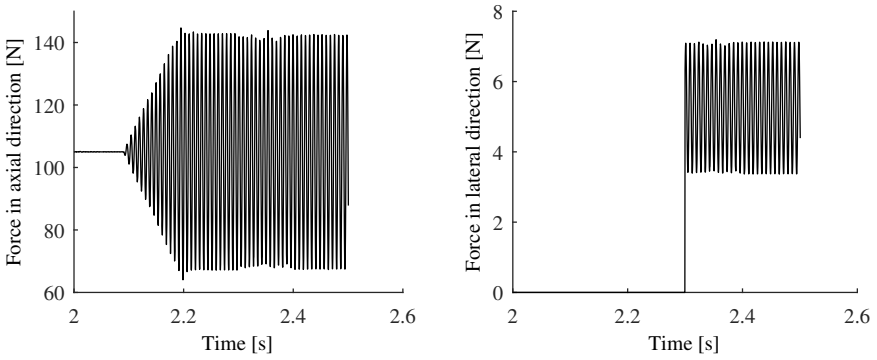

(a) Applied load in axial direction for 132 Hz (b) Applied load in lateral direction for 132 Hz.

Figure 5.20: The applied load with a frequency of 132 Hz in (a) axial direction and (b) lateral direction with an amplitude equal to 5 % of the load in axial direction.

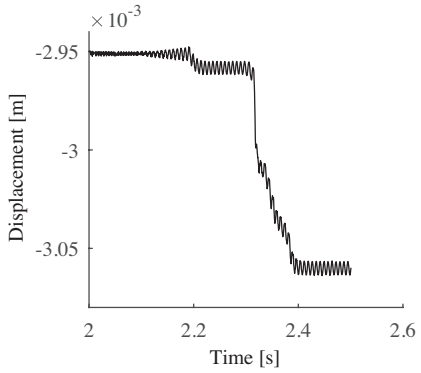

Figure 5.21: The predicted displacements of the transition piece by the application, after 2.1 s, of an sinusoidal axial load of 132 Hz and, at 2.3 s, a supplement of a lateral load of 5% of the axial load.

In order to gain insight into the details of the settlement process, the axisymmetric loading at the effective frequency of 321 Hz that corresponds to the mode m=2,n=1 is considered. The process is zoomed in the time interval between 2.19 and 2.20 seconds, which is approximately equal to 3 periods of the load. Figure 5.22 presents the vertical displacement of the transition piece, the frictional contact force acting on the transition piece (per node) and the applied force (per node) as functions of time. The figure shows that a settlement event occurs in the following manner. Initially, between 2.19s and 2.1915s, the system is in the stick phase during which the focused upon contact nodes do not move relative to each other. The global displacement of the nodes is not zero though at this phase due to the elasticity of the cones. Then transition occurs to the slip phase as soon as the frictional force reaches the maximum allowable stick load. This happens at about 2.1915s. Thereafter, a relative motion between the contact nodes is initiated and the settlement starts to progress (the absolute displacement increases steadily). Dur-

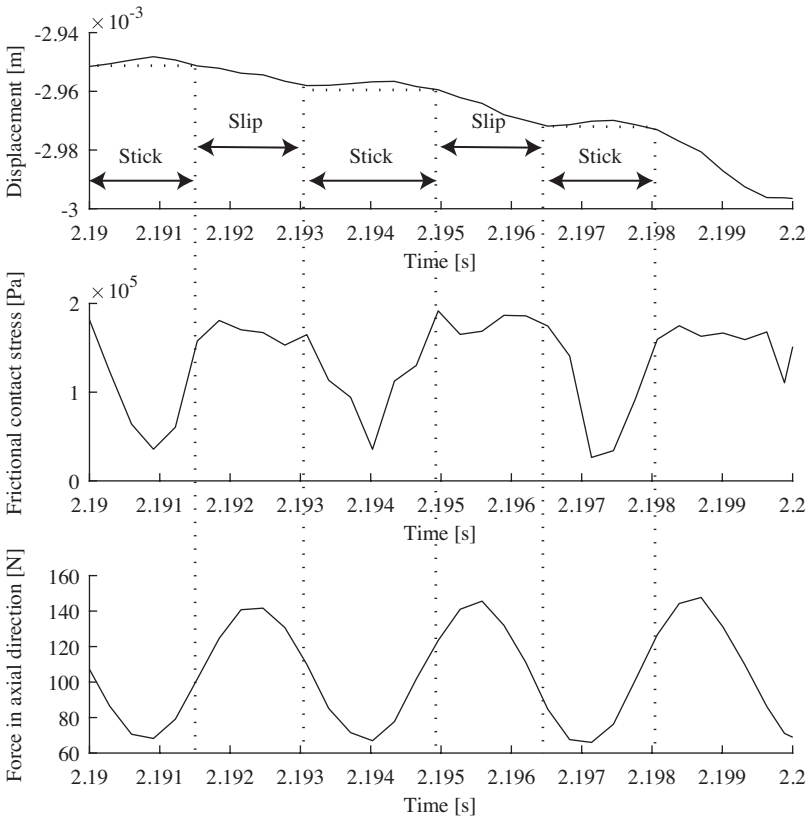

Figure 5.22: The displacement of the transition piece, the frictional force, and the applied sinusoidal load of 321 Hz in axial direction presented between 2.19 and 2.20 s.

ing this phase, the frictional force changes marginally and does not follow the signature of the applied load. Then, at a certain time instant the relative velocity becomes zero and the system returns to the stick phase. This sequence of events repeats itself quasi-periodically. Thus, the discussion above reconfirms the earlier formulated statements that the settlement is a stick-slip process that occurs at the resonance frequencies of the combined system.

5.6. CONCLUSIONS

In this chapter, a finite element model intended to investigate the behaviour of a slip-joint under the influence of vibrations is presented. The model was set up with the aim of reproducing the results obtained in the experiments in a qualitative manner. In the simulations, both a static and a dynamic force are applied directly to the nodes at the top of the TP part.

The results of the model produce a settlement behaviour that can be classified as stick-slip. A simulation of vibration-induced settlement shows that the model is able to reproduce the frequency-driven settlement events that were observed in the experiments described in Chapter 4. The frequency of vibrations at these settlement events correspond with the natural frequencies of the combined system. Besides the frequency dependence, the model reproduces the dependence of the settlement distance on the applied amplitude of the vibrations. For amplitudes below a critical value, settlement events only occur when the vibration applied causes resonance of the combined system. This specific model behaviour is also observed in the experiments.

The results of several simulations show that settlement can only be obtained while the load operates with a frequency corresponding to the second, fourth, sixth, and 10^{th} mode. The mode shape of 321 Hz (the 10^{th} mode) is characterized by the circumferential mode m=2 and the longitudinal mode of n=1, which was the most effective mode-shape combination found during the experiments.

With the same model, a successful dismount can be simulated with loads and vibration that correspond to the initial installation simulation. A dismount was simulated with an axial pulling force that is similar to the simulated self-weight and a frequency that corresponds to one of the natural frequencies of the combined system. Pulling with a larger axial force did not lead to a dismount unless vibration at the effective frequency of 321 Hz was applied. This result shows that the experimental observations can be reproduced qualitatively by this model.

A parametric study was carried out to investigate the uncertainties associated with this finite element model. It is shown that, the model predictions are extremely sensitive to the parameters of the friction model, which were not directly measured in the experiments. The model predictions are also sensitive to the choice of damping model and the damping coefficients. This is expectable given the resonance character of the settlement process.
A reduction of the element size slightly influences the results during the axial loading phase. However, the overall behaviour of the model under vibration remains unchanged. This study demonstrated that it is challenging to select the correct values for the parameters *a priori* when attempting to reproduce the experimental results.
A closer look at the settlement process and its dependence on the time signature and symmetry of the load reconfirmed that the settlement is a stick-slip process that occurs at the resonance frequencies of the combined system.

6

CONCLUSIONS

In this thesis the vibration-induced settlements that occur during the installation and dismount of a slip-joint connection used in offshore wind foundations were explored using experiments and numerical models. Vibration-induced settlement is obtained by vibrating one of the cones of the slip-joint. This novel method of achieving movement in a frictional joint may prove to be effective for the installation and dismount of a slip-joint, and it may also be useful during remedial manoeuvres of the slip-joint. The objective of this thesis was to investigate the potential of the use of vibrations during the installation and dismount of a slip-joint with slightly different cone angles.

In order to carry out a preliminary investigation into the dynamics of the slip-joint, a lumped model of the vibration-induced settlement of a slip-joint connection was proposed in Chapter 3. The goal of the model is to describe the dynamics of the slip-joint under the influence of vibrations in a simplified manner. The novelty of this model lies in the use of springs that represent the effective stiffness of the entire upper cone and the contact between the two cones, whose stiffnesses were derived using a thin-shell theory.
The Coulomb dry friction model was employed to describe the frictional contact between the cones. The model was used to simulate constant and harmonic loading cases for the installation of the joint. The results of the simulations indicate that the application of a constant load and the dropping of the upper cone from a certain height are both inadequate installation options when attempting to achieve a required settlement depth. The desired settlement depth can, however, be achieved by the application of a harmonic load to the top of the upper cone. The simulations in which vibrations were applied show that a successful installation can be achieved using various combinations of amplitudes and frequencies of the applied harmonic force. The vibration-induced settlement events show a stable equilibrium depth after a certain period, indicating that a controlled installation of a slip-joint is possible.

To prove that vibration-induced settlement is effective for installation and dismount purposes, an experimental campaign was initiated and executed. The campaign in-

cluded a series of installation and dismount tests with scaled slip-joint specimens, an experimental modal analysis, and high-precision measurements of the dimensions of the test specimens.
An experimental setup was designed in order to investigate the installation and dismount of a slip-joint using 1:10 scaled specimens of such a slip-joint. The procedure used for the installation experiment was to initially let the cone settle under its simulated self-weight. Subsequently, vibration was applied to the cones, and the frequency of vibration was increased in steps or by a constant increment. This procedure made it possible to identify the excitation frequencies that are effective for settlement and to study the settlement mechanism, along with the influence of the incremental increase of the excitation frequency on the settlement process and distance.

The test results demonstrate that the frequency of the applied vibration is key to the successful installation/dismount of a slip-joint. Only specific (resonance) frequencies of the applied vibration were found to be effective in inducing relative movement. It is observed that the application of a larger force in combination with a frequency that differs from these specific resonance frequencies did not lead to perceptible additional settlement. The observed settlements converged to certain equilibrium levels, indicating the possibility of a controlled installation.
The installation tests performed with the frequency of the applied vibration being increased incrementally demonstrated that, when the increment is too large, resonance does not have sufficient time to develop. As a consequence, smaller settlements will be achieved. The same tests also showed that the method of constantly increasing of the frequency leads to similar movements as the method that involved stepwise increases in frequency if a relatively small increment of the frequency is used.
The direction of the applied vibration, being either horizontal or vertical, led to similar settlement depths for the majority of the tests. This shows that the behaviour of the system under the influence of vibration is unaffected by the direction of the applied vibration. The wear that occurred on the contact surfaces as a result of repetitive testing did have an influence on the obtained settlement levels but not on the vibration-induced behaviour of the system.
The measured strain levels showed that the deformations that occurred as a result of the applied vibration and vibration-induced settlement remained well within the elastic regions. The strain measurements showed a non-uniform deformation around the circumference. This indicates a non-uniform contact and non-uniform stiffness along the circumference.
The use of two different vibratory devices, namely a set of eccentric motors or an electrodynamic shaker, enabled an investigation into the influence of the amplitude of the vibration and the effectiveness of frequencies outside the working spectrum of vibratory devices traditionally used for pile driving. It was shown that there are multiple effective frequencies at which settlement occurs. However, for both vibratory devices, the final settlement event was found to occur at the exact same effective frequency. Similar settlement levels were obtained for vibrations at equal frequencies with both vibratory devices. Remarkably, the vibrations that were applied with the electrodynamic shaker had amplitudes that were 250 times smaller than those applied by the eccentric

motor. This observation demonstrates the strong influence of the applied frequency on vibration-induced settlement. The amplitude of the applied vibration influences the settlement at resonance frequencies and can be used to control the final settlement depth of the system.
The experimental campaign demonstrated that the application of vibration is a controllable method for the installation and dismount of a slip-joint.
During several installation tests the frequency response of the combined system was measured before and after each settlement event. These measurements showed that the dynamic properties of the system change with increasing settlement depth. On the basis of this observation it was concluded that the stiffness of the combined system increases with increasing contact area and settlement.
The experiments also indicated that the specific frequency of 120 Hz is most relevant for vibration-induced settlement of the scaled slip-joint. In the majority of the installation tests, the final settlement event occurred while shaking at this frequency. The majority of the successful dismounts were also obtained by vibrating at this specific frequency.

In order to gain insight into the physics of the settlement behaviour and to understand why the above-mentioned frequency of 120 Hz leads to effective settlement, an experimental modal analysis was conducted on the installed scaled slip-joint. The results of this experiment confirm that, predominately, vibrations with frequencies close to one of the natural frequencies of the combined system are effective in inducing settlement. The modal shape around 120 Hz, which is the most effective for installation and dismount purposes, is characterized by the circumferential mode m=2 and longitudinal mode n=1 of a conical shell.

The dimensions of one set of cones were measured using a laser setup. The measured dimensions of the specimens gave an impression of the manufacturing tolerances, the initial contact, and the development of the contact with increasing settlement. The measurements clearly showed that the slip-joint specimens were manufactured with undesirably high tolerances. The contact developed at two distinct areas and then expanded in the circumferential direction with increasing settlement levels. On the basis of these measurements, it can be observed that the contact was non-uniform, which provides an explanation for the non-uniformity of the measured strains along the circumference that were observed in the installation tests.

Based on the experimental campaign it can be concluded that the use of vibration-induced settlement is effective for the execution of installation or dismount of a slip-joint connection. Furthermore, it was observed that the frequency of the applied vibration is key to a successful settlement process. The settlement levels are only marginally sensitive to vibration amplitudes. Of all of the methods considered, the slow ramping up of frequency shows the highest potential to be used in practice for installation and dismount purposes, as it requires minimal instructions and knowledge of the dynamic properties of the system.

In Chapter 5, the behaviour of a slip-joint under influence of vibrations was modelled

using a finite element model which was set up with the aim of reproducing the experiments qualitatively. Using this model, the installation and dismount procedure used in the experimental campaign were simulated.
The results of the numerical model indicated that it is able to reproduce the observed settlement process. Furthermore, the cones' settlement events achieved as a result of the applied vibration can occur in one of the following two manners. The first is that it occurs when the amplitude of the force is increased substantially. The second is by selecting specific frequencies of the applied vibrations in combination with smaller amplitudes. For amplitudes below a critical value, settlement events occur only when the applied vibration causes resonance of the combined system. This specific dependence on the frequency of vibration in the settlement behaviour of the model was also observed in the experiments. The model is thus able to reproduce the frequency dependence of vibration-induced settlement for the installation simulations. The mode of the FE model that was found to be effective in obtaining vibration induced settlement corresponds to the combination of the circumferential mode m=2 and a longitudinal shape of n=1. This mode shape matches the most effective mode shape that was identified in the experimental campaign.
The model is able to simulate a successful dismount with applied loads and vibration that correspond to the initial installation simulation. In the simulations in which a successful dismount was obtained, an axial pulling force that was similar to the simulated self-weight of the upper cone and a vibrational frequency that corresponded to one of the natural frequencies of the combined system was applied. The model was not able to produce a successful dismount for larger applied axial forces without the application of a vibration corresponding to one specific natural frequency. This final result is in line with the observations of the experimental dismount. It can be concluded that the finite element model qualitatively captures the vibration-induced behaviour of the slip-joint experiments in both installation and dismount simulations.

A parametric study was conducted to investigate the uncertainties associated with the finite element model. This study indicates that the experimental settlement level achieved as a result of the simulated self-weight can be approximated by utilizing a low friction coefficient in the simulations. The settlement level that occurred as a result of the application of the vibrations that were found to be effective during the experiments was not matched by the finite element model. This difference can be related to the discrepancy between the perfect contact along the circumference of the FE model and the imperfect contact of the scaled specimens. By choosing even lower friction coefficients the reproduction of the experiments settlement levels will be more accurate.
The simulations that featured different values for the decay function of the friction coefficient were found to be highly sensitive. The decay function describes decay as a function of the relative velocity for the value of the friction from the static to dynamic value. A low decay function, indicating a 'slow' decay, influences the model results such that a settlement event is observed at most frequencies, and the frequency dependence of the settlement behaviour is lost.
A reduction of element size slightly influences the results obtained during the axial loading phase. The behaviour of the model under vibration remains unchanged.

The results of the finite element model were shown to be sensitive to the choice of damping. Great care should be taken in the selection of damping type, as the results can be influenced such that no settlement is obtained while vibration is applied.
Based on the performed parametric study, it can be concluded that it is a challenge to select the correct values for the parameters *a priori* when attempting to reproduce the experimental results both quantitatively and qualitatively. The quantitative prediction of vibration-induced settlement using the current model is therefore not recommended. Based on the simulation results, it can be concluded that the finite element model is able to capture the stick-slip behaviour that occurs during settlement events. Moreover, the model is capable of capturing the key behaviour of the slip-joint under the influence of vibrations, i.e. the fact that only certain natural frequencies can effectively induce a relative movement for small amplitudes of the dynamic force. The model confirms the experimental observation that, if the frequency of the applied vibration does not correspond to a natural frequency, larger amplitudes are required to achieve settlement.

In this thesis, it is proven that, under the action of a vibratory source, settlement events between the cones of a slip-joint can be achieved. With the use of experiments and numerical modelling, it is demonstrated that excitation at frequencies equal or close to natural frequencies of the slip-joint is key to the successful installation or dismount of a slip-joint. The settlement behaviour induced by vibrations is observed to be a stick-slip process that finally stabilizes at a level of equilibrium. The use of the slip-joint can extend the applicability of the monopile foundation for offshore wind turbines to deeper waters and larger turbines. The results obtained in this thesis are expected to enable successful vibration-assisted installations of slip-joints in full-scale.

BIBLIOGRAPHY

4c offshore. Veja mate wind farm details. Online, 2016. URL www.4coffshore.com/windfarms/greater-gabbard-united-kingdom-uk05.html.

Analog Devices. Three-axis accelerometer evaluation board (eval-adxl326z). Online, 2013. URL www.analog.com.

Armstrong-Hélouvry, B. *Control of Machines with Friction*, chapter 1, page 36. Springer Science Business Media, 1991. doi: 10.1007/978-1-4615-3972-8.

Barber, J. R. *Elasticity*, volume 172, chapter The Reciprocal Theorem, pages 517–528. Springer Netherlands, 2010. doi: 10.1007/978-90-481-3809-8_34.

Barrett, R. T. Nasa reference publication 1228. Technical report, NASA, March 1990.

Blau, P. J. The significance and use of the friction coefficient. *Tribology International*, 34 (9):585–591, sep 2001. doi: 10.1016/s0301-679x(01)00050-0.

Bo, L. C. and Pavelescu, D. The friction-speed relation and its influence on the critical velocity of stick-slip motion. *Wear*, 82(3):277–289, nov 1982. doi: 10.1016/0043-1648(82)90223-X.

Brincker, R., Zhang, L., and Andersen, P. Modal identification of output-only systems using frequency domain decomposition. *Smart Mater. Struct.*, 10(3):441–445, jun 2001. doi: 10.1088/0964-1726/10/3/303.

Bruel & Kjaer. Technical review - new instrumentation for vibration testing. Online, 1971. URL www.bksv.com/doc/technicalreview1971-2.pdf. page 36-40.

Cai, C., Zheng, H., Khan, M., and Hung, K. Modeling of material damping properties in ansys. *ANSYS 2002 Users Conference and Exhibition*, 2002.

Campbell, W. E. Studies in boundary lubrication. *Trans. A.S.M.E.*, 61(7):633–641, 1939.

CAPE Holland. Product brochure vibratory device model cv-230. Online, 2015. URL http://www.cape-holland.com. accessed 2016.

Cook, R., Malkus, D., Plesha, M., and Witt, R. *Concepts and applications of finite element analysis*. John Wiley and Sons, fourth edition, 2002. pp.32-36.

de Vries, E. Offshore monopile failure - a solution may be in sight. *Wind Power Montly magazine*, 2010. URL https://tinyurl.com/y9ovrjyx.

de Vries, W. and Krolis, V. Effects of deep water on monopile support structures for offshore wind turbines. In *Conference proceedings EWEC*, 2007.

Den Hartog, J. Forced vibrations with combined viscous and coulomb damping. *Philosophical Magazine*, 9(59):801–817, 1930.

Diepeveen, N. *On Fluid Power Transmission*. Phd thesis, Delft university of technology, 2013.

DNV. Joint industry project summary report from the jip on the capacity of grouted connections in offshore wind turbine structures. Technical report REPORT NO. 2010-1053 REVISION NO. 05, Det Norske Veritas AS, 2011a.

DNV. Design of offshore wind turbine structures. Technical report DNV-OS-J101, Det Norske Veritas AS, January 2011b.

Euro-bearings LTD. Online, 2013. URL `www.euro-bearings.com`.

Gaylord, E. W. and Shu, H. Coefficients of static friction under statically and dynamically applied loads. *Wear*, 4(5):401–412, sep 1961. doi: 10.1016/0043-1648(61)90008-4.

Godfrey, D. Vibration reduces metal to metal contact and causes an apparent reduction in friction. *A S L E Transactions*, 10(2):183–192, 1967. doi: 10.1080/05698196708972178.

Ho, A., Mbistrovam, A., and Corbetta, G. The european offshore wind industry - key trends and statistics 2015. Technical report, The European Wind Energy Association, 2016.

Hong, H. and Lui, C. Coulomb friction oscillator: Modelling and responses to harmonic loads and base excitations. *Journal of Sound and Vibrations*, 229(5):1171–1192, 2000.

Invertek drives. Invertek optidrive p2 overview page. Online, 2015. URL `www.invertekdrives.com/variable-speed-drives/optidrive-p2/`.

Jonkman, J. and Musial, W. Offshore code comparison collaboration (oc3) for iea task 23 offshore wind technology and deployment. techreport NREL/TP-5000-48191, National Renewable Energy Laboratory, 2010.

Kaldunski, P. Plane anisotropy parameters identification based on barlat's model. In *Proceedings of the 3rd Polish Congress of Mechanics (PCM) and 21st International Conference on Computer Methods in Mechanics (CMM), Gdansk, Poland, 8-11 September 2015*, pages 275–278. Informa UK Limited, apr 2016. doi: 10.1201/b20057-60.

Kutz, M., editor. *Eshbach's Handbook of Engineering Fundamentals*. Wiley-Blackwell, jan 2009. doi: 10.1002/9780470432754. p. 4.52.

Lotsberg, I., Serednicki, A., Bertnes, H., and Lervik, A. Design of grouted connections for monopile offshore structures - results from two joint industry projects. *Stahlbau*, 81, 2012.

Mac Donald, B. *Practical Stress Analysis with Finite Elements*. Glasnevin, 2007. ISBN 9780955578106. doi: 10.1016/0043-1648(82)90223-X. p.147.

Marks, L. *Standard Handbook for Mechanical Engineers*. McGraw-Hill, 1967. doi: 10.1002/aic.690140103.

Mueller-BBM. The measurement device:pak mkii. Online, 2013. URL http://www.muellerbbm-vas.com/products/data-acquisition/frontends.

Nikken, L. Jacob drill chuck. Online, 2015. URL https://tinyurl.com/y9pf6ca2.

Nolle, H. and Richardson, R. Static friction coefficients for mechanical and structural joints. *Wear*, 28(1):1–13, apr 1974. doi: 10.1016/0043-1648(74)90097-0.

NoordzeeWind. Operation report 2009. techreport OWEZ R 000 20101112 operations 2009, NoordzeeWind, 2010.

Nordlund, E. and Lundberg, B. Slip and energy dissipation in conical friction joints loaded by impact waves. *International Journal of Impact Engineering*, 4(2):127–144, 1986.

Oberg, E. and Jones, F. *Machinery's Handbook (18th Edition) A Reference Book for the Mechanical Engineer, Draftsman, Toolmaker and Machinist*. Industrial Press, New York, 18 edition, 1969.

Orlowitz, E., Andersen, P., and Brandt, A. Comparison of simultaneous and multi-setup measurement strategies in operational modal analysis. In *IOMAC'15 6th international Operational Modal Analysis Conference*, 2015.

PCB Piezotronics. Model 086d05 modally tuned impulse hammer w/force sensor and tips 0 to 5k lbf, 1 installation and operating manual. Online, 2007a.

PCB Piezotronics. Product information on accelerometer model: 356b18. Online, 2007b. URL http://www.pcb.com/products.aspx?m=356B18.

PCB Piezotronics. Product information on impulse hammer model: 086d05. Online, 2007c.

Popp, K. Non-smooth mechanical systems - an overview. *Forschung im Ingenieurwesen*, 64:223–229, 1998.

Rabinowicz, E. Stick and slip. *Scientific American*, 195(5):109–118, 1956. URL http://www.nature.com/scientificamerican/journal/v194/n5/pdf/scientificamerican0556-109.pdf.

Rabinowicz, E. The intrinsic variables affecting the stick-slip process. *Proceedings of the Physical Society*, 71(4):668–675, apr 1958. doi: 10.1088/0370-1328/71/4/316. URL http://dx.doi.org/10.1088/0370-1328/71/4/316.

Richardson, M.H. Is it a mode shape, or an operating deflection shape? *Sound & Vibration Magazine*, 30th Anniversary, March 1997.

RIFTEK Sensors & Instruments. Laser triangulation sensors rf603 series. Online, 2012.

Ringspann. Shaft-hub-connections edition 2010/2011. Online, 2011. URL www.ringspann.com.

SD Tools. Structural dynamics toolbox- overview. Online, 2008. URL www.sdtools.com/sdt/.

SD Tools. Structural dynamics toolbox & femlink user guide. Online, March 2016.

Segeren, M. and Diepeveen, N. Influence of the rotor nacelle assembly mass on the design of monopile foundations. *Heron*, 59(1):17–36, 2015.

Segeren, M. and Hintz, U. Private email with Uwe Hintz. R&D engineer at Mann from 1983-1993, 2015.

Segeren, M., Lourens, E., Tsouvalas, A., and T.J.J. van der Zee. Investigation of a slip joint connection between the monopile and the tower of an offshore wind turbine. *IET Renewable Power Generation*, 8(4):p. 422 – 432, 2014.

Seidel, M. Feasibility of monopiles for large offshore wind turbines. In *Conference Proceedings DEWEK*, 2010.

Shaumann, P. and Böker, C. Can jackets and tripods compete with monopiles? In *Conference proceedings EWEA Offshore Wind*, 2005.

Sieros, G., Chaviaropoulos, P., J.D.Sørensen, Bulder, B., and Jamieson, P. Upscaling wind turbines: Theoretical and practical aspects and their impact on cost of energy. *Wind energy journal*, 15:3–17, 2012.

Soedel, W. *Vibrations of Shells and Plates*. Marcel Dekker, third edition, 2004. (page 55-56).

Stockinger, K. *Die Hochspannungsfreileitung*. Verlag von Julius Springer, 1931. (Page 63).

Symmons, G. -. Phd thesis, University of Manchester, 1969.

Tullis, T. E. *Friction and Faulting*. Springer Nature, 1987. doi: 10.1007/978-3-0348-6601-9.

Valmont. Valmont light pole products brochure. Online, 2015. URL http://www.valmont.com.

van der Tempel, J. and Schipholt, B. L. The slip-joint connection, alternative connection between pile and tower. techreport DOWEC report-F1W2-JvdT-03-093/01-P, Delft University of Technology, 2003. Dutch Offshore Wind Energy Converter project 2003.

Wacker Neuson. Eccentric motor ar 53, product brochure. Online, 2015. URL www.wackerneuson.nl.

Watkins, J. D. and Clary, R. R. Vibrational characteristics of some thin-walled cylindrical and conical frustum shells. Technical report, Langley Research Center, 1965. URL https://ntrs.nasa.gov/archive/nasa/casi.ntrs.nasa.gov/19650010314.pdf.

wind-turbine-models.com. Webpage with one of the mann turbine turbines at herrendeich - nordstrand, germany. Online, 2014. URL https://tinyurl.com/ycxjoceu.

A

EQUATIONS OF MOTION OF A CIRCULAR CONICAL SHELL

This appendix summarizes the relevant equations of Chapter 3.2 of the book by Soedel (2004) that are used for the derivation of the effective stiffnesses of a conical shell. Equations (A.1) to (A.3) (3.2.9 until 3.2.11 in Soedel (2004)) give the equations of static equilibrium of a conical shell for the tangential direction U_x, circumferential direction U_θ and normal direction U_3 for the case shown in figure A.1. Where μ in the original text is replaced by ν representing the Poission's ratio.

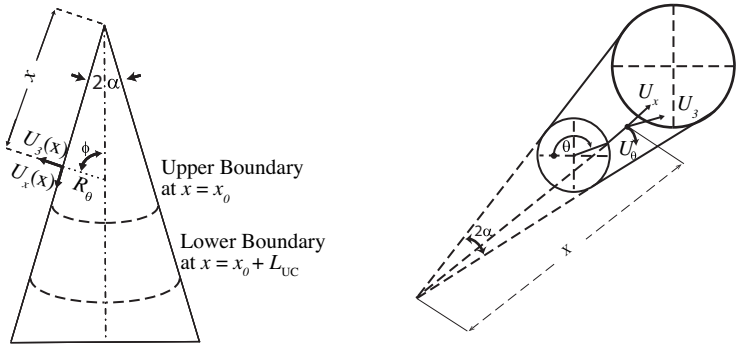

Figure A.1: Coordinate definitions for a conical shell with cone angle α, the displacement in tangential direction U_x, in circumferential direction U_θ and in normal direction U_3.

$$N_{xx,x} + \frac{1}{x\sin(\alpha)} N_{\theta x,\theta} + \frac{1}{x}(N_{xx} - N_{\theta\theta}) + q_x = 0 \tag{A.1}$$

$$N_{x\theta,x} + \frac{2}{x} N_{\theta x} + \frac{1}{x\sin(\alpha)} N_{\theta\theta,\theta} + \frac{1}{x\tan(\alpha)}(Q_{\theta 3}) + q_\theta = 0 \tag{A.2}$$

$$Q_{x3,x} + \frac{1}{x}Q_{x3} + \frac{1}{x\sin(\alpha)}Q_{\theta 3,\theta} - \frac{1}{x\tan(\alpha)}N_{\theta\theta} + q_3 = 0 \tag{A.3}$$

in which q are distributed load components (per unit length) in the direction of x, θ and 3. The shear forces that are normal to the shell surface, Q_{x3} and $Q_{\theta 3}$ are:

$$Q_{x3} = M_{xx,x} + \frac{M_{xx}}{x} + \frac{1}{x\sin(\alpha)}M_{\theta x,\theta} - \frac{M_{\theta\theta}}{x} \tag{A.4}$$

$$Q_{\theta 3} = M_{x\theta,x} + \frac{2M_{\theta x}}{x} + \frac{1}{x\sin(\alpha)}M_{\theta\theta,\theta} \tag{A.5}$$

The relation between the forces, moments and strains are given by equations A.6 to A.11:

$$N_{xx} = K(\epsilon^0_{xx} + \nu\epsilon^0_{\theta\theta}) \tag{A.6}$$

$$N_{\theta\theta} = K(\epsilon^0_{\theta\theta} + \nu\epsilon^0_{xx}) \tag{A.7}$$

$$N_{x\theta} = N_{\theta x} = \frac{K(1-\nu)}{2}\epsilon^0_{x\theta} \tag{A.8}$$

$$M_{xx} = D(k_{xx} + \nu k_{\theta\theta}) \tag{A.9}$$

$$M_{\theta\theta} = D(k_{\theta\theta} + \nu k_{xx}) \tag{A.10}$$

$$M_{x\theta} = M_{\theta x} = \frac{D(1-\nu)}{2}k_{x\theta} \tag{A.11}$$

in which K represents the membrane stiffness and D the bending stiffness:

$$K = \frac{Eh}{1-\nu^2} \tag{A.12}$$

$$D = \frac{Eh^3}{12(1-\nu^2)} \tag{A.13}$$

The relation between the strains and the displacements are given by equations (A.14) to (A.19):

$$\epsilon^0_{xx} = U_{x,x} \tag{A.14}$$

$$\epsilon^0_{\theta\theta} = \frac{1}{x\sin(\alpha)} U_{\theta,\theta} + \frac{1}{x} U_x + \frac{1}{x\tan(\alpha)} U_3 \tag{A.15}$$

$$\epsilon^0_{x\theta} = U_{\theta,x} - \frac{1}{x} U_\theta + \frac{1}{x\sin(\alpha)} U_{x,\theta} \tag{A.16}$$

The bending strains k are:

$$k_{xx} = \beta_{x,x} \tag{A.17}$$

$$k_{\theta\theta} = \frac{1}{x\sin(\alpha)} \beta_{\theta,\theta} + \frac{1}{x} \beta_x \tag{A.18}$$

$$k_{x\theta} = x\left(\frac{\beta_\theta}{x}\right)_{,x} + \frac{1}{x\sin(\alpha)} \beta_{x,\theta} \tag{A.19}$$

where β_x and β_θ are angles that influence the linear (for thin shells) variation through the shell thickness. These angles are given by equation (A.20) and (A.21) for a conical shell:

$$\beta_x = -U_{3,x} \tag{A.20}$$

$$\beta_\theta = \frac{1}{x\tan(\alpha)} U_\theta - \frac{1}{x\sin(\alpha)} U_{3,\theta} \tag{A.21}$$

B

RESULTS OF THE EXPERIMENTAL INVESTIGATION INTO VIBRATION-INDUCED MOVEMENT OF A SLIP-JOINT

B.1. INTRODUCTION AND SUMMARY OF THE EXPERIMENTAL RESULTS

In this appendix, all of the settlement and load measurements of the installation and dismount tests performed at Civil Engineering Faculty's Stevinlab are presented. A summary of the results is first provided in order to give an overview of the details and results of the experiments. The experiments are divided into batches of tests; an overview of the batches is given in Table B.1. Descriptions of the individual experiments are given in Tables B.2, B.3, B.4.

Batch 1 concerned the initial installation and dismounting experiments conducted with cone set 1. These experiments demonstrated that vibrations are effective in terms of creating movement in a slip-joint when installing or dismounting it. It was observed that the applied vibrations were only effective in terms of settlement between the cones at specific frequencies. It was also found that a larger applied force does not necessary lead to larger settlements. Several attempts were required to successfully dismount the cones for the first time. A force of -40 kN and at 85 Hz was successful. After these tests an adjustment to the experimental setup was performed: ball bearings underneath the hydraulic jacks were added to allow the cones to self-align.

The experiments of batch 2 reproduced the observation that the cones of the slip-joint, after the introduction of self-weight, are able to move relative to each other only while vibration at certain frequencies was applied. The presence of the ball bearing changes

the effective frequencies slightly. The new results show, that at the effective frequencies, the settlement/movement follows stick-slip cycles.

The axial capacity was tested with a maximum axial force test. This test simulated the axial load of a fully installed wind turbine tower and rotor- nacelle assembly on top of the slip-joint. No additional settlement was observed, which demonstrates that installing the slip-joint with the assistance of vibrations provides the joint with sufficient axial capacity to bear the turbine weight. Another test in this batch showed that, if a large constant increment of the frequency of vibration is used, the final settlement depth may not be reached. Settlement events that occur as a result of applied vibration thus need time to develop.

The experiments of batch 3 were carried out with slip-joint set 2. The experiments showed that, with a large increment of the frequency of vibration, the effective frequency can be overshot, resulting in settlements smaller than what could be achieved. With a smaller increment, this effect was not observed. The frequencies that were found to be effective differ slightly between the two sets, which is attributed to their minimal differences in the dimensions.

The experiments in batch 4 and 5 concentrated on capturing the evolution of the frequency response of the slip-joint from initial situation until the final settlement. To track the changes in the response of the joint, hammer impact experiments were conducted after each settlement event.

The experiments in batch 6 investigated the influence of the amplitude of the vibration applied on the settlement behaviour. This was done by replacing the eccentric motors with an electrodynamic shaker. Despite the smaller amplitudes of the vibration, the same settlement behaviour as in the experiments which featured the eccentric motors was observed. Other tests in this batch indicated that the amplitude of the applied vibration has a limited influence on the final settlement depth. Changing the direction of the applied vibratory load did not change the behaviour of the settlement, while the wear of the contact surfaces of the cones caused reduction in settlement depth under simulated self-weight without vibrations. The axial force required to obtain settlement events increased during these experiments, and as a result, the settlement depth obtained cannot be compared with the results obtained in batches 3, 4, and 5.

The results of the experiments in batch 7 were obtained with slip-joint set 1. The results indicated that several effective frequencies can be used to obtain similar settlement depths and that changing the frequency after the final settlement depth is achieved does not result in additional settlement. The final settlement depth obtained was generally slightly shallower than that obtained in the experiments that featured eccentric motors for equal axial forces. For dismounting, a frequency of approximately 120 Hz was found to be effective in the majority of the experiments executed using set 1.

The results of the experiments in batch 8 were obtained using slip-joint set 1 and the

Table B.1: Overview of the experimental batches.

Batch	Test nr.	Goals
1.	1-7	First installation and dismount experiments with cone set 1
2.	8-11	Repetition of tests / Test max. axial capacity / Test effectiveness of a lin. increase of frequency
3.	12-28	Repetition of tests with set 2 of cones / Investigate the effect of time in the settlement process
4.	29-31	Repetition of tests / Investigate changes in response of the system by increasing settlement depths
5.	32-42	Repetition of tests / Investigate changes in response of the system by increasing settlement depths
6.	43-56	Investigate the influence of the amplitude of the vibration in settlement behaviour of the cone set 2
7.	57-75	Repetition of tests / Investigate the influence of the vibration amplitude in behaviour of the cone set 1
8.	76-84	Repetition of tests to confirm settlement behaviour of the cone set 1

eccentric motors. The experiments were intended to reproduce the results obtained in batch 1 in order to compare them with the results of the electric shaker of batch 7 and the result of the eccentric motor tests obtained with slip-joint set 2 in batch 3. The maximum settlement achieved in these tests was equal to that observed in the tests of batch 7. This means that an electric shaker with small force amplitudes of the vibration is capable of producing similar settlement depth as the eccentric motor actuator that delivers vibrations of up to 200 times larger force amplitudes. This observation indicates that the settlement events that occur as a result of the small vibrations applied at specific frequencies can be the result of resonance.

In the following sections the results of the majority of the individual tests are discussed in greater detail.

Table B.2: Overview of the experimental batches

Test Matrix **number of test**	**Type of test**	**Set**	**Vibratory device**	**Frequency increase**	**Axial force[kN]**	**Result**
1	Install	1	Ecc. Motor	Step wise	10	Settles 13.4 mm
2	Dismount	1	Ecc. Motor	Linear incr. 0-200 Hz in 30s	-6	no dismount
3	Dismount	1	Ecc. Motor	Linear incr. 0-100 Hz in 15s	-10	no dismount
4	Dismount	1	Ecc. Motor	Linear incr. 0-100 Hz in 15s	-10 to -20	no dismount
5	Dismount	1	Ecc. Motor	Linear incr. 0-110 Hz in 90s	-20	no dismount
6	Dismount	1	Ecc. Motor	Linear incr. 0-100 Hz in 15s	-20 to -30	no dismount
7	Dismount	1	Ecc. Motor	Step wise up to 85 Hz	-40	Successful dismount
				Ball bearings are added to the set up		
8-1	Install	1	Ecc. Motor	Step wise up to 115 Hz	10	9 mm of settlement
8-2	Install	1	Ecc. Motor	Step wise up to from 115-200 Hz	10	3 mm of settlement
9	Max. axial force	1	none	none	10 to 60	No additional settlement
10	Dismount	1	Ecc. Motor	Step wise up to 128 Hz	-30	Successful dismount
11	Install	1	Ecc. Motor	From 0-128 Hz in 13 sec	10	Full settlement of 11 mm is not reached in the 13s.
12	Install	2	Ecc. Motor	Slow step wise up to 200 Hz	10	Settles at 30, 54, 86, 110, 115, 126 Hz total 14 mm
13	Dismount	2	Ecc. Motor	Slow step wise up to 128 Hz	-30	Successful dismount
14	Install	2	Ecc. Motor	Slow step wise up to 200 Hz	10	Settles at 30, 51, 53, 90, 108, 115, 122, 126 Hz total 11.5 mm
15	Dismount	2	Ecc. Motor	Slow step wise up to 127.5 Hz	-30	Successful dismount
16	Install	2	Ecc. Motor	Linear incr. 0-130 Hz in 15 s	10	Add. Settl. when freq is lowered to 127 Hz;total 10 mm
17	Dismount	2	Ecc. Motor	Linear incr. 0 to 126 Hz in 13 s	-30	Successful dismount
18	Install	2	Ecc. Motor	Linear incr. 0-126 Hz in 13 s	10	Total 13 mm settlement
19	Dismount	2	Ecc. Motor	Linear incr. 0 to 124 Hz in 13 s	-30	at 125 Hz it loosens
20	Install	2	Ecc. Motor	Linear incr. 0-126 Hz in 13s	10	Total 9.8 mm settlement
21	Dismount	2	Ecc. Motor	Linear incr. 0 to 127 Hz in 13 s	0 to -30	at -30 kN it dismount at the frequency of 126 Hz
22	Install	2	Ecc. Motor	Slow step wise up to 200 Hz	10	At 30, 50, 52, 83, 105, 120, 122 Hz total 11.4 mm
23	Dismount	2	Ecc. Motor	Linear incr. 0 to 125 Hz	0 to -30 to -35	at -35 kN dismounts at 125 Hz
24	Install	2	Ecc. Motor	Slow step wise up to 200 Hz	10	Settles at 50, 52, 83, 105, 115, 120 Hz in total 10.7 mm
25	Dismount	2	Ecc. Motor	Linear incr. 0 to 125 in 13 s	0 to -30	slowly loosens
26	Install	2	Ecc. Motor	Linear incr. 0-125 Hz in 26s	10	In total 12.5 mm settlement
27	Dismount	2	Ecc. Motor	Linear incr. 0 to 125 in 60 s	-20	slowly loosens at 115 Hz
28	Install	2	Ecc. Motor	Linear incr. 0 to 125 in 60 s	10	Settlement at 50, 83, 92, 105 Hz and 11.3 mm
29	Dismount	2	Ecc. Motor	Linear incr. 0 to 120 in 60 s	-20	comes loose at 110 Hz
30-1	hammer impact	2	-	-		8 impact tests after settlement under self-weight
30-2	Install	2	Ecc. Motor	Stepwise	10	at 29 Hz 1 mm
30-3	hammer impact	2				8 impact tests after 1st settlement event
30-4	Install	2	Ecc. Motor	Stepwise	10	at 50, 52 Hz
30-5	hammer impact	2				8 impact tests after 2nd settlement event
30-6	Install	2	Ecc. Motor	Stepwise	10	at 94, 98 Hz, but in stick-slip cycles
30-7	hammer impact	2				8 impact tests after 3rd settlement event
30-8	Install	2	Ecc. Motor	Stepwise	10	at 105 , Hz, 2.5 mm
30-9	hammer impact	2				8 impact tests after 4rd settlement event
30-10	Install	2	Ecc. Motor	Stepwise	10	total settlement of test 30= 11.2 mm
31	Dismount	2	Ecc. Motor	Linear incr. 0 to 120 in 60 s	-20	comes loose at 110 Hz

Table B.3: Overview of the experimental batches

Test Matrix number of test	Type of test	Set	Vibratory device	Frequency increase	Axial force[kN]	Result
32	Install	2	Ecc. Motor	ramp up to 118 Hz , stepwise to 130		settlement 10 mm
33-1	Dismount	2	Ecc. Motor	Linear incr. 0 to 118	-18	does not dismount
33-2	Dismount	2	Ecc. Motor	Linear incr. 0 to 118 to 128 to 116 Hz	-18 to -22	does dismount at 120 Hz
34-1 to 34-15	Install	2	Ecc. Motor	Step wise	10	Mult. files of the settlement instances
35	Dismount	2	Ecc. Motor	Linear incr. 0 to 118 Hz	-20	does dismount at 110HZ
36-1	hammer impact	2		Prior to installation	0	
36-2	Install	2	-	own weight	10	no measurements
36-3	hammer impact	2		After settlement under own weight		8 impact tests
36-4 to 36-6	Install	2	Ecc. Motor	Stepwise	10	at 20, 29.3 Hz; 0.5 mm total settlement
36-7	hammer impact	2				8 impact tests
36-8-36-10	Install	2	Ecc. Motor	Stepwise	10	at 49, 51.4, 53 Hz; 1.5 mm settlement
36-11	hammer impact	2				8 impact tests
36-12	Install	2	Ecc. Motor	Stepwise	10	at 83 Hz, 0.7 mm
36-13	hammer impact	2				8 impact tests
36-14	Install	2	Ecc. Motor	Stepwise	10	at 103 and 105 Hz; 4.3 mm settlement
36-15	hammer impact	2				8 impact tests
36-16	Install	2	Ecc. Motor	Stepwise	10	at 118, 135, 193 Hz; 7.55 mm settlement
36-15	hammer impact	2				8 impact tests
37	Dismount	2	Ecc. Motor		-20	1 mm at 110 Hz but does not dismount.
38	Dismount	2	Ecc. Motor		-24	loosens 0.1 mm
39	Dismount	2	Ecc. Motor		-36	it dismounts but no results are measured
40	Install	2		settlement 0, 10 KN	0, 10	at 10 kN it settles for .5 mm
41	Install	2	Ecc. Motor	ramp up to 123 Hz	10	at 30, 50, 80, 95, 103, 119 Hz in total 12.7 mm
42	Dismount	2	Ecc. Motor	Linear incr. 0 to 118	from +10 to -30	does dismount at -20 kN and at 118 Hz
43	Install	2		settlement 0, 10 KN	0, 10	
44	Install	2	Shaker at low pos.	Sweep 20-400 Hz in 180 s	18	Total settlement 3 mm
45	Install	2	Shaker at low pos.	Sweep 20-800 Hz in 600 s	20	Total settlement 3.9 mm
46	Install	2	Shaker at low pos.	Sweep 20-250 Hz in 230 s	20	30% of max voltage shaker
47	Install	2	Shaker at low pos.	Sweep 20-250 Hz in 230 s	20	60% of max voltage shaker
48	Install	2	Shaker at low pos.	Sweep 20-250 Hz in 230 s	20	90% of max voltage shaker
49	Install	2	Shaker at low pos.	Sweep 20-250 Hz in 230 s	24	30% of max voltage shaker
50	Install	2	Shaker at low pos.	Sweep 20-250 Hz in 230 s	24	60% of max voltage shaker, 1.6 mm settlement
51	Install	2	Shaker at low pos.	Sweep 20-250 Hz in 230 s	24	90% of max voltage shaker, 0.6 mm settlement
52	Dismount	2	Shaker at low pos.	Sweep 230-250 Hz	-27	Releases at 249.5 Hz
53	Install	2	Shaker at low pos.	249 Hz, Ampl. stepwise incr.	28	Total settlement 10 mm
54	Dismount	2	Shaker at high pos.	249 Hz	-28 to -30	Dismounts at -30 kN
55	Install	2	Shaker at high pos.	From 20-300 Hz in 280 s; 300 to 249.5 Hz	32	90% of max voltage shaker; 1.5 mm settlement
56	Install	2	Shaker at high pos.	249 Hz, Ampl. stepwise incr.	28	Settlement 6 mm

Table B.4: Overview of the experimental batches

Test Matrix **number of test**	**Type of test**	**Set**	**Vibratory device**	**Frequency increase**	**Axial force[kN]**	**Result**
57	Dismount	1	Shaker at high pos.	Sweep from 20-300 Hz with 1 Hz/s	24 to -34	Initially no dismount; Dismounts at 269 Hz.
58	Install	1	Shaker at high pos.	Stepwise from 20-400 Hz	10	at 77, 105, 113.5, 116, 118, 120 Hz, 8.5 mm
59	Dismount	1	Shaker at high pos.	Stepwise from 0 to 119 Hz	-30	Dismounts at 119 Hz
60	Install	1	Shaker at high pos.	Stepwise from 119 to 200 Hz	10	at 119HZ and 123; 7.1 mm
61	Install	1	Shaker at low pos.	20-320 Hz with 1 Hz/s	10	at 240 Hz micrometer settlement
62	Dismount	1	Shaker at low pos.	At 119 Hz	-30	Dismounts at 119 Hz
63	Install	1	Shaker at low pos.	Step wise from 0 to 300 Hz	10	110, 115, 117, 118, 119 Hz, 4.7 mm settlement
64	Dismount	1	Shaker at low pos.	Shaking with 119 Hz	-24	Dismounts at 119 Hz
65	Install	1	Shaker at low pos.	Shaking with 120 Hz, Ampl. stepwise incr.	10	7 mm total settlement
66	Sweep	1	Shaker at low pos.	20-300 Hz with 1 Hz/s		Response peaks at 123, 151, 261, 275 Hz
67	Dismount	1	Shaker at low pos.	Shaking with 120 Hz	-24	Dismounts at 120 Hz
68	Install	1	Shaker at low pos.	Stepwise from 0 to 300 Hz	10	at 113, 118, 119 Hz; 3 mm settlement
69	Dismount	1	Shaker at low pos.	Shaking with 120 Hz	-20	Dismounts at 120 Hz
70	Install	1	Shaker at low pos.	Shaking with 120 Hz	10	Settlement 4.6 mm
71	Sweep	1	Shaker at high pos.	Sweep from 20-300 Hz with 1 Hz/s		response peaks at 123, 151, 261, 275 Hz
72	Dismount	1	Shaker at high pos.	Shaking with 120 Hz	-30	Dismounts at 120 Hz
73	Install	1	Shaker at high pos.	Various frequencies	10	77, 107, 112, , 115, 116, 117, 118, 119 Hz; 10 mm settling
74	Dismount	1	Shaker at high pos.	Shaking with 120 Hz	-20 to -40	Dismounts at 120 Hz
75	Install	1	Shaker at high pos.	Shaking with 260 Hz and then to 120 Hz	10	Settlement 6 mm
76	Dismount	1	Ecc. motor	Linear incr. 0 to 118 Hz	-20 to -30	Dismounts at 121 Hz
77	Install	1	only axial forces	from 0 to 10 kN in 20 s	10	Shows stick slip behaviour
78	Install	1	Ecc. motor	Step wise incr. up to from 0-200 Hz	10	at 27, 78, 110, 115, 120 Hz settlement of 10 mm
79	Dismount	1	Ecc. motor	Linear incr. 0 to 118 Hz	-24	Dismounts at 120 Hz, loosens at 113 Hz
80	Install	1	Ecc. motor	Stepwise increase (5 files)	10	settlement of 10 mm
81	Dismount	1	Ecc. motor	Linear incr. 0 to 118 Hz	-22	Dismounts at 120 Hz, loosens at 120 Hz
82	Install	1	Ecc. motor	Slow ramp up to 120 Hz in 60s	10	total settlement 7.9 mm
83	Dismount	1	Ecc. motor	Linear incr. 0 to 118 Hz	-22	Dismounts at 120 Hz, loosens at 119 Hz
84	Install	1	Ecc. motor	Slow ramp up to 120 Hz in 180s	10	at 25, 33, 65, 78, 89, 107-120 Hz; settlement 8.5 mm

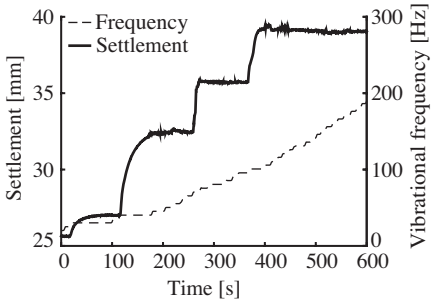

Figure B.1: Measured settlement and vibrational frequency over time, Test 1

B.2. RESULTS OF BATCH 1: TESTS 1-7, THE FIRST INSTALLATION AND DISMOUNTING ATTEMPTS WITH SLIP-JOINT SET 1

Figure B.1 presents the settlement and the frequency of vibration over time for the first installation test. Settlement events occur at several frequencies and after the applied frequency of 110 Hz no additional settlement is observed. After the final settlement event occurs at a frequency of 110 Hz, achieved at approximately t=380 s, the amplitude of vibration is increased and at the end of the test the amplitude tripled when the applied frequency is equal to 200 Hz, at t=600s; the absence of any settlements after the applied frequency of 110 Hz demonstrates that the settlement is not proportional to or even correlated with the amplitude of the applied force. Thus, the use of larger force amplitudes does not automatically result in larger observed settlement of the upper cone. Figure B.2 shows the results of tests 2 to 7. Six attempts were required to dismount the slip-joint for the first time. Before these attempts, it was unknown what (lift) force magnitude and which frequency were effective for dismounting purposes. A combination of an axial force of -40 kN and a frequency of vibration of 85 Hz, as shown in figure B.2(f), was successful for the initial dismounting of the cones.

B

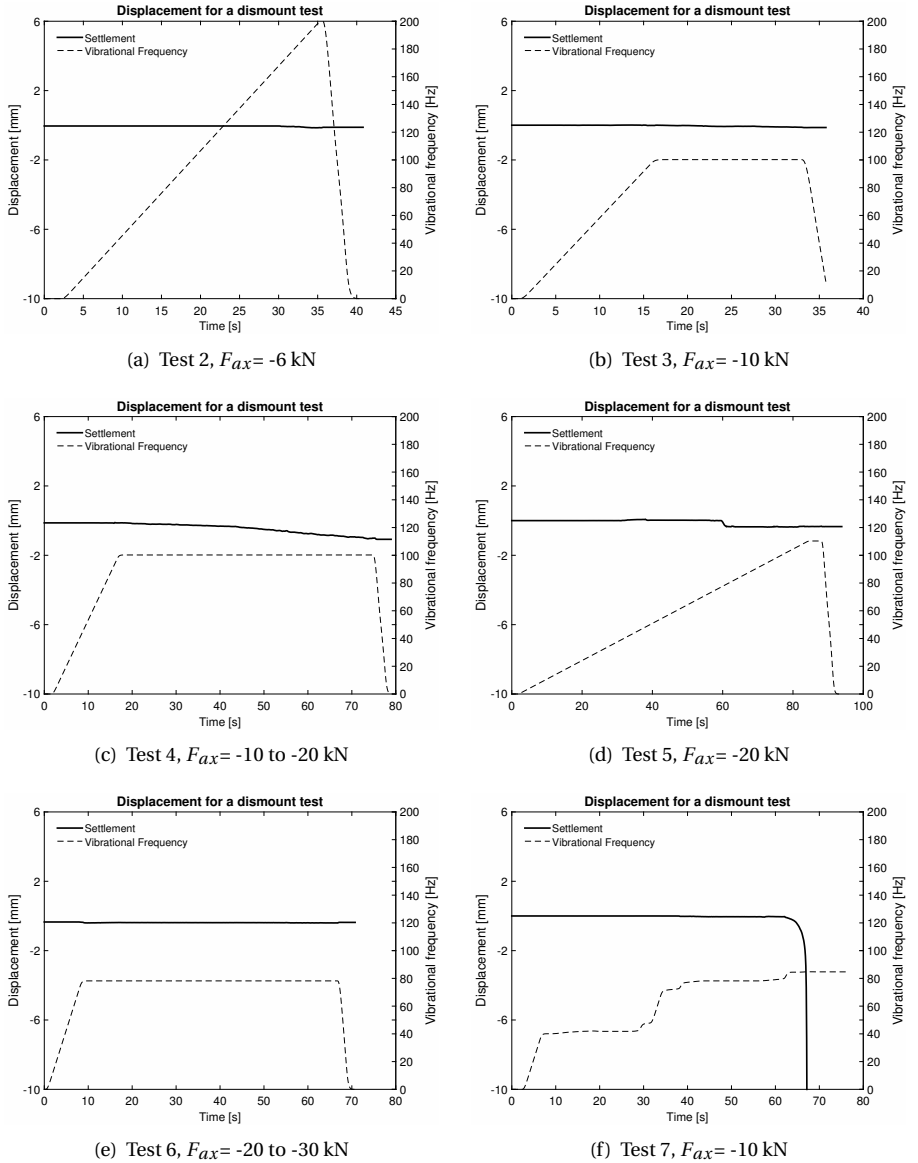

(a) Test 2, F_{ax}= -6 kN

(b) Test 3, F_{ax}= -10 kN

(c) Test 4, F_{ax}= -10 to -20 kN

(d) Test 5, F_{ax}= -20 kN

(e) Test 6, F_{ax}= -20 to -30 kN

(f) Test 7, F_{ax}= -10 kN

Figure B.2: The measured settlement of the upper cone and the frequency of the applied vibration in tests 2 to 7; The first dismounting tests (attempts) with their applied axial forces.

B.3. RESULTS OF BATCH 2: TESTS 8-11 WITH SLIP-JOINT SET 1

After the first batch of tests was completed, a set of ball bearings were installed underneath the hydraulic jacks to ensure the self-alignment of the two cones. This was done because the axial capacity was found to be smaller than expected after the initial installation test. The second installation and dismount tests were thus conducted with a slightly different set up than that used for the first batch. Figure B.3 presents the results of experiments 8 to 12 of Table B.2.

Figures B.3(a) and B.3(c) show that, by applying small steps in the frequency of vibration, settlement events were observed to occur at frequencies of vibration of 45, 70, 75, 95, 115, and 123 Hz. The distinct stick-slip behaviour and the time dependence of the vibration-induced settlement is observed between 756 s and 767 s in Figure B.3(b). This figure shows that, at a frequency of vibration of 115 Hz, two settlement cycles occur, with a stick event in-between. The second settlement cycle occurred after a period of 2 s of stick, during which the presumed resonance of the system builds up to a level necessary for a next sliding event. Thereafter, the test is continued and frequencies from 115 to 200 Hz are applied in test 8-2. Figure B.3(a) shows the continuation of the test and it is observed that at a applied frequency of approximately 115 Hz a slight settlement occurs. An additional sliding event is observed to take place when the frequency of the applied vibration is increased to 123 Hz. Note, that the settlement events in these test were observed to occur at slightly different frequencies to those observed in batch 1. This is attributed to the initial misalignment of the cones and the inability of the set up to self-align along the common axis in batch 1.

Test 9 investigated whether the slip-joint was able to bear the simulated weight of the mass of a turbine tower and an RNA. This test starts after the settlement obtained at the end of test 8. In test 9, the additional mass is simulated by applying an axial force of 60 kN to the joint. Figure B.3(d) presents the applied axial force and the measured settlement of the upper cone. The figure shows that no settlement was observed. Note, that the applied axial force of 60 kN was a sixfold increase as compared to the applied axial load in the installation test with vibrations.

Figure B.3(e) presents the results of test 10, which was a dismount test that features an axial pulling force of -30 kN. In this test, additionally, the frequency of the motors was slowly increased until the cones come loose. The figure shows that the cones started to loosen and dismount at an applied frequency of 127 Hz.

Figure B.3(f) presents the results of test 11, which was an installation test that featured an increase of the frequency of vibration from 0 to 128 Hz over 13 seconds. Thereafter, the frequency was lowered to 127 Hz and an additional settlement was observed. This observation indicates that, during the relatively rapid increase in frequency, the settlement had not fully developed. This obseveration demonstrates that the settlement that occurs needs time to develop in order to lead to a sliding event. If one of the effective

frequencies for settlement is passed by rapidly, an 'incomplete' settlement event can be expected. It can be concluded that the incremental increase in frequency can influence the behaviour of the vibration-induced settlement of the slip-joint.

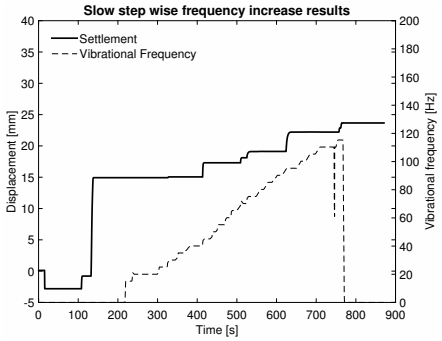

(a) Test 8-1

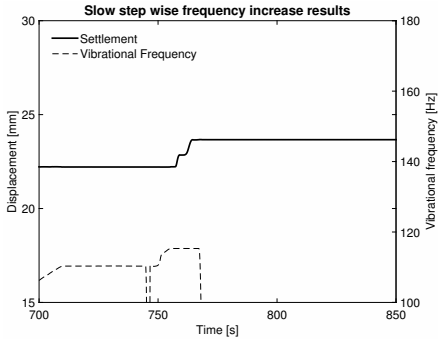

(b) Test 8-1 Zoomed at 750 s

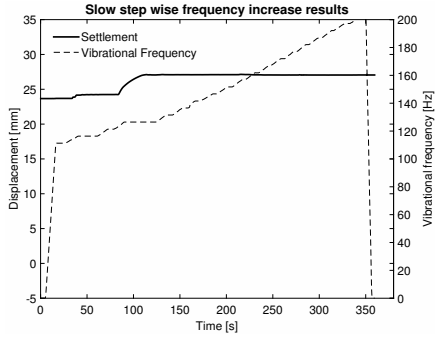

(c) Test 8-2

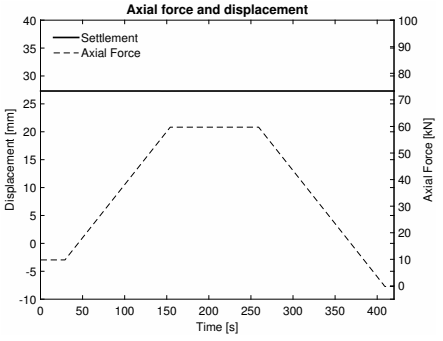

(d) Test 9

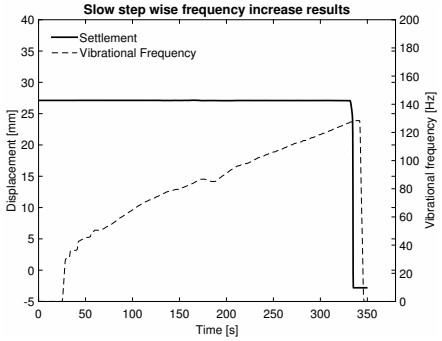

(e) Test 10

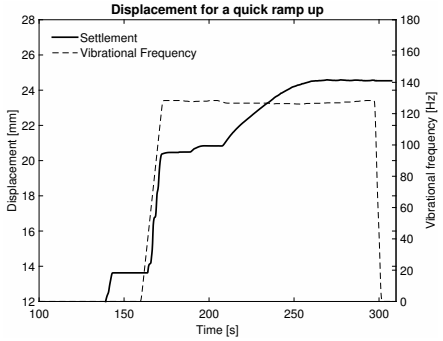

(f) Test 11

Figure B.3: The measured settlement of the upper cone and the frequency of the applied vibration in tests 8 to 11 of the second test batch.

B.4. RESULTS OF BATCH 3: TESTS 12-28 WITH SLIP-JOINT SET 2

After the first and second batch of experiments, slip-joint set 2 replaced set 1 in the experimental set up. Several installation and dismount tests were performed using set 2. One of the observations in batch 2 was that the manner in which the frequency is increased plays a role in the development of the settlement. Therefore, several experiments were conducted in order to investigate the time dependence of the settlement. Note that moat of these figures show an initial settlement; this is the result of the application of an axial force of 10 kN, the simulated self-weight of the slip-joint, which preceded b y the vibration induced settlement part of an individual test.

B.4.1. RESULTS OF THE INSTALLATION TESTS

Figure B.4(a) presents the results of test 12, which was an installation test that featured a step-wise increase of the frequency of vibration from 0 to 200 Hz. Settlements were observed to occur at forcing frequencies 30, 54, 86, 110, 115, and 126 Hz. The total settlement obtained was 14 mm. After applying a forcing frequency of 126 Hz no additional settlement was observed while the amplitude of the force was almost tripled with the increase in frequency to 200 Hz at approximately t=2100 s. This demonstrates that the application of larger forces does not necessarily result in larger settlement and that the frequency of vibration governs the degree of vibration-induced settlement in the slip-joint.

Figure B.4(b) presents results of test 14, which was an installation test with a step wise increase in frequency of the applied vibration from 0 to 200 Hz. Settlements were observed at forcing frequencies 30, 51, 53, 90, 108, 115, 122, and 126 Hz. The total settlement achieved was 11.5 mm. For tests 12 and 14, almost identical effective settlement frequencies were registered.

Figure B.4(c) presents the results of test 16, which was an installation test that featured a rapid increase of the frequency of vibration from 0 to 132 Hz over 15 seconds. The total settlement achieved was 10 mm. After reaching a frequency of 132 Hz the frequency of vibration was lowered to 127 Hz, which resulted in a continuation of settlement. Thereafter, a variation of the frequency did not lead to additional settlement. This result demonstrates that the final settlement level is determined by the duration of vibration applied at a certain effective frequency. This means that if one of the effective frequencies for settlement events is surpassed too rapidly, a lower settlement level will be observed.

Figure B.4(d) presents the results of test 18, which was an installation test that featured a rapid increase of the frequency of vibration from 0 to 126 Hz over 13 seconds. The variation in the frequency applied after the final settlement event did not result in additional settlement events. Comparing these observations with the results of test 16, they demonstrate that a rapid increase in frequency can reach the total settlement depth, but only when the frequency that is reached at the end of the increase in frequency is equal

to that of the effective frequency for settlement. The total settlement obtained during vibration was 13 mm.

Figure B.4(e) presents the results of test 20, which was an installation test that featured a rapid increase of the frequency of vibration from 0 to 126 Hz over 13 seconds. It reproduced the results of test 18 exactly: Both test 18 and test 20 showed that a final settlement depth can be reached with a rapid increase in the frequency of vibration. The total settlement achieved is 9.8 mm, which is smaller than in test 18. Note however that the initial settlement due to the simulated weight was slightly greater in test 20. The maximum settlement depth that can be reached with vibration is thus also influenced by the present conditions at the start of vibratory loading. If the settlement as result of the applied self-weight is larger or smaller, the settlement that is achieved by the use of vibratory loading is smaller or larger, respectively..

Figure B.4(f) presents the results of test 22, which was an installation test that featured a step-wise increase of the frequency of vibration from 0 to 200 Hz. Settlement events were found at forcing frequencies 30, 50, 52, 83, 105, 120, and 122 Hz. The total settlement observed during vibrating was 11.4 mm.

Figure B.5(a) presents the results of test 24, which was an installation test that featured a step-wise of the frequency of vibration from 0 to 200 Hz. Settlement events occurred at forcing frequencies 50, 52, 83, 105, 115, and 120 Hz. The total settlement achieved was 10.7 mm. Here, the settlement event that occurred at 30 Hz in test 22 was not observed. The other settlement events are, however, observed around similar frequencies as in test 22.

Figure B.5(b) presents the results of test 26, which was an installation test that featured a slow increase of the frequency of vibration from 0 to 125 Hz over 26 seconds. Thereafter, any variation in the frequency did not result in additional settlement events. The same end result as in test 12 and 14 was obtained with a relatively slow increase of the frequency in vibration. The total settlement achieved is 12.5 mm and it is a result of separate settlement events at multiple frequencies.

Figure B.5(c) presents results of test 28, which is an installation test that featured a slow increase of the frequency of vibration from 0 to 125 Hz over 60 seconds. The results can be considered to be a reproduction of test 26. The total settlement achieved was 11.3 mm. The individual settlement events were, as a result of the smaller increment of the increase of applied frequency, more noticeable.

B.4.2. RESULTS OF THE DISMOUNTING EXPERIMENTS

Figures B.6(a) to B.7(f) present the results of the dismounting tests performed with slip-joint set 2. Figures B.8(a) to B.9(b) present the axial loads applied during the dismounting tests. In the majority of the cases, a successful dismount was achieved using a vibration with a frequency of 125 Hz in combination with an axial force of -30 kN.

The results of tests 13, 15, 17, 19, and 21 show the sensitivity of the system to the application of a specific effective frequency of vibration and axial force combination. In Figures B.6(a) and B.6(b) it can be observed that the cones only dismounted when a frequency of vibration of 127 Hz was applied.
In Figure B.7(a) a rapid ramping up of the frequency of vibration to 127 Hz is observed to be successful in dismounting. In Figure B.7(b) it is observed that the frequency of vibration was slightly below the effective frequency at the end of the initial ramping up. Once the frequency was slowly increased, the cone dismounted.

In test 21, which is depicted in Figure B.7(c), one can observe exactly the opposite, namely that the frequency of vibration after the initial ramp up was slightly above the effective frequency. Once the frequency is slowly decreased the cones dismounts. The latter observation demonstrates the high relevance of the choice of the frequency of vibration for the settlement events. Figure B.8(e) shows that the axial load of test 21 was slowly increased to -30 kN in order to determine whether it was possible to dismount the cones with lower axial forces. Reaching an axial force of -30 kN the joint did not directly produce a dismount, and it was only after the frequency was increased to the effective frequency that a successful dismounting of the joint was achieved.

The results of tests 25 and 27, which are provided in Figures B.7(e) and B.7(f), show that a successful dismount was achieved for both a rapid and slow ramping up of the frequency of vibration. In test 27, a successful dismount was achieved with -20 kN (see Figure B.9(b)). This demonstrates that, even with 30 percent lower axial force, vibration at the correct frequency leads to a successful dismount. These results of the dismount tests prove that the frequency of the vibratory load is essential for a successful dismounting of the joint and that required settlement needs time to develop in order to allow vibration-induced movement.

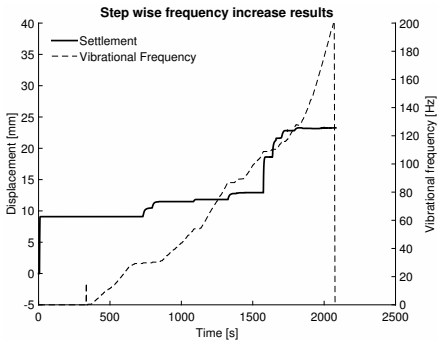

(a) Test 12

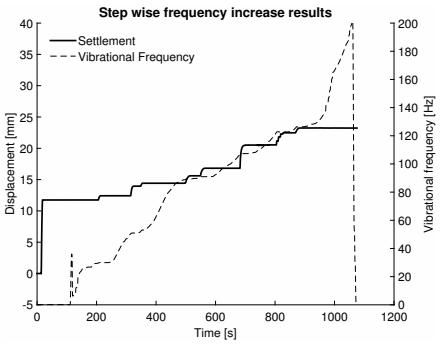

(b) Test 14

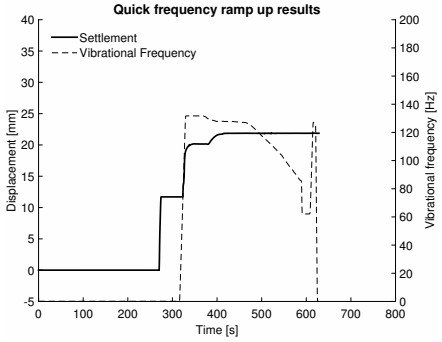

(c) Test 16

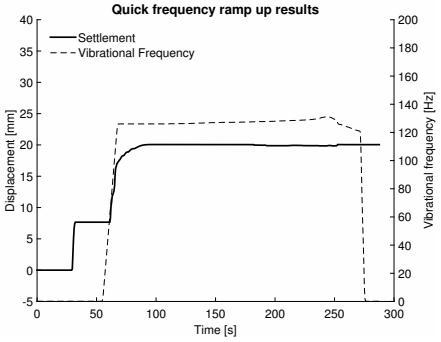

(d) Test 18

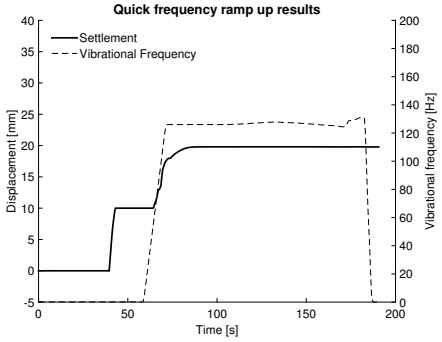

(e) Test 20

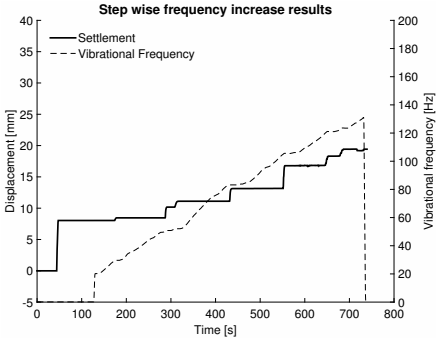

(f) Test 22

Figure B.4: The measured settlement of the upper cone and the frequency of the applied vibration in the installation tests with slip-joint set 2 of the third batch of experiments.

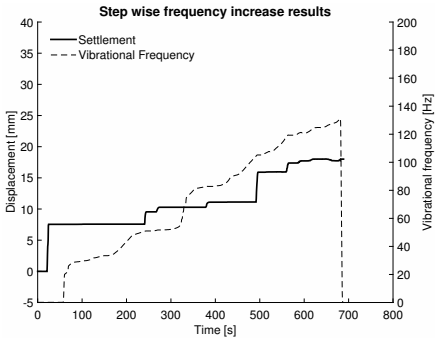

(a) Test 24

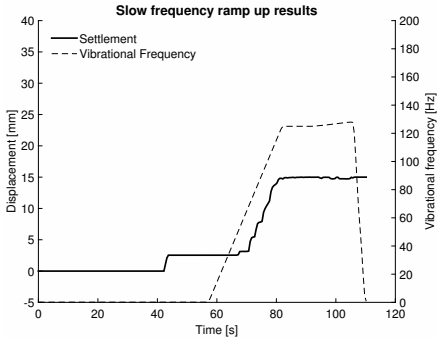

(b) Test 26

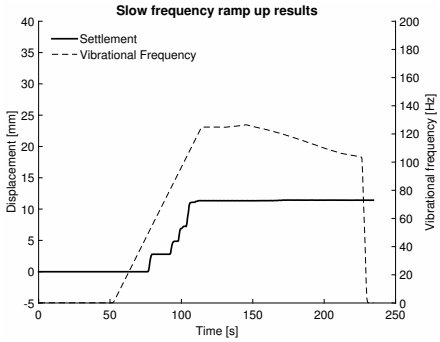

(c) Test 28

Figure B.5: The measured settlement of the upper cone and the frequency of the applied vibration in the installation tests with slip-joint set 2 of the third batch of experiments.

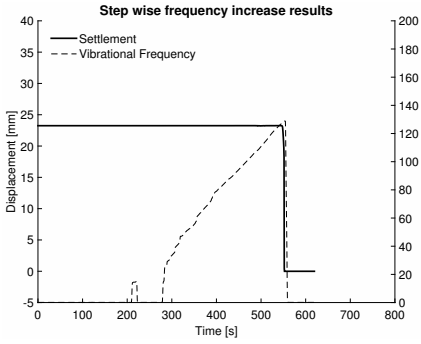

(a) Test 13

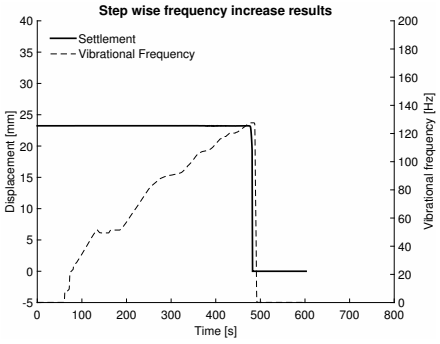

(b) Test 15

Figure B.6: The measured settlement of the upper cone and the frequency of the applied vibration in the dismount tests with slip-joint set 2 of the third batch of experiments.

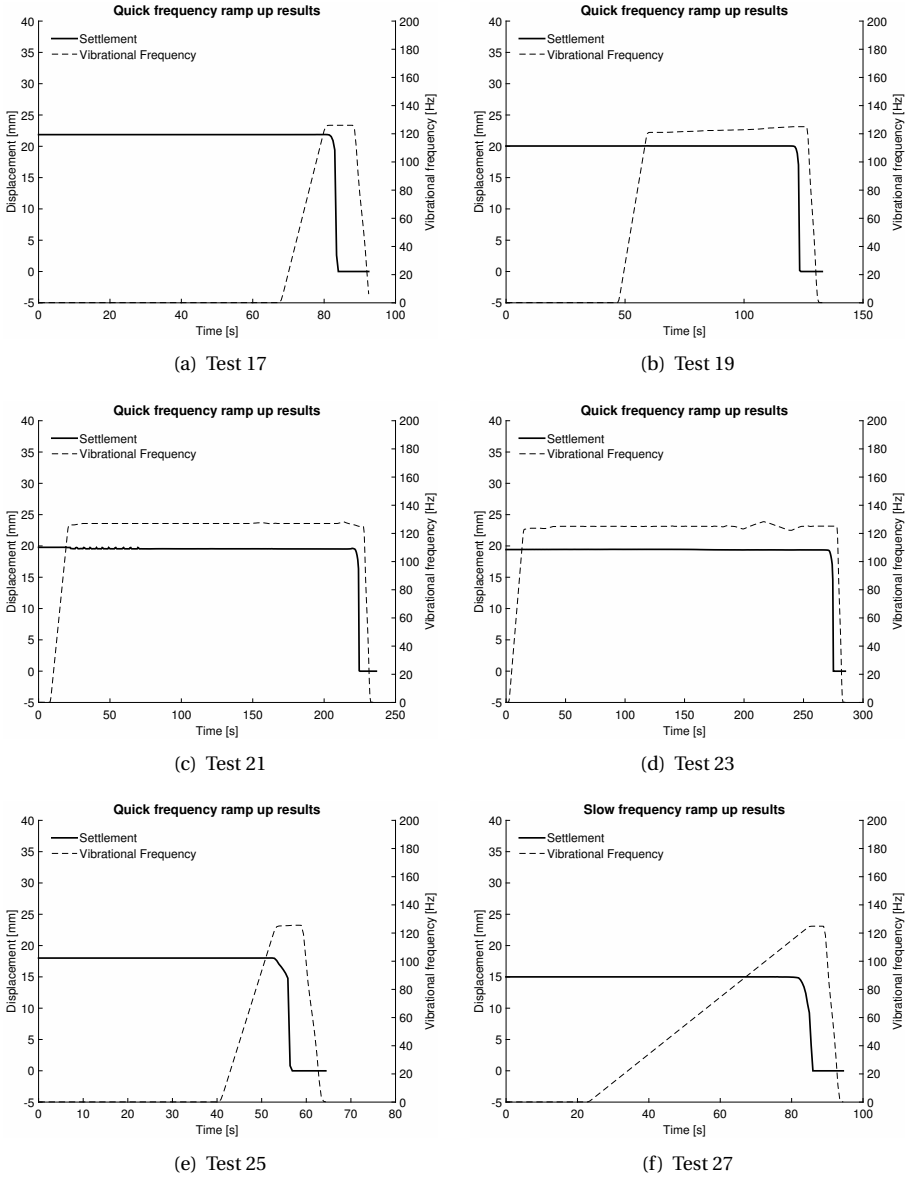

(a) Test 17

(b) Test 19

(c) Test 21

(d) Test 23

(e) Test 25

(f) Test 27

Figure B.7: The measured settlement of the upper cone and the frequency of the applied vibration in the dismount tests with slip-joint set 2 of the third batch of experiments.

B

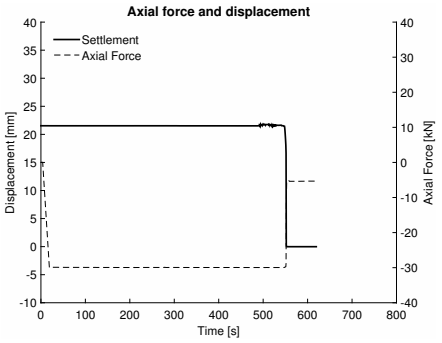

(a) Applied axial force Test 13

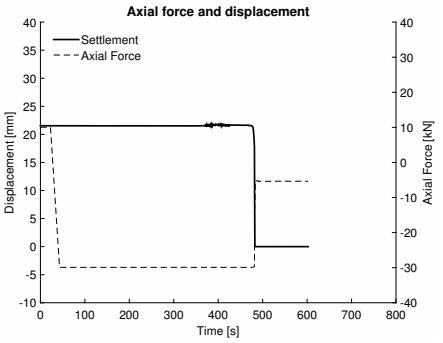

(b) Applied axial force Test 15

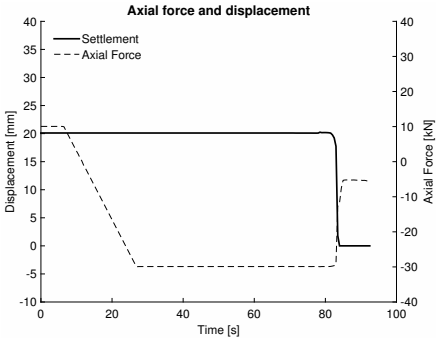

(c) Applied axial force Test 17

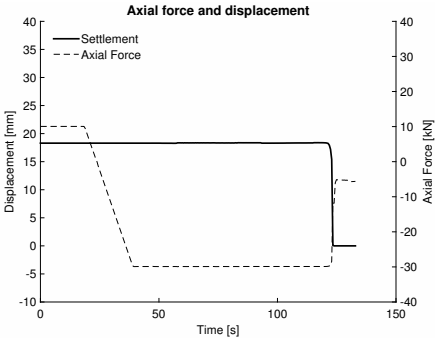

(d) Applied axial force Test 19

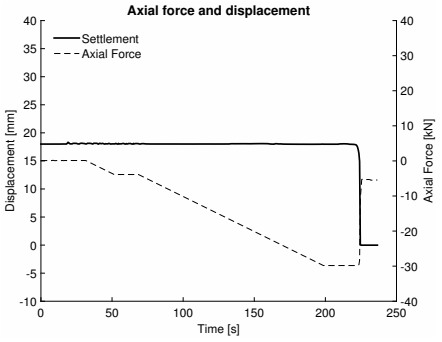

(e) Applied axial force Test 21

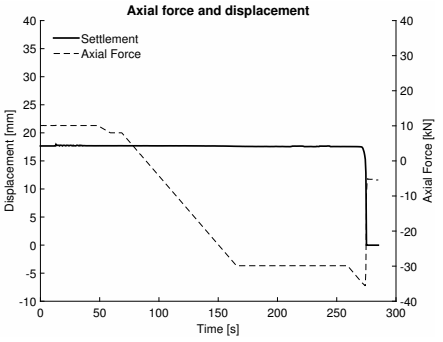

(f) Applied axial force Test 23

Figure B.8: The applied axial loads and measured settlements during the third batch of dismounting tests of slipjoint set 2.

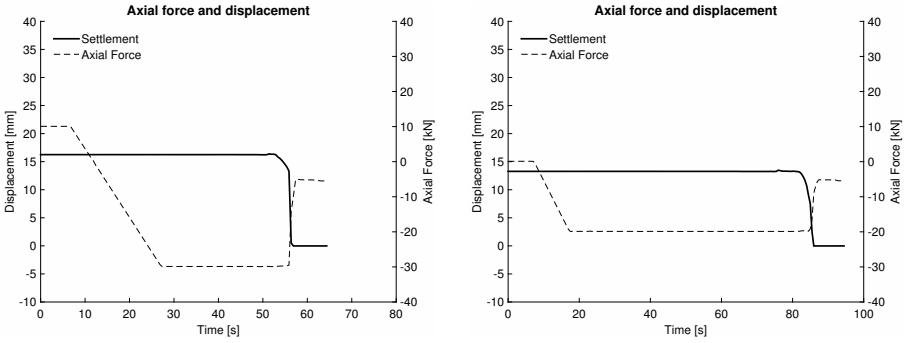

(a) Applied axial force Test 25

(b) Applied axial force Test 27

Figure B.9: The applied axial loads and measured settlements during the third batch of dismounting tests of slipjoint set 2.

B.5. RESULTS OF BATCH 4: TESTS 29-31 WITH SLIP-JOINT SET 2

In this batch, the installation sequence of the slip-joint was divided into several steps: After the stabilization of each settlement event, the test was stopped and multiple hammer impact tests were conducted. These impact tests were performed in order to track the changes in the dynamic response of the slip-joint to a pulse load. Figures B.10(a) to B.10(e) present the settlement events per sub-step. In Figure B.10(c), it is interesting to note that, after 40 seconds three stick-slip cycles were still observed, while the frequency was kept constant at 98 Hz over 10 seconds. This demonstrates that settlement at this frequency required time to develop into a sliding event.

Figure B.11 presents the measurements of the two dismount experiments in this batch. The results of both tests are almost identical and the cones loosen into a successful dismount when a frequency of 110 Hz is applied. A slow increase of the frequency in combination with an axial force of -20 kN is thus sufficient to dismount a slip-joint.

B.6. RESULTS OF BATCH 5: TESTS 32-42 WITH SLIP-JOINT SET 2

In this batch several tests were reproduced and experiments similar to those conducted in batch 4 were executed in order to reproduce the changes in the response of the slip-joint. Note that only some of the results of the experiments conducted in this batch are given here.

B.6.1. RESULTS OF THE INSTALLATION EXPERIMENTS

Figure B.12(a) depicts the obsevered settlement of the upper cone as a result to a slow increase of the frequency of the applied vibration up to 118 Hz and subsequently the frequency is increased to 130 Hz. Several settlement events are observed during the initial phase in which frequency is slowly increased. Increasing the frequency from 118 Hz to 130 Hz did not result in additional events. Figures B.12(b) and B.12(c) present the settlement levels at the start and end of test 34. In test 34, the frequency was increased in steps from 0 to 200 Hz. In total, only 5 mm of settlement was achieved during this experiment.

Figures B.12(d) and B.12(e) present the observation at the start and at the end of test 36. Between the settlement events the vibration was stopped and hammer impacts test were executed. In test 36, a total of 7.55 mm of settlement was obtained by all settlement events. At this point, it became clear that the repetitive testing left wear marks on the contact surfaces, which influenced the settlement that could be achieved by the application of axial load and vibration.
In test 40, the axial force that simulated the self-weight resulted in only 0.5 mm of settlement, whereas, in previous tests, settlement of approximately 7 mm was observed. This reduction of achieved settlement after the self-weight was simulated can be attributed

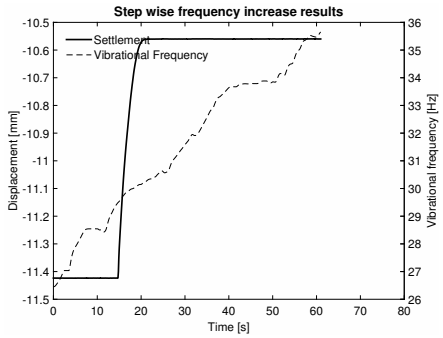

(a) Test 30-2; 25-35 Hz

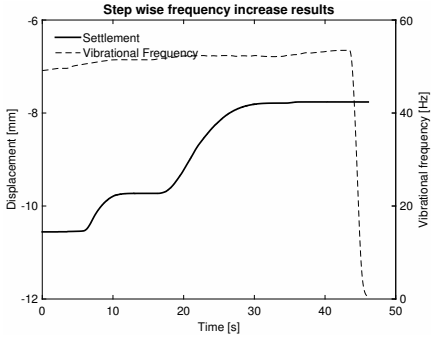

(b) Test 30-4; 45-55 Hz

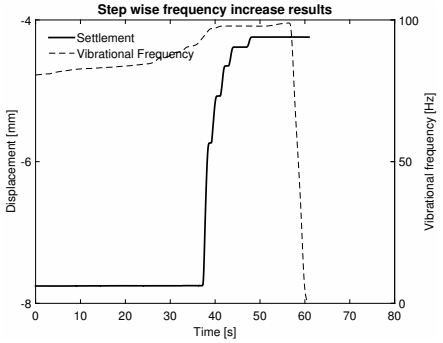

(c) Test 30-6; 80-100 Hz

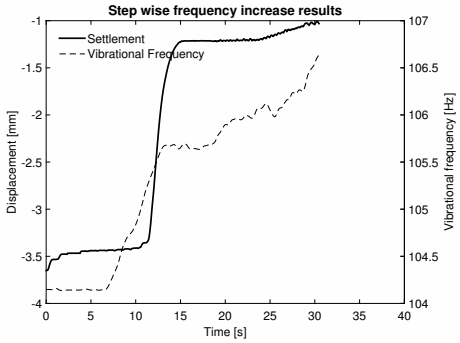

(d) Test 30-8; 104-106 Hz

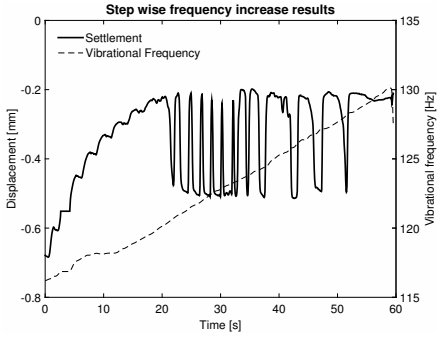

(e) Test 30-10; 115-130 Hz

Figure B.10: The measured settlement of the upper cone and the frequency of the applied vibration in the installation tests with slip-joint set 2 of the fourth batch of experiments.

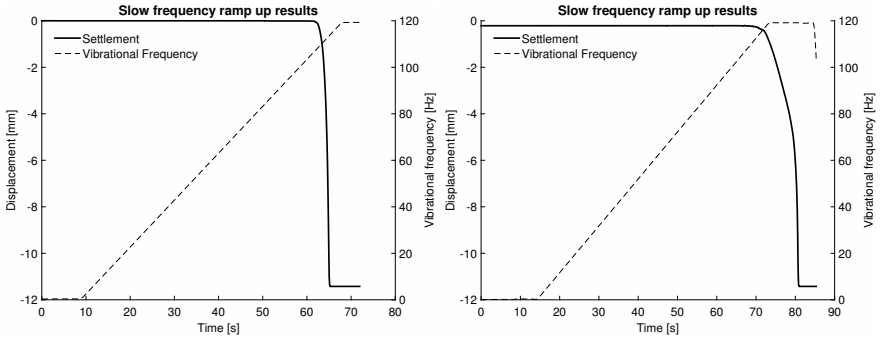

(a) Test 29 (b) Test 31

Figure B.11: The measured settlement of the upper cone and the frequency of the applied vibration in the dismount tests with slip-joint set 2 of the fourth batch of experiments.

to the increase of friction due to the wear that occurred at the contact areas. The results of test 41, which followed after the small settlement obtained in test 40, are given in Figure B.12(f). The figure shows that a settlement of 12 mm was achieved as a result of a frequency increase from 0 to 123 Hz over 60 seconds. The final settlement depth in test 41 was found to be 1 mm less than in test 36; this illustrates the degradation of the slip-joint as a result of repetitive testing. The results of test 40 and 41 show that wear affects settlement levels and that the vibration-induced settlement is decreased by wear.

B.6.2. RESULTS OF THE DISMOUNTING EXPERIMENTS

Figures B.13 and B.14 present the measured settlements of the upper cone and the axial loads applied during the dismounting tests in batch 5. Figures B.13(a), B.13(b), B.14(a) and B.14(b) show that the joint only dismounted while a vibration with a frequency of 120 Hz is applied in combination with an increased axial load of -24 kN. The increase in the required axial load for a successful dismount reconfirms the increase in apparent friction due to wear.

The results of the dismounting test 35 are reflected upon in Figures B.13(c) and B.14(c). These figures show that a successful dismount was achieved by shaking with a frequency of 118 Hz and applying an axial force of -20 kN.

After test 35, the cones required larger axial force for successful dismounts. This was illustrated by tests 37-39, where, finally an axial force of -36 kN was necessary to dismount. Results of tests 37 and 38 are given in Figures B.13(d), B.13(e), B.14(d) andB.14(e). The results of test 39 were not successfully measured.

Figures B.13(f) and B.14(f) depict a successful dismounting of the slip-joint of test 42 while shaking at 118 Hz and applying an axial force of -30 kN.

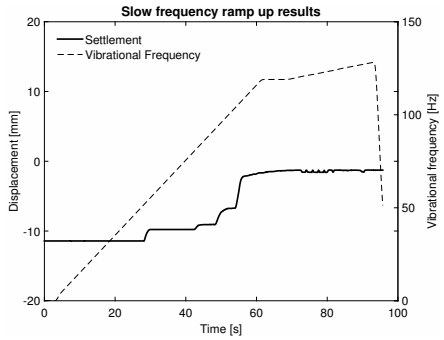

(a) Test 32

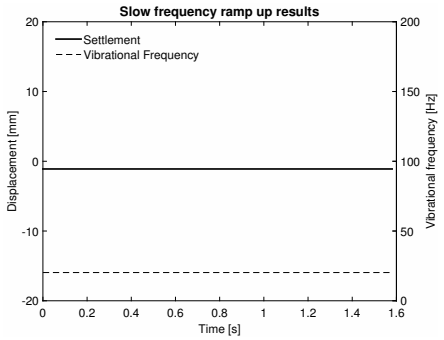

(b) Test 34-1

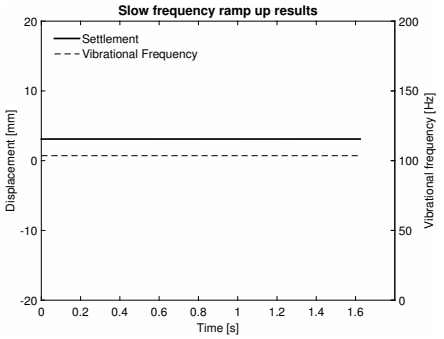

(c) Test 34-15

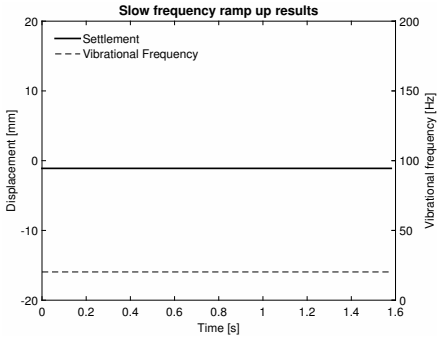

(d) Test 36-4

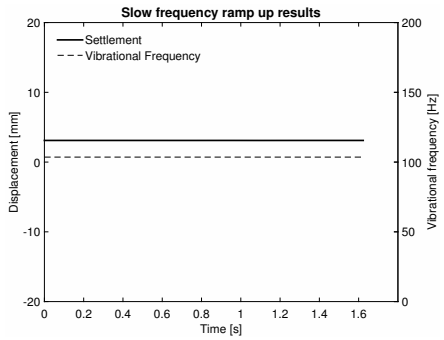

(e) Test 36-14

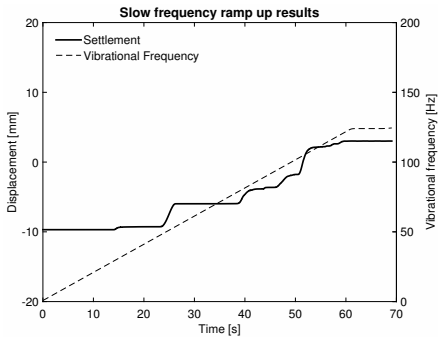

(f) Test 41

Figure B.12: The measured settlement of the upper cone and the frequency of the applied vibration in the installation tests with slip-joint set 2 of the fifth batch of experiments.

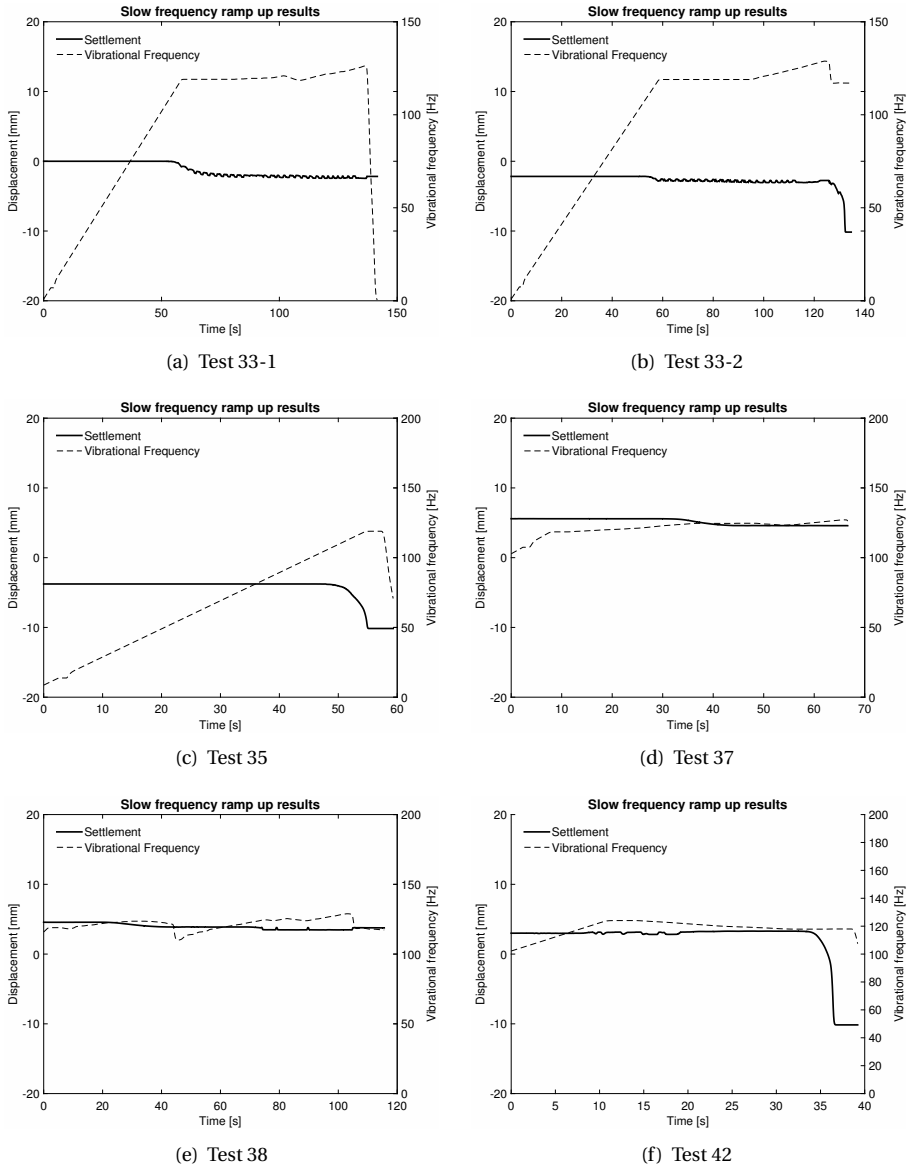

(a) Test 33-1

(b) Test 33-2

(c) Test 35

(d) Test 37

(e) Test 38

(f) Test 42

Figure B.13: The measured settlement of the upper cone and the frequency of the applied vibration in the dismount tests with slip-joint set 2 of the fifth batch of experiments.

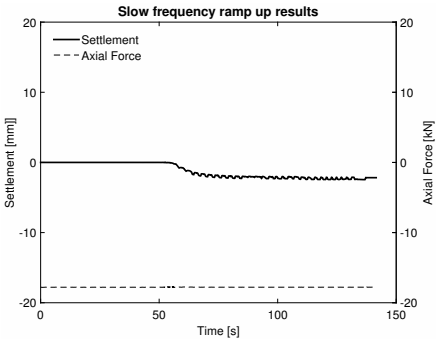

(a) Applied axial force Test 33-1

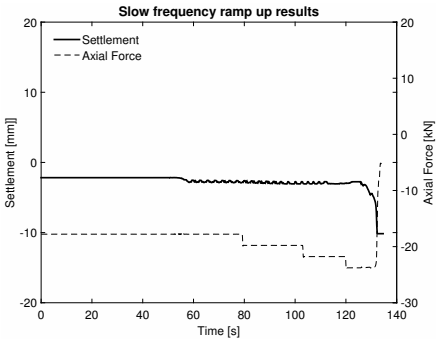

(b) Applied axial force Test 33-2

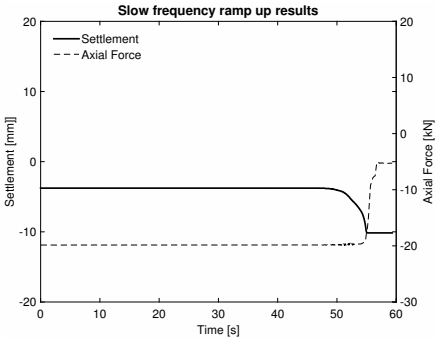

(c) Applied axial force Test 35

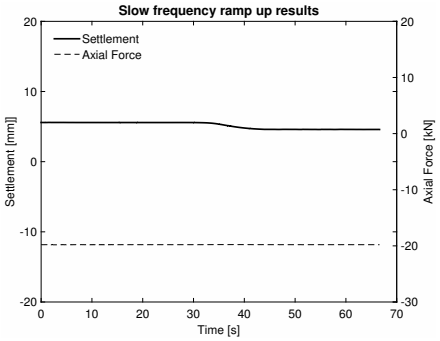

(d) Applied axial force Test 37

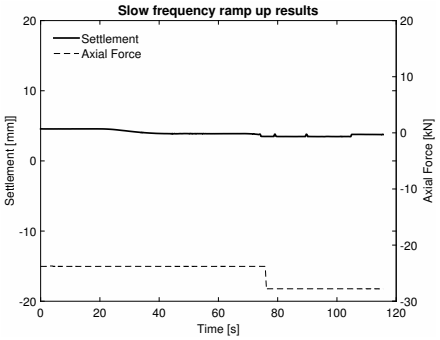

(e) Applied axial force Test 38

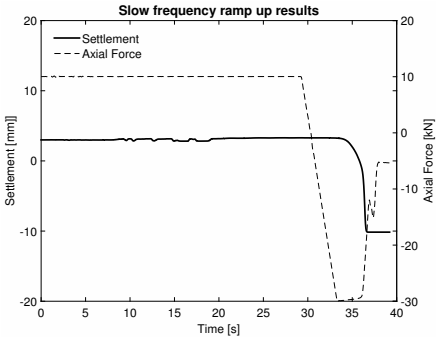

(f) Applied axial force Test 42

Figure B.14: The measured settlement of the upper cone and the frequency of the applied vibration in the dismount tests with slip-joint set 2 of the fifth batch of experiments.

B.7. RESULTS OF BATCH 6: TESTS 43-56 WITH SLIP-JOINT SET 2

Before this batch was executed, the individual cones of set 2 were polished in order to reduce the effects of the wear marks. In the sixth batch, the eccentric motors where replaced by an electric shaker. In comparison with the eccentric motors, the point at which the vibrations were introduced was completely different, as it was applied at a single point on the surface of the transition piece. In total, four locations were used to check the sensitivity of the results to the application point. Other differences between the eccentric motors and the electric shaker are that the latter can apply a smaller, but controllable amplitude. Furthermore, the shaker is able to introduce vibration of a single frequency instantaneously and that the larger operational frequency band of the shaker allows investigation into frequencies far above 200 hz. A downside of the used electric shaker system is that the frequency of vibration could not be logged by the data acquisition system available. The frequency was therefore logged on paper, and the applied frequency over time is thus omitted in some figures.

B.7.1. RESULTS OF THE INSTALLATION EXPERIMENTS

The first installation experiments intended to determine whether the electric shaker was powerful enough to induce a settlement event. Therefore, the applied axial force was increased to 20 kN in the initial installation test to be sure that the wear did not prevent settlement events from occurring. Tests 44-51 were attempts to install the slip-joint. These tests investigated the effects of the choice of shaker and the amplitude of vibration on the settlement results.

Figures B.15 and B.16 depict the observed settlements of the upper cone and the forces at the shaker head of the initial attempts to install the slip-joint with an electric shaker. The results of tests 44 and 45 show two similar settlement patterns at approximately the same effective frequencies. The main difference between these tests is that an additional axial force of 2 kN was added in test 45. These results again show that multiple frequencies are found to be effective for settlement events are found and reconfirms that settlement of the system is governed by the frequency and less by the amplitude of the force.

Tests 46-48 were performed after test 45 to investigate whether additional settlement could be achieved with 30, 60, and 90 percent of the maximum amplitude of the applied vibration. No additional settlement was observed and therefore not given here.
In tests 49-51 the three amplitude levels were again tested, and an additional axial force of 4 kN was added to 20 kN to enable settlement. The settlement of the upper cone and the measured force at the shaker of these tests are presented in Figures B.16(a) to B.16(c). The figures show that shaking with 60 and 90 percent of the maximum amplitude resulted in additional settlement events; these results proved that the final settlement depth can be controlled by means of the amplitude applied.

Figure B.16(d) presents the observed settlements and the forces at the shaker-head

during test 53. In this test, an axial force of 28 kN and a constant frequency of vibration of 248 Hz were applied. During the test, the amplitude of the force was increased in a step-wise manner. The figure shows that the first four amplitude steps resulted in a settlement step, with a total settlement of 5 mm. Each settlement event reached an equilibrium depth after a short period. After the fourth step, the additional increase of the amplitude had no effect. These results demonstrate that the settlement level of the joint is controllable by the use of the amplitude and that the settlement of the joint shows a stabilizing behaviour after each settlement event.

Figure B.16(e) presents the results of test 55. Here, only 1.5 mm of settlement was achieved by a frequency sweep from 20 to 300 Hz over the first 280 seconds. Thereafter, the frequency of the shaker was reduced to 249 Hz but no additional settlement occurred. The small settlement is attributed to the wear of the contact areas on the individual cones.

Figure B.16(f) presents the settlement and force at the shaker for test 56. In this test, a constant frequency of 249 Hz and an axial force of 28 kN were applied. The figure shows that additional settlement events occurred when shaking with larger amplitudes. In comparison with test 55, the amplitude doubled; one can, therefore, conclude that, while shaking at one of the effective frequencies, the amplitude of the vibratory load can be used to control the settlement depth.

B.7.2. RESULTS OF THE DISMOUNTING EXPERIMENTS

Figure B.17 presents the results of the two dismount tests performed in batch 6. In both dismount tests the application of vibration with a frequency of 249 Hz led to a successful dismount. In test 52, two slow sweeps between 230 and 250 Hz were performed, and the axial force needed to be increased before the cones dismounted. In test 54 a constant frequency of 249 Hz was used.
Figure B.17(b) shows that the axial force needed to be increased to -30 kN before the cones dismounted. A successful dismount was achieved with a higher frequency in the previous batches. In the next batch, more investigations into the effective frequencies are performed with slip-joint set 1.

B

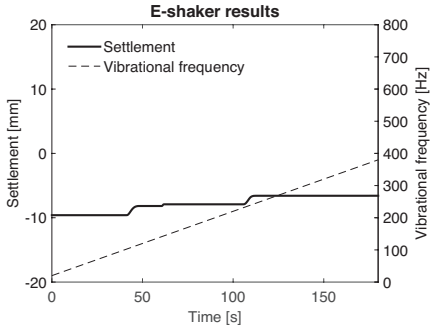

(a) Test 44; F_{ax}=18 kN

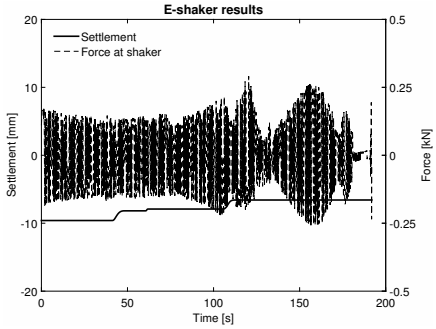

(b) Force at shaker Test 44

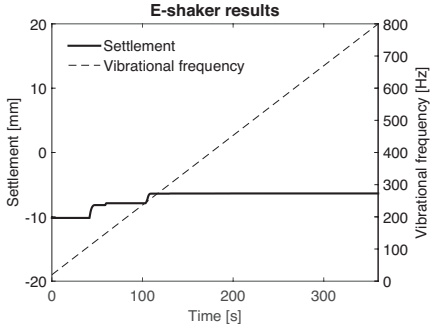

(c) Test 45; F_{ax}=20 kN

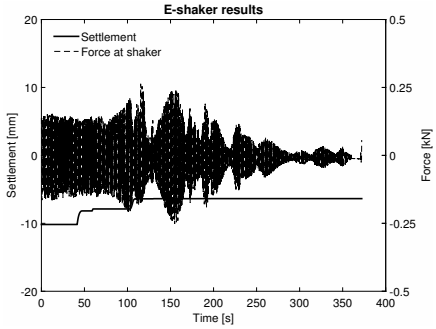

(d) Force at shaker Test 45

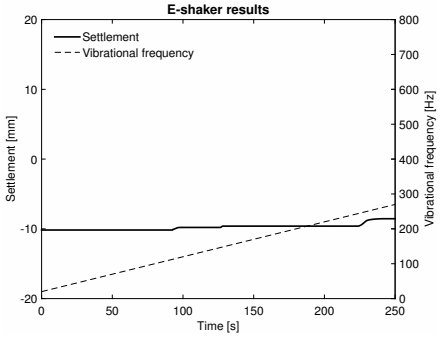

(e) Test 50; F_{ax}=24 kN

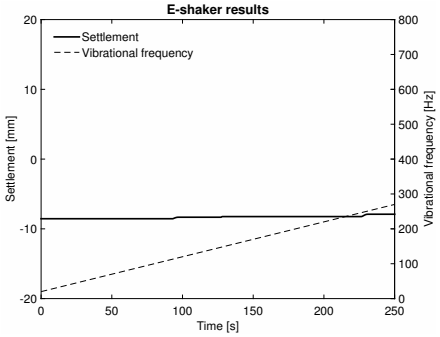

(f) Test 51; F_{ax}=24 kN

Figure B.15: The measured settlement of the upper cone, the frequency and amplitude of the applied vibration in the installation tests with slip-joint set 2 of the sixth batch of experiments.

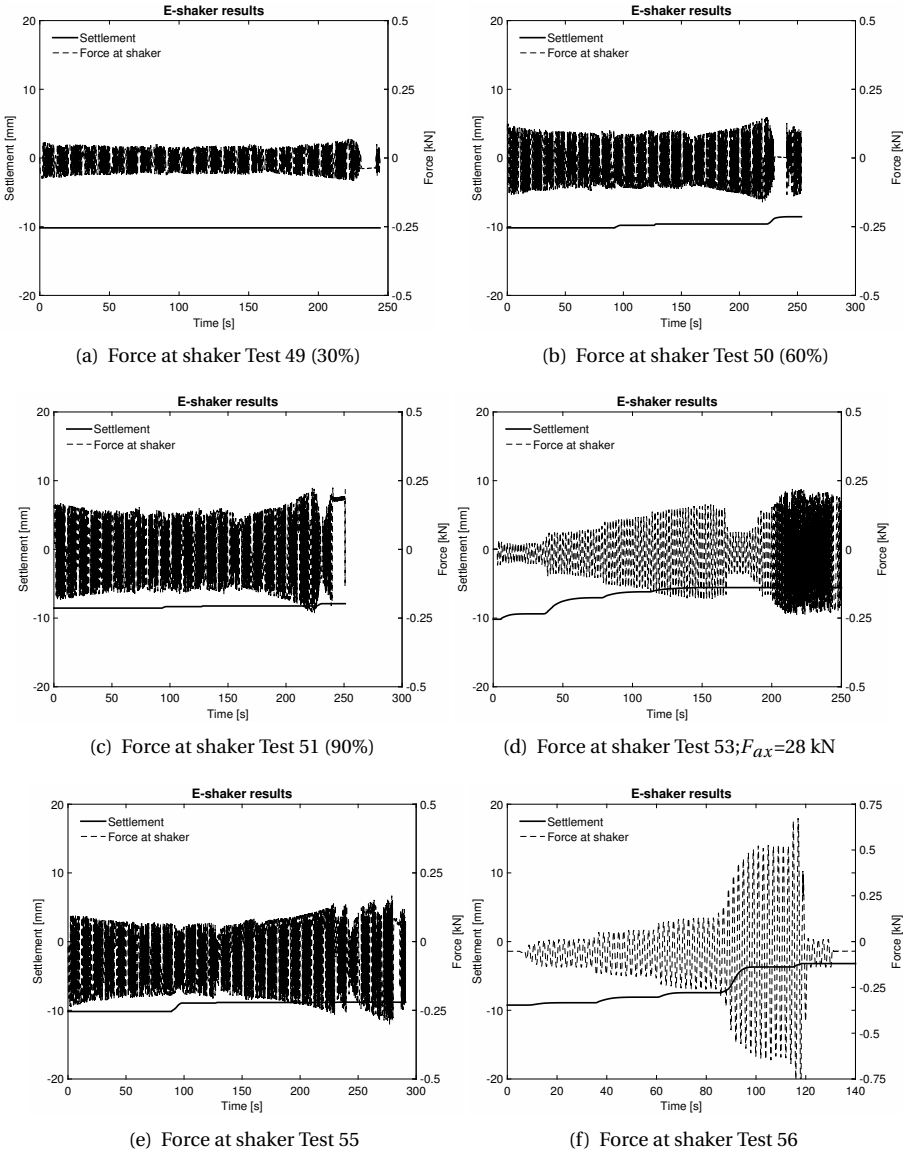

(a) Force at shaker Test 49 (30%)

(b) Force at shaker Test 50 (60%)

(c) Force at shaker Test 51 (90%)

(d) Force at shaker Test 53;F_{ax}=28 kN

(e) Force at shaker Test 55

(f) Force at shaker Test 56

Figure B.16: The measured settlement of the upper cone, the frequency and amplitude of the applied vibration in the installation tests with slip-joint set 2 of the sixth batch of experiments.

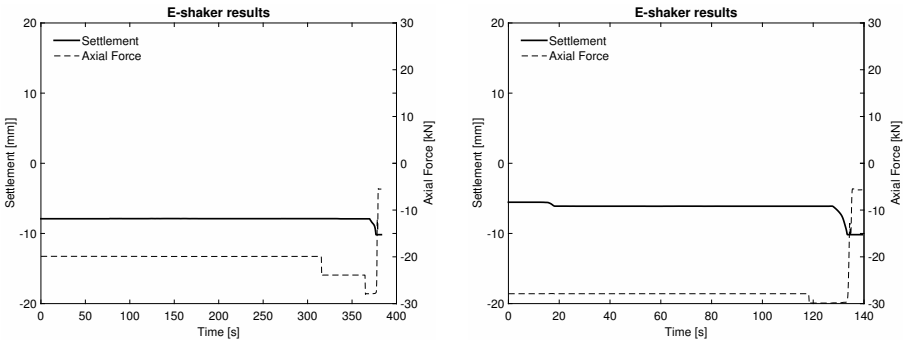

(a) Applied axial force Test 52

(b) Applied axial force Test 54

Figure B.17: The applied axial loads during the sixth batch of dismounting tests of slipjoint set 2.

B.8. RESULTS OF BATCH 7: TESTS 57-75 WITH SLIP-JOINT SET 1

In batch 7, slip-joint set 2 is replaced with set 1, which was used in the experiments conducted in batch 1 and 2. The aim is to reproduce the results of the experiments of batch 1-5 where the eccentric motors were applied. This would make it possible to make a comparison between the observations as a result of the application of the shaker and those of the eccentric motors. This section is divided into a subsection that present the results of the installation test and another section with the results of the dismount experiments.

B.8.1. RESULTS OF THE INSTALLATION EXPERIMENTS

Figures B.18(a) and B.18(b) present the settlement and forces at the shaker used in test 58. In this test, the frequency was increased in steps from 20 to 400 Hz, and an axial force of 10 kN was applied. Settlement events occurred at frequencies 70, 77, 105, 113.5, 116, 118, and 120 Hz (these frequencies were manually noted during the test, as recording the frequency of the shaker was not possible), which resulted in a total settlement of 8.5 mm. After the settlement event that occurred at 120 Hz, no additional events were observed when the frequency was increased to 400 Hz. This test almost reproduced the results of test 8 of batch 2 which was executed with eccentric motors. This is remarkable as the electric shaker applies a vibration with force amplitudes of 50 to 250 times smaller than the amplitudes applied by the eccentric motors. The settlements achieved in test 58 and in test 8 were of the same order, and these results prove that settlement behaviour is mainly determined by the frequency at which the system is vibrated and not by the amplitude of vibration. When comparing the magnitude of the axial force and the obtained settlement depth of this batch and the previous batch, it can be seen that the applied forces in the previous batch were much larger. This observation confirms that the previous set and the observations were affected by wear.

In Figures B.18(c) and B.18(d), the settlement and forces at the shaker of test 60 are given. This test was performed with an axial force of 10 kN and a constant frequency of 119 Hz. The figures show that the settlement occurred in several stick-slip cycles. After the initial settlement was stabilized an attempt was made to increase the settlement depth by increasing the amplitude to the maximum. This did not result in additional settlement. It was only after the frequency was increased to 123.5 Hz that an additional 0.5 mm was obtained. Increasing the frequency up to 200 Hz in small steps did not result in additional settlement events. These results again demonstrate that the influence of the amplitude of the vibration is limited. The frequency of the vibration must be equal or close to one of the effective frequencies of the system in order to induce a settlement event.

To check if an additional settlement event could be found above 200 Hz, installation test 60 was followed by a frequency sweep from 20 to 320 Hz with an increment of 1 Hz/s in test 61. At 240 Hz, a micrometer of settlement was observed to occur. This result is negligible and is therefore not given in this appendix. Beyond this micrometer shift, no

additional settlements occurred, and it can be concluded that the limit of the settlement was reached within the same frequency band as the eccentric motors. The results of batch 6 did show that the frequency of 249 Hz was also effective in creating settlements. The results of test 61 indicate that the sequence in which the frequencies are applied does affect the end result. Frequencies of approximately 240 or 120 Hz can both be used to obtain the same end result.

In Figures B.18(e) and B.18(f), the settlement of the upper cone and the force at the shaker of test 63 are given. In this test the frequency is slowly manually increased from 20 to 320 Hz. The frequencies at which settlement events occurred were manually noted as being 110, 115, 117, 118, and 119 Hz. These events resulted in a total settlement of 4.7 mm.

In Figures B.19(a) and B.19(b), the settlement of the upper cone and the force at the shaker of test 65 are given. In this test, the frequency was kept constant at 120 Hz, in combination with an axial force of 10 kN. With a small increase in the applied force, additional settlement events occurred which resulted in a total settlement of 7 mm. Remarkably, the applied force during the settlement events was found to be very small (0.05 kN). This may be explained by the presence of a resonance frequency at 120 Hz which resulted in a smaller force being required to maintain the required energy level that was used to supply the force at the shaker. After the final settlement was reached, the frequency of the force was slowly increased up to 2 kHz but, no additional settlement was observed.

In test 66, a frequency sweep was performed in order to to check at which frequencies between 0 and 300 Hz response peaks occurred. The largest responses at the accelerometers were observed and manually noted at approximately 123, 151, 261, and 275 Hz. This result is not visualized in this appendix as the frequency of the vibration could be observed but not measured.

In Figures B.19(c) and B.19(d), the settlement and the force at the shaker of test 68 are given. This test is a reproduction of test 63, and the frequency was slowly increased manually from 20 to 320 Hz; an axial force of 10 kN was also applied. The frequencies at which settlement events occurred were 113, 118, and 119 Hz, resulting in a total settlement of 3 mm. A smaller total settlement was achieved than in test 63, which is attributed to wear of the contact surface.

In Figure B.19(e) and B.19(f), the settlement and force at the shaker of test 70 are given. This test reproduces test 65. The frequency was kept constant at 120 Hz in combination with an axial force of 10 kN. Again, settlement events occurred with increasing shaker force. A total settlement of 4.6 mm was obtained. The obtained settlement was smaller than obtained in test 65, while the applied force at the shaker head was larger. This clearly shows the influence of wear of the contact surfaces on the settlement obtained. It is again noticeable that the amplitudes at the settlement events were small.

In test 71, a frequency response test was again performed by sweeping the shaker frequency from 20 to 300 Hz. This time, the shaker was located at a position that was closer to the open end of the transition piece. The response peaks at the accelerometers were observed at 84, 94, 120, 427, 150, and 262 Hz. The largest peaks were found at 120 Hz and 262 Hz.

In test 73, the effectiveness of the frequencies that corresponded to these response peaks was investigated. In Figure B.20(a) the settlement and the force at the shaker of test 73 are presented. During the first 600 second, the settlement events were achieved with standard harmonic vibration. After 600 seconds, a block-shape function was used and an additional settlement was observed. A total settlement of 10 mm was obtained. This result shows that the vibration shape can also influence the settlement depth. Furthermore, this result indicates that the electric shaker is capable of inducing the same settlement levels as the much more powerful set of eccentric motors. Another observation is that the settlement depths achieved by shaking closer to the open end are somewhat larger than the settlements obtained when shaking closer to the clamped end.

In test 75, the goal was to investigate the effect of the order in which the vibration frequencies were applied. In this test, a frequency of 262 Hz was initially used and after the settlement event stabilized the frequency of vibration was lowered to 120 Hz. Figure B.20(b) presents the result of test 75. It was observed that the settlement increased with an increasing amplitude of vibration at 262 Hz. After 200 seconds, a block-wave function was used, but no additional settlement is observed. Thereafter, the frequency of vibration was lowered to 120 Hz, and no settlement event was observed. This result shows that multiple frequencies are effective in obtaining a final settlement depth. This statement is based on tests 67, 70, and 73. When compared to test 75, the sequence of frequencies was reversed in tests 67 and 70, but these tests showed no additional settlement when the frequency was switched to the other effective frequency.

B.8.2. RESULTS OF THE DISMOUNTING EXPERIMENTS

Figure B.21 presents the results of dismount tests 57, 59, and 62. In test 57, the axial force was increased to -34 kN and in combination with a frequency of 269 Hz, this increase in axial force resulted in an effective dismount. Both tests 59 and 62 resulted in a successful dismount by means of shaking with 119 Hz and applying an axial force of -30 kN. These results confirm that multiple frequencies are effective in creating settlement events. In test 62, the force at the shaker was slowly increased until the dismount was successful. This result shows that there is a critical amount of energy, that is required to induce a settlement event.

Figure B.22 shows the results of dismounting tests 64, 67 and 69. In these three tests, successful dismounts were obtained by shaking with a frequency of 119 and 120 Hz. An axial force of -24 kN was sufficient to dismount in tests 64 and 67, and in test 69, an axial force of -20 kN was sufficient.

Figure B.23 shows the results of dismounting tests 72 and 74; both dismounted success-

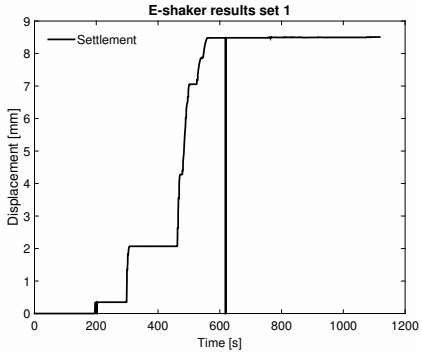

(a) Test 58; F_{ax}=10 kN

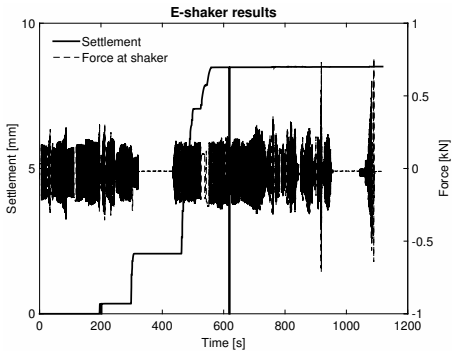

(b) Force at shaker Test 58

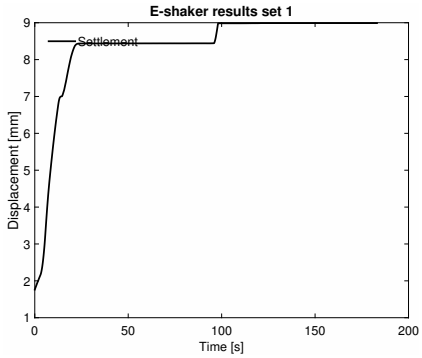

(c) Test 60; F_{ax}=10 kN - 119 Hz

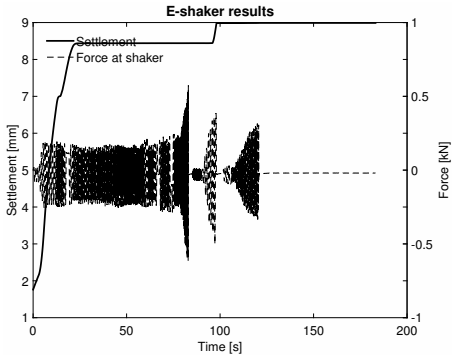

(d) Force at shaker Test 60

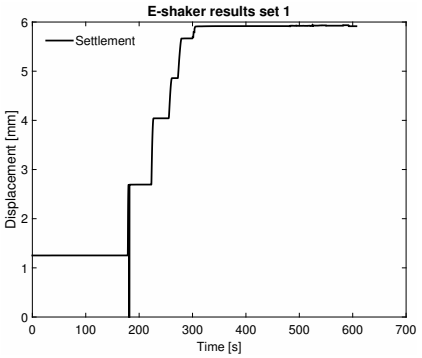

(e) Test 63; F_{ax}=10 kN

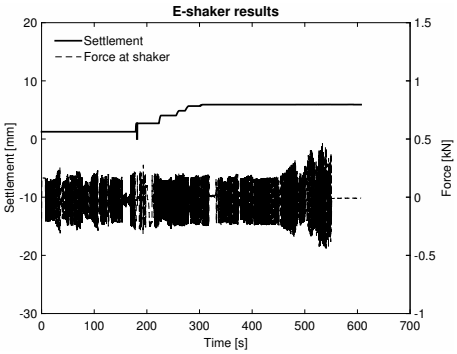

(f) Force at shaker Test 63

Figure B.18: The measured settlement of the upper cone and the amplitude of the applied vibration in the installation tests with slip-joint set 1 of the seventh batch of experiments.

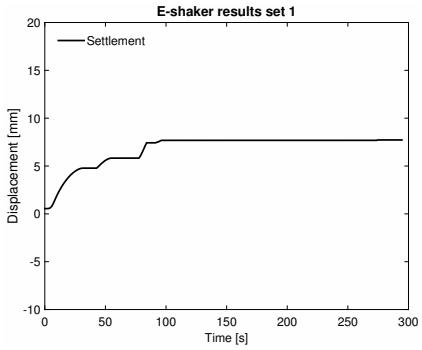

(a) Test 65 - 120 Hz

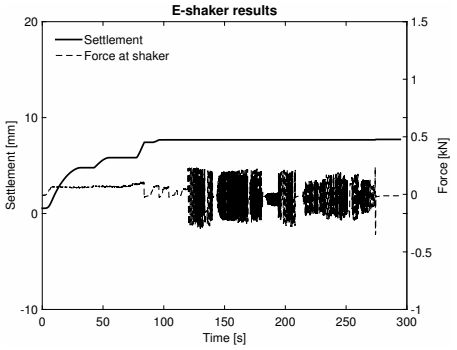

(b) Force at shaker Test 65

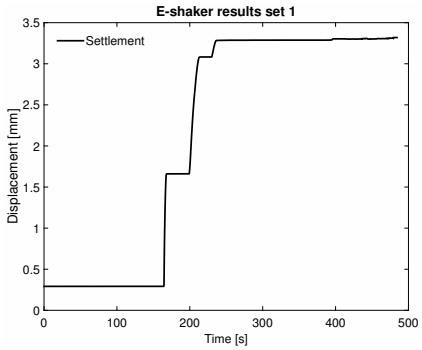

(c) Test 68

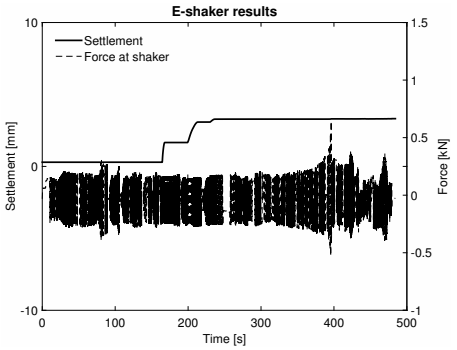

(d) Force at shaker Test 68

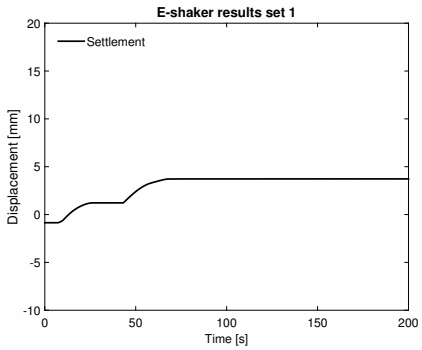

(e) Test 70

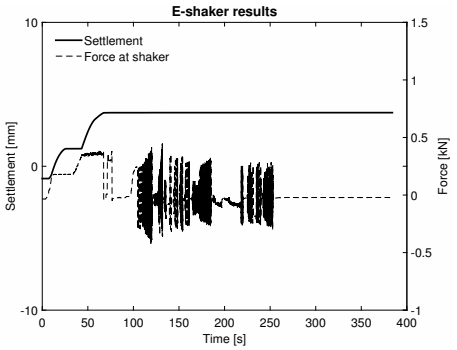

(f) Force at shaker Test 70

Figure B.19: The measured settlement of the upper cone and the amplitude of the applied vibration in the installation tests with slip-joint set 1 of the seventh batch of experiments.

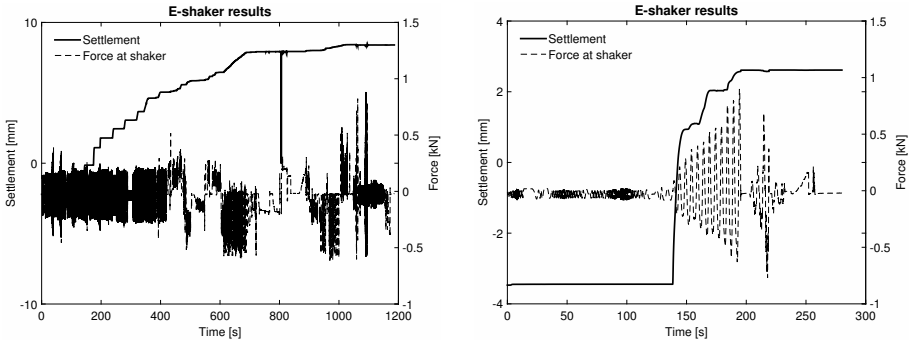

(a) Force at shaker Test 73

(b) Force at shaker Test 75

Figure B.20: The measured settlement of the upper cone and the amplitude of the applied vibration in the installation tests with slip-joint set 1 of the seventh batch of experiments.

fully at a frequency of vibration of 120 Hz. The axial force in test 72 was -30 kN, while, in test 74, the required axial force was -40 kN. This increase in required force shows that, after several tests, the wear increased the friction between the surfaces. The tests that were performed with the shaker demonstrate that the settlement that is induced by vibration can be obtained with relatively small amplitudes, which may make the installation and dismounting of slip-joints by means of vibration possible in full scale.

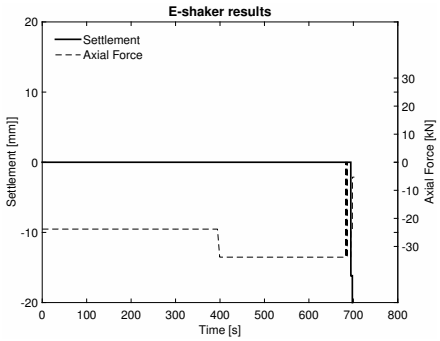

(a) Applied axial force Test 57

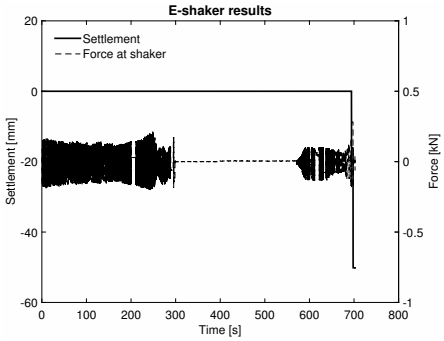

(b) Force at shaker Test 57

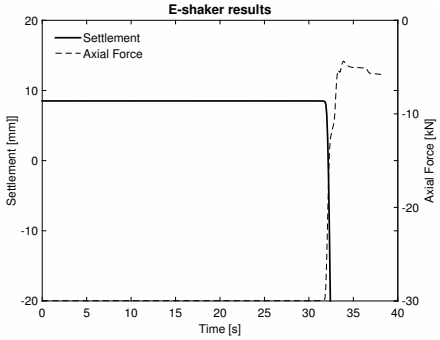

(c) Applied axial force Test 59

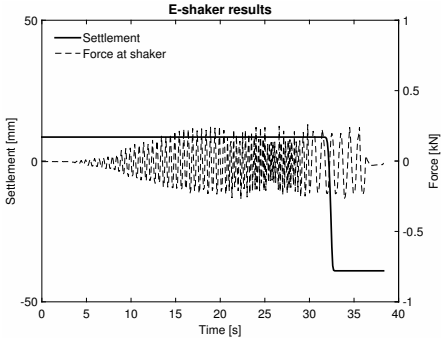

(d) Force at shaker Test 59

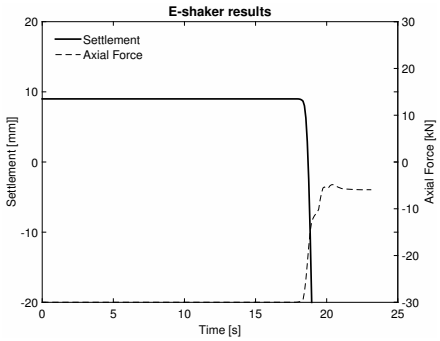

(e) Applied axial force Test 62

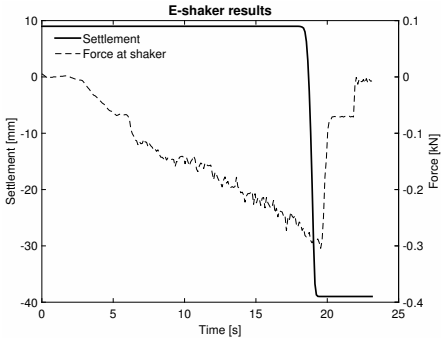

(f) Force at shaker Test 62

Figure B.21: The measured settlement of the upper cone, the applied axial forces and the amplitude of the applied vibration in the dismount tests with slip-joint set 1 of the seventh batch of experiments.

B

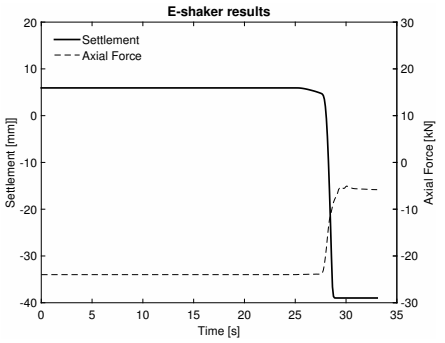

(a) Applied axial force Test 64

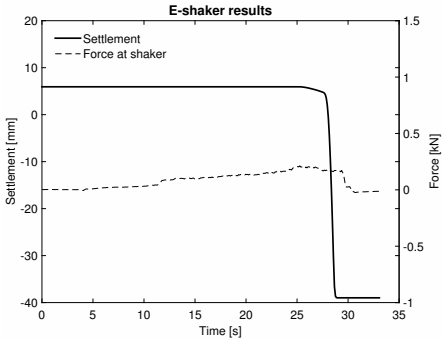

(b) Force at shaker Test 64

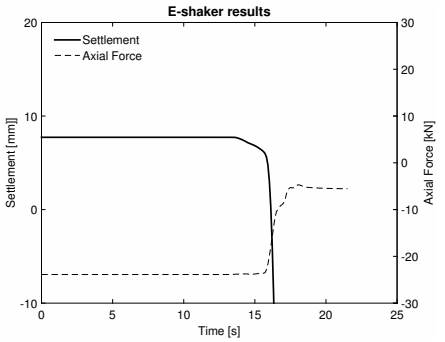

(c) Applied axial force Test 67

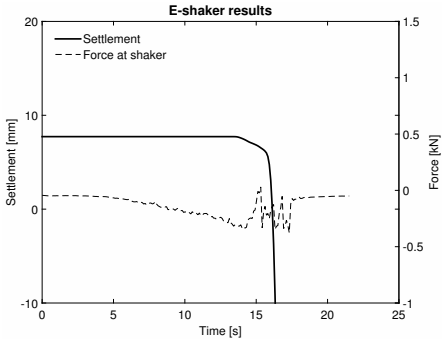

(d) Force at shaker Test 67

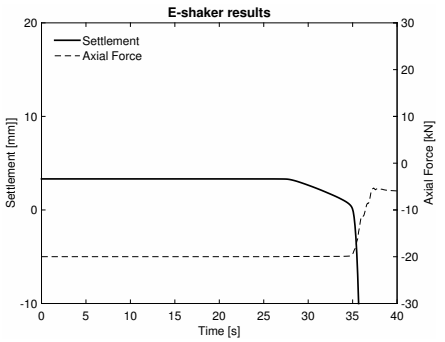

(e) Applied axial force Test 69

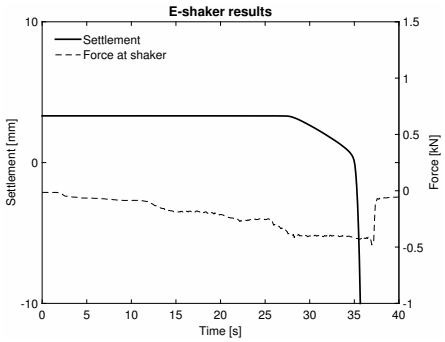

(f) Force at shaker Test 69

Figure B.22: The measured settlement of the upper cone, the applied axial forces and the amplitude of the applied vibration in the dismount tests with slip-joint set 1 of the seventh batch of experiments.

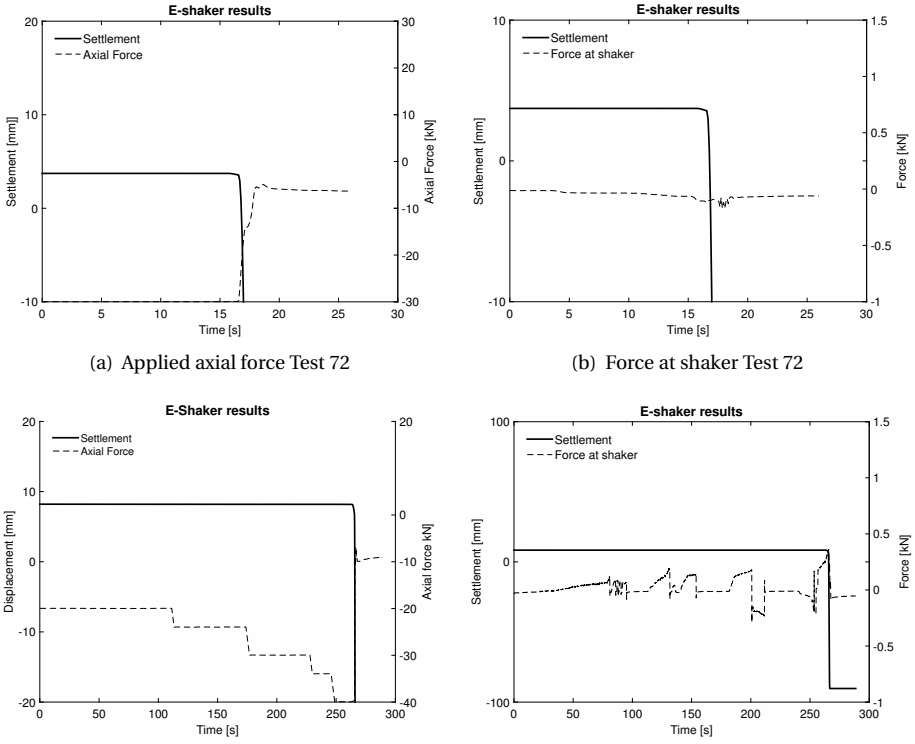

(a) Applied axial force Test 72

(b) Force at shaker Test 72

(c) Applied axial force Test 74

(d) Force at shaker Test 74

Figure B.23: The measured settlement of the upper cone, the applied axial forces and the amplitude of the applied vibration in the dismount tests with slip-joint set 1 of the seventh batch of experiments.

B.9. RESULTS OF BATCH 8: TESTS 76-84 WITH SLIP-JOINT SET 1

In batch 8 another comparison of the effects of the eccentric motors and electric shaker was conducted by replacing the electric shaker with the eccentric motors on cone set 1. The results allow the results obtained previously using the electric shaker and the two cone sets to be compared.

B.9.1. RESULTS OF THE INSTALLATION EXPERIMENTS

In Figure B.24(a), the measured settlement and the applied axial load over time observed in test 77 are given. In this test the settlement under the simulated weight was investigated. The results demonstrate a stick-slip behaviour caused by the increase of the axial force.

In Figure B.24(b), the settlement over time observed in test 78 is depicted. In this test, settlement under vibrations with frequencies from 0 to 200 Hz and an axial load of 10 kN was investigated. The figure shows settlement events at 27, 78, 110, 115, and 120 Hz with a total settlement of 10 mm. These results indicate that both vibration actuators are able to induce settlements of similar levels. Furthermore, for both cone sets, the final settlement event was obtained with vibrations at a frequency of approximately 120 Hz.

In Figures B.24(c) and B.24(d), one can see the settlement levels achieved after the first and the last settlement events with the step-wise increase of frequency of vibrations featured in test 80. A total of 10 mm of settlement is obtained and settlement events were found to occur at the same frequency as in test 78 (120 Hz).

Figure B.24(e) depicts the result of test 82. In this test, the frequency of vibration was slowly increased from 0 to 120 Hz over 60 seconds. The figure indicates that several settlement events occurred and that the largest settlement was obtained at approximately 120 Hz. The settlement stabilized to an equilibrium depth, and a total settlement of 7.9 mm was obtained. Increasing and decreasing the frequency after the equilibrium was reached led to no additional settlement. This demonstrates that the increment of the frequency was small enough to allow the resonance to develop into the maximum possible settlement events.

Figure B.24(f) presents the result of test 84. In this test, the frequency of vibration was slowly increased from 0 to 120 Hz over 180 seconds. Settlement events were observed at 25, 33, 65, 78, 89, and from 107 to 120 Hz, resulting in a total settlement of 8.5 mm.

Comparing the results of the two actuators, one can conclude that no settlements were obtained for frequencies below the 75 Hz with the electric shake; in contrast, the eccentric motors could induce settlements at 30 Hz with both sets. This means that the settlement events that occurred below 70 Hz were amplitude-driven and were a result of the increase of the applied axial load delivered by the eccentric motors.

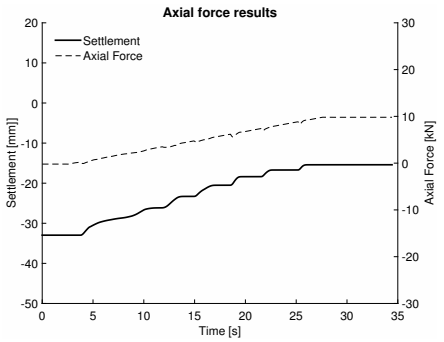

(a) Applied axial force Test 77

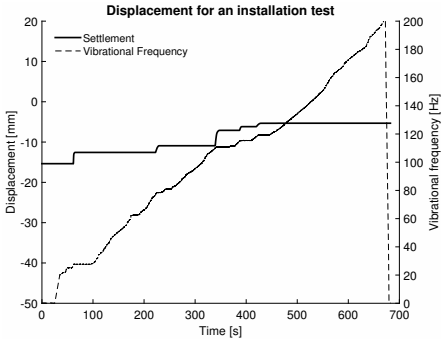

(b) Test 78; F_{ax}=10 kN

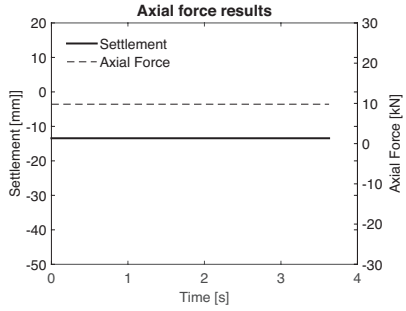

(c) Test 80-1

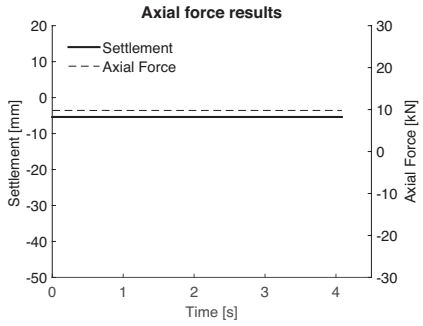

(d) Test 80-5

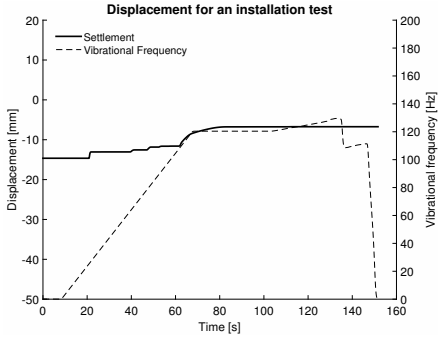

(e) Test 82

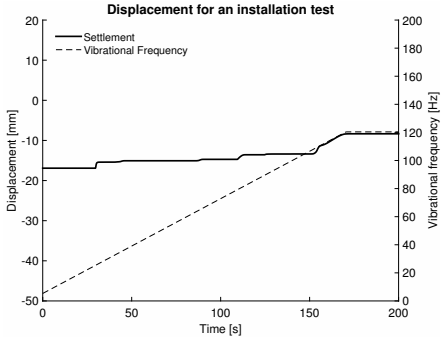

(f) Test 84

Figure B.24: The measured settlement of the upper cone, the applied axial load and the frequency of the applied vibration in the installation tests with slip-joint set 1 of the eight batch of experiments

B.9.2. RESULTS OF THE DISMOUNTING EXPERIMENTS

Figure B.25(a) and B.25(b) provide the results of dismounting test 76. The figures indicate that vibration at 120 Hz is effective in terms of achieving a dismounting of the cones and that the axial force needs to be increased to -30 kN in order to achieve a successful dismount. Note that, prior to this test, the cones were installed with the electric shaker and that, using the eccentric motors with much greater power, a successful dismounting was not achieved until the axial force was increased. This demonstrates two things: The first is that both actuators are equally effective in producing settlement events for the slip-joint, and the second is that there is a limit to what vibrations can realize without axial forces when wear of the contact areas begins to occur.

Figures B.25(c) to Figure B.25(e) depicts three successful dismounts achieved using a slow increase of frequency from 0 to 118 Hz over 60 seconds. The figures illustrate the influence of wear on the settlement levels achieved during the installation tests.

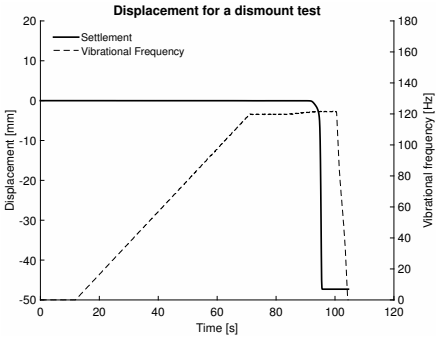

(a) Test 76

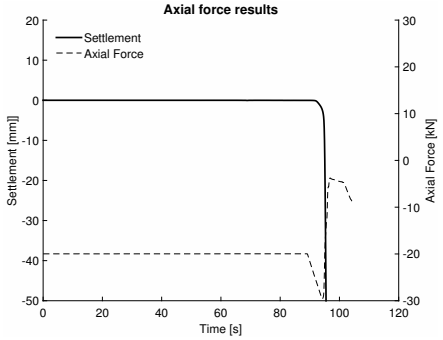

(b) Applied axial force Test 76

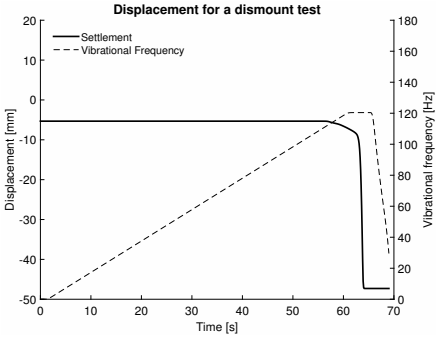

(c) Test 79; F_{ax}= -24 kN

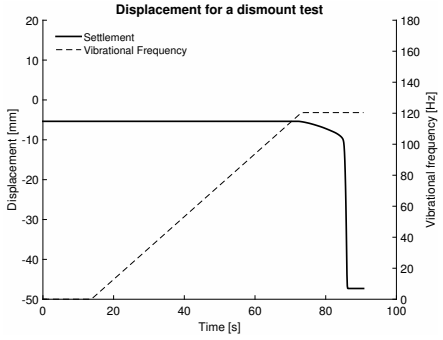

(d) Test 81; F_{ax}= -22 kN

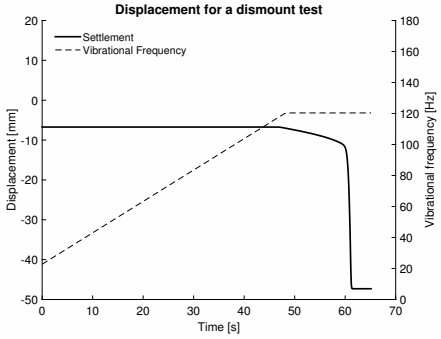

(e) Test 83; F_{ax}= -22 kN

Figure B.25: The measured settlement of the upper cone, the applied axial load and the frequency of the applied vibration in the dismount tests with slip-joint set 1 of the eight batch of experiments.

B

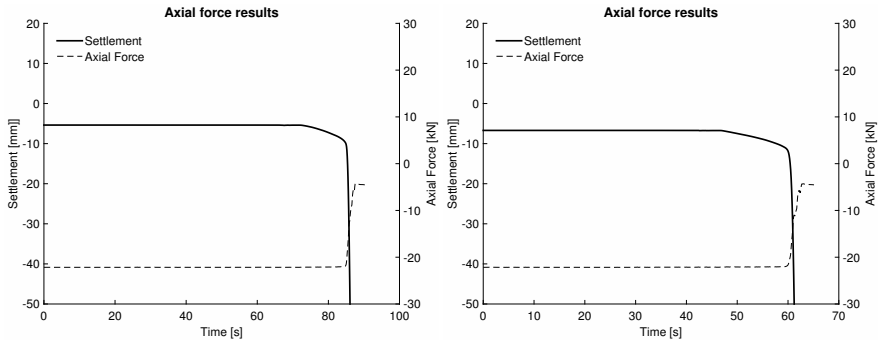

(a) Applied axial force Test 81

(b) Applied axial force Test 83

Figure B.26: The applied axial loads during the dismounting tests with slip-joint set 1 of the eight batch of the experiments.

ACKNOWLEDGEMENTS

Finally, this amazing and challenging journey of my PhD research has come to an end. This PhD thesis has been finalized with the assistance and support of many people and I would like to thank you all sincerely.

First of all, I want to thank my promotor Andrei for taking me under your wing since the day we started the discussions on this PhD work. Thank you for the support and guidance in completion of this work. Working with you has been inspiring and I have great respect for your commitment to your so-called crazy group of friends. Hayo, I want to thank you for your support and guidance over the last years. I enjoyed the many discussions and laughs we had during our carpooling and I look back with a smile on our shared experiences during our PhD's.

I would like to thank Gijs van Kuijk and Jan van der Tempel for creating the PhD position at the TU Delft within the research programme FLOW. Without the both of you, I would not have had the opportunity to start my PhD. My (former) colleagues Antonio, Niels, David and Wybren, that were there at the start of this journey, thank you for your support.

John and Kees of the Stevinlab, thank you for your assistance, dedication during the built and execution of the experiments, and the sacrificed evenings in which some of the (loud) experiments had to be conducted. Siamand, thank you for your support and allowing me to use your equipment. I would like to thank my former BSc and MSc students and in special Koen for the fruitful collaborating during the experiments. I am also grateful to my colleagues of the research groups of Offshore Engineering and Dynamics of Solids and Structures for their support and making the past years enjoyable.

Niels and Thomas, my old room mates, thank you for standing beside me as my paranymphs, for your friendship, and your support ever since the WMZ. It feels special to share this moment with you. My parents, for believing in me and allowing me to find my way in life. Your endless love and support, regardless of my choices, have allowed me to become who I am today. My brother, thank you for your help in the design of the cover and your support in the last weeks.

Finally, I cannot thank my wife Mirjam enough. You have been always there for me during the past years and always reminded me that I can do this. Thank you for your support and encouragement to work day and night to finish this thesis.

SAMENVATTING

Het merendeel van de bestaande offshore windturbines bestaat typisch uit een monopile fundering, een overgangsstuk met een verticaal gepositioneerde gevoegde verbinding, een turbinetoren en een turbine. Van de 2.653 offshore-turbines die eind 2015 zijn geïnstalleerd, wordt 80 procent ondersteund door een monopile.

Ondanks de huidige overweldigende dominantie van de monopile is de toekomstige toepassing ervan nogal onzeker. Offshore windturbines zijn voortdurend in capaciteit en omvang toegenomen, en zijn naar diepere wateren verhuisd; deze ontwikkelingen vereisen grotere en zwaardere ondersteuningsconstructies. Het is onwaarschijnlijk dat drijvende structuren de voorkeur gaan krijgen boven bodemstructuren, tot een waterdiepte van 80 m. De vraag is dus of jacket-constructies of monopiles onder dergelijke omstandigheden zullen worden gebruikt? De monopile lijkt te verliezen in deze wedstrijd, omdat, om aan de vereisten te voldoen, een monopaal extreem groot zou moeten zijn; het kan dus niet langer binnen de grenzen van de industrie vallen, zowel in termen van productie-eisen als de hefcapaciteit van speciale wind-installatieschepen. Men kan zich afvragen of een enkele monopile noodzakelijk zou zijn, of dat een reeks van intelligent verbonden kleinere monopiles zou kunnen volstaan. De sleutel tot het succes van een dergelijk concept zou de zogenaamde slip-joint verbinding kunnen zijn.

Een slip-joint bestaat uit twee conische stukken staal, waarvan een de conische bodem van het overgangsstuk is en de andere de conische top van de funderingspaal vormt. Voor deze verbinding is geen 'grout' nodig en, naast een verbindingsoptie voor het overgangsstuk en monopile, kunnen deze monopiles dan bestaan uit een aantal lichtere gedeelten met zeer grote diameters. Door gebruik te maken van een slip-joint kan de toepasbaarheid van de monopile worden uitgebreid tot diepere wateren en voor turbines met zeer grote rotors en vermogenscapaciteiten.

Hoewel de slip-joint in het verleden met succes werd gebruikt voor onshore windturbines, is deze nog niet offshore gebruikt. Een van de uitdagingen bij het gebruik van de verbinding is het zorgen voor een juiste passing van de conussen ondanks de imperfecties die het gevolg zijn van fabricagetoleranties, vervormingen door heien en de potentiële schade die kan optreden tijdens het hanteren van de conussen.

In dit proefschrift wordt voorgesteld om een klein verschil in de hoeken van de conussen te gebruiken om de bovengenoemde onvolkomenheden aan te pakken. Een steilere hoek van de conus voor het overgangsstuk in vergelijking met die van de monopile wordt voorgesteld. Deze enigszins verschillende hoeken vereisen dat de bovenste conus elastisch vervormt om omlaag te schuiven langs de onderste conus tijdens de installatie. Om het installatieproces te vergemakkelijken, wordt voorgesteld dat trillingen worden

toegepast om de bovenste conus naar beneden te laten glijden met behulp van zijn eigen gewicht. Om deze nieuwe methode van verbinden te gebruiken, zal het nodig zijn om te onderzoeken op welke manier trillingen invloed hebben op de relatieve bewegingen tussen de twee conussen die een stabiel contact moeten bereiken.

Het doel van dit proefschrift is om het potentieel van het gebruik van trillingen in de installatie en demontage van een slip-joint met licht verschillende conushoeken te onderzoeken. Het onderzoek wordt uitgevoerd door middel van numerieke modellering en experimenten.

Om een voorlopig onderzoek naar de dynamica van de slip-joint uit te voeren, wordt een lumped-massa model van de door trillingen geïnduceerde zakking van een slipverbinding ontwikkeld en geanalyseerd. De voorspellingen van het model geven aan dat de slipafstand, veroorzaakt door het gewicht van de bovenste conus van een slipverbinding alleen, onvoldoende is om het gewenste contact tussen de conussen te verkrijgen, zelfs voor kleine conushoeken. Er wordt aangetoond dat de gewenste slipafstand kan worden bereikt door middel van het toepassen van een trilling. Verder geeft het model aan dat specifieke combinaties van de amplitude en frequentie van de belasting effectief zijn in het bereiken van de gewenste overlap tussen de conussen. Deze resultaten ondersteunen het idee dat een gecontroleerde installatie van een slipverbinding mogelijk is met behulp van trillingen.

Om de effectiviteit van trillings-geïnduceerde zakking in de installatie en demontage van een slipverbinding voor offshore windturbines aan te tonen met experimenten, is een opstelling ontworpen en gebouwd. De opstelling is zodanig ontworpen dat de beoogde volledige installatievolgorde kan worden nagebootst met geschaalde exemplaren van de slip-joint. Trillingen worden tijdens de experimenten geïntroduceerd met behulp van een set excentrische motoren of een elektrische shaker. Met behulp van deze opstelling worden de volgende onderwerpen onderzocht:

1. Het effect van trillings-geïnduceerde beweging van geschaalde slip-joints wordt onderzocht met behulp van twee soorten trillingsactuatoren.

2. Een experimentele modale analyse wordt uitgevoerd om te identificeren welke frequenties effectief zijn bij het induceren van zakkingen en om de corresponderende effectieve operationele trilvormen van de geschaalde slip-joint te identificeren.

3. De afmetingen en geometrie van een set conussen worden gemeten om de status van de conussen die in de experimenten worden gebruikt te bepalen.

De experimenten tonen aan dat de frequentie van de toegepaste trillingen bepalend is voor de succesvolle installatie of demontage van een slipverbinding. Alleen toegepaste trillingen van specifieke resonantiefrequenties blijken effectief te zijn en laten relatieve beweging toe. Opgemerkt wordt dat een toepassing van een grotere krachtamplitude in combinatie met een frequentie die verschilt van die specifieke resonantiefrequenties die effectief bleken te zijn, niet automatisch resulteert in extra zakking. De waargenomen

zakking tijdens het aanbrengen van trillingen stabiliseert zich tot bepaalde evenwichtsniveaus. Dit waargenomen gedrag maakt deze procedure waarschijnlijk aantrekkelijk voor toekomstige implementatie in offshore condities, wanneer beheersing van het zakkingsniveau gewenst is. Met behulp van een elektrische shaker worden zakkingen verkregen die vergelijkbaar zijn met die welke worden bereikt door het gebruik van een excentrische motor, terwijl de geleverde amplitude van de elektrische shaker 250 keer kleiner is dan die door de excentrische motor wordt geleverd. Dit toont de dominantie van frequentie op het gedrag van de zakking van de slip-joint aan.

Om het gedrag van de conussen te onderzoeken bij de frequenties die effectief bleken te zijn wat betreft de zakking, wordt een experimentele modale analyse uitgevoerd op de geïnstalleerde geschaalde slip-joint. De resultaten van dit experiment bevestigen dat overwegend die trillingen die effectief zijn bij het induceren van zakking, zich bij de eigenfrequenties van het gecombineerde systeem bevinden. De trillingsvorm rond 120 Hz, die het meest effectief is voor installatie- en demontage doeleinden, wordt gekenmerkt door de omtrek modus m = 2 en longitudinale modus n = 1 van een conische cilinder. Op basis van de gemeten afmetingen van de conussen, wordt een indruk van de fabricagetoleranties, het eerste contact en de ontwikkeling van het contact verkregen. De resultaten geven aan dat de conussen grotere lokale vervormingen en ovaliteit hebben dan bedoeld. Analyse van het contact geeft aan dat het zich op twee verschillende gebieden ontwikkelt en vervolgens in omtrek richting expandeert met toenemende zakkingsniveaus.

Een eindig elementenmodel is opgezet, met als doel de experimenten kwalitatief te reproduceren. Het model reproduceert het zakkingsgedrag dat kan worden geïdentificeerd als stick-slip. Bovendien is het model in staat om het belangrijkste aspect van het gedrag van de slip-joint onder invloed van trillingen te reproduceren. Alleen bepaalde natuurlijke frequenties induceren relatieve bewegingen tussen de conussen voor kleine amplituden van de dynamische kracht. Het eindige-elementenmodel is in staat om de frequentieafhankelijkheid van de trillings-geïnduceerde zakking te reproduceren in zowel installatie als demontage simulaties. De specifieke modus die overeenkomt met de omtrekmodus m = 2 en de longitudinale modus n = 1, geïdentificeerd als meest effectief in de experimenten, bleek ook het meest effectief te zijn in het model. Een gedetailleerde analyse van het zakkingsproces en de afhankelijkheid van het tijdssignaal en symmetrie van de belasting bevestigden opnieuw dat de waargenomen en voorspelde zakking een stick-slip-proces is dat optreedt bij de resonantiefrequenties van het gecombineerde systeem.

Een parametrische studie wordt uitgevoerd om de onzekerheden te onderzoeken die aan het eindige-elementenmodel zijn verbonden. Deze studie geeft aan dat het bereikte zakkingsniveau dat is waargenomen in de experimenten, als gevolg van het gesimuleerde eigengewicht, kan worden benaderd door gebruik te maken van een lage wrijvingscoëfficiënt in de simulaties. Het zakkingsniveau dat plaatsvond als gevolg van de toepassing van de trillingen waarvan werd vastgesteld dat ze effectief waren tijdens de experimenten, werd niet geëvenaard met de voorspellingen van het eindige elemen-

tenmodel. Dit verschil kan worden gerelateerd aan de discrepantie tussen het perfecte contact langs de omtrek van het model en het onvolmaakte contact van de geschaalde exemplaren. Door nog lagere wrijvingscoëfficiënten te kiezen, zal de reproductie van de uitkomsten van de experimenten meer accuraat zijn.

Geconcludeerd wordt dat, onder invloed van een trillingsbron, zakkingen tussen de kegels van de slip-joint kunnen worden bereikt. Met behulp van experimenten en numerieke modellering wordt aangetoond dat excitatie op frequenties gelijk aan of dicht bij de natuurlijke frequenties van de slipverbinding cruciaal is voor de succesvolle installatie of demontage van een slip-joint. Het gedrag van de zakking dat wordt geïnduceerd door trillingen, wordt waargenomen als een stick-slip-proces dat uiteindelijk stabiliseert op een niveau van evenwicht; deze stabilisatie wordt waargenomen in de voorspellingen van de numerieke modellen en in de experimenten. Over het algemeen hoopt de auteur dat dit proefschrift de weg zal banen naar de succesvolle toepassing van de innovatieve slip-joint in de volgende generatie offshore windturbines.

LIST OF PUBLICATIONS

JOURNAL PAPERS

1. **M.L.A. Segeren , N.F.B. Diepeveen**, *Influence of the Rotor Nacelle Assembly Mass on the Design of Monopile Foundations*, Heron, Vol. 59 (2014) No. 1, pp. 17-36.

2. **M.L.A. Segeren,E. Lourens, A. Tsouvalas, T.J.J. van der Zee**, *Investigation of a slip joint connection between the monopile and tower of an offshore wind turbine* EIET Renewable Power Generation, Vol.8 (2014) No.4, pp 422-432.

CONFERENCE PAPERS

1. **M.L.A. Segeren**, *Influence of a boatlanding and j-tubes on wave loads and wall thickness of the monopile support structure design*, Proceedings of the EWEA Offshore 2011 Conference, Amsterdam, The Netherlands, 29 November-1 December 2011.

2. **M.L.A. Segeren , E. Lourens**, *Investigation of a slip joint connection between the monopile and tower of an offshore wind turbine* EWEA 2013: Europe's Premier Wind Energy Event, Vienna, Austria, 4-7 Febraury 2013.

3. **M.L.A. Segeren, K.W. Hermans**, *Experimental investigation of the dynamic installation of a slip joint connection between the monopile and tower of an offshore wind turbine*, Journal of Physics: Conference Series, 524 (1), 2014; TORQUE 2014: The Science of Making Torque from Wind 2014, Copenhagen, Denmark, 18-20 June 2014).

CURRICULUM VITÆ

Maxim Luka Adriaan Segeren was born in Dordrecht, the Netherlands, on May 25th, 1983. After finishing his secondary education at the Walburg College in Zwijndrecht in 2001, he started his studies at the faculty of Mechanical Engineering at Delft University of Technology. He graduated in 2009 as an offshore engineer with an M.Sc. thesis titled 'Torsion in offshore wind turbines and the effect of torsion on a jacket support structure'. After working as an independent researcher on a feasibility study for the creation of a renewable Markermeer with wind power production and storage, he started his PhD project in 2010 at the Offshore Engineering Section of Delft University of Technology. During his time as a PhD candidate, he led several consultancy projects on monopile designs for offshore wind projects, and he was the instructor responsible for the master course 'Offshore Wind Support Structure Design'.
Maxim is currently working as a project manager at Delft University of Technology and is involved in the organization of new research projects, setting up a national PhD program, and the valorisation of research output.